Optical monitoring in fabrication of optical coatings

Master's Thesis, 10.6.2019

Author:

Kasper Honkanen

Supervisors:

Olli Herranen, Ph.D.
Jussi Toppari, Professor

UNIVERSITY OF JYVÄSKYLÄ
DEPARTMENT OF PHYSICS

Abstract

Honkanen, Kasper
Optical monitoring in fabrication of optical coatings
Master's thesis
Nanoscience Center, Department of Physics, University of Jyväskylä, 2019, 84 pages.

Optical coatings are employed in various academic and industrial applications to modify or enhance optical properties of materials and components. Therefore optical coatings have a long history of research and development, which is still advancing. For this thesis optical filter design and fabrication methods utilizing vacuum evaporation and optical monitoring were studied. The objective was to test and improve production capabilities of an industrial electron beam evaporation system using direct transmittance measurement for layer thickness monitoring. Four distinct optical coatings of differing complexity were designed and fabricated. The coating types were a Bragg mirror, a short wavelength pass edge filter, a long wavelength pass edge filter and a narrow bandpass absorption filter. Design processes for the filters are shown including their structure and the development of the monitoring strategy. The results are analysed and possible optimization solutions are shortly discussed.

Keywords: thesis, optics, optical monitoring, optical coating, optical filter

Tiivistelmä

Honkanen, Kasper
Optisten pinnoitteiden valmistaminen optisella monitoroinnilla
Pro gradu -tutkielma
Nanoscience Center, Fysiikan laitos, Jyväskylän yliopisto, 2019, 84 sivua

Optinen kerrosmonitorointi optisten pinnoitteiden valmistuksessa

Optinen pinnoite on kappaleelle valmistettu pinnoitus, jonka tarkoituksena on vaikuttaa kappaleen pinnan optisiin ominaisuuksiin. Näitä ominaisuuksia ovat muunmuassa pinnan heijastavuus, transmissio sekä absorptio. Tavallisesti optinen pinnoite laaditaan optiikassa käytettävälle lasikomponentille, kuten linssille tai prismalle. Muitakin materiaaleja voidaan pinnoittaa, kuten muovia.

Optiset pinnoitteet voidaan jaotella erilaisiin alatyyppeihin. Esimerkiksi heijastusta poistava pinnoitus on suunniteltu nimensä mukaisesti minimoimaan pinnasta heijastuvan valon määrää, samalla parantaen transmissiota eli pinnan läpäisevän valon määrää. Pinnoittamattoman lasin ja ilman rajapinnassa heijastuu karkeasti 4 % valosta. Usean läpäisevän komponentin muodostamassa systeemissä on täten välttämätöntä minimoida heijastuksen aiheuttama valotehon menetys. Heijastusta poistava pinnoite on erittäin yleinen optiikkaa sisältävissä laitteissa, kuten kameroissa, aurinkokennoissa, sekä silmälaseissa. Muita optisia pinnoitustyyppejä ovat muunmuassa peilit, optiset suotimet, sekä sädejakajat.

Optinen pinnoitus koostuu toistensa päälle kasatuista ohutkalvoista, joiden paksuus voi vaihdella muutamasta nanometristä mikrometreihin. Toisistaan poikkeavan taitekertoimen omaavien kalvojen rajapinnassa valo osittain sekä heijastuu että transmittoituu. Täten kalvosysteemin sisällä on sekä eteneviä että takaisin heijastuneita valonsäteitä, jotka pystyvät interferoimaan toistensa kanssa. Interferensssin voimakkuus riippuu kohtaavien aaltojen vaihe- sekä amplitudierosta. Vaihe-eroihin voidaan vaikuttaa säätämällä kalvojen kerrospaksuutta. Pinnoitteelle toivotunlaisten optisten ominaisuuksien saavuttamiseksi pinnoitteen suunnittelussa täytyy valita

sopivat kalvomateriaalit ja kalvojen lukumäärä, sekä määrittää toimivat kerrospaksuudet. Yksinkertaiset pinnoitteet voivat sisältää vain muutaman ohutkalvon, mutta vaativammat optiset pinnoitteet ovat erittäin monimutkaisia sisältäen kymmeniä tai jopa satoja ohutkalvoja. Pinnoitteiden suunnittelussa on tänä päivänä mahdollista käyttää apuna kaupallisia tietokoneohjelmia.

Pinnoitteiden valmistamiselle on teollisuudessa käytettävissä useita erilaisia pinnoitusmenetelmiä, kuten terminen höyrystys, kemiallinen höyrystys sekä sputterointi. Näille menetelmille puolestaan löytyy useita erilaisia variaatioita. Menetelmille yhteistä on pinnoitemateriaalin siirtäminen ulkoisesta lähteestä pinnoitettavalla kappaleelle hiukkasina. Kalvopakan kerrosten paksuus on tärkeää saada pinnoituksessa oikein, sillä muuten lopullisen pinnoitteen ominaisuudet voivat kärsiä. Pinnoitettavan kerroksen paksuutta voidaan monitoroida reaaliajassa, ja pinnoitus lopetetaan siinä vaiheessa, kun sopiva kerrospaksuus on saavutettu. Yleinen menetelmä fyysisen kerrospaksuuden monitorimiseksi on kvartsikidemonitorointi, jonka toiminta perustuu kvartsikiteen mitattavan värähtelytaajuudeen riippuvuuteen kiteelle päätyneen pinnoitteen paksuudesta. Toinen vaihtoehto on monitoroida pinnoitteen optisien ominaisuuksien muuttumista transmittanssi- tai heijastusmittauksella, jonka avulla voidaan määrittää pinnoitteen paksuus. Tätä kutsutaan optiseksi monitoroinniksi.

Tässä tutkielmassa esitellään optisten pinnoitteiden ominaisuuksia sekä valmistusmenetelmiä, joihin lukeutuvat yleiset optiikan valmistukseen käytetyt pinnoitusteknologiat sekä optisen monitoroinnin periaatteet. Kokeellisessa osassa suunniteltiin neljä erilaista optista suodinpinnoitetta. Suunnitellut pinnoitteet valmistettiin käyttäen tyhjiöhöyrystystekniikkaa ja optista kerrospaksuusmonitorointia. Tutkielman tavoitteena oli tutustua optiseen monitorointiin ja testata teollisen tyhjiöhöyrystyslaitteiston sekä suoran transmittanssimonitoroinnin tuotantokykyä. Suodintyypit olivat Braggin peili, lyhytpäästö- ja pitkäpäästösuotimet, sekä absorptiotyypin kapeakaistapäästösuodin. Pinnoitteiden suunnitteluprosessit esitellään kokonaisuudessaan rakenteen muodostamisesta monitorointistrategian laatimiseen. Tuloksia analysoidaan ja mahdollisia keinoja pinnoitteiden parantamiseksi käsitellään lyhyesti.

Avainsanat: opinnäyte, optiikka, optinen monitorointi, optinen pinnoitus, optinen suodin

Acknowledgements

I want to express my gratitude to Millog for the opportunity to work with an interesting topic, as well as for the extraordinarily welcoming working environment. I think the experience has been both pleasant and highly valuable.

I would like to thank my supervisors for their advice and constructive feedback on the thesis. Doctor Olli Herranen guided the experimental part of the thesis, offered advice when needed, and has been a pleasure to work with. Professor Jussi Toppari has offered useful comments especially on the theoretical part of the thesis and kindly supported the project. Thank you!

I would also like to thank Millog's evaporation machine operators Katri Alli and Vesa Hautala for assisting with the use of the evaporation machine and for providing technical support.

Finally, I want to offer my sincerest gratitude to my family and friends for their continuous love, support and encouragement. Thank you for being a part of this journey. You made it all worthwhile.

Jyväskylä, June 2019

Kasper Honkanen

Contents

Abstract **iii**

Tiivistelmä **v**

Acknowledgements **vii**

1 Introduction **3**

2 Theoretical background **5**

2.1 Physics of optical thin-films 5

2.1.1 Fresnel equations 5

2.1.2 A thin film stack 9

2.1.3 Quarter-wave stack 10

2.1.4 Absorption bandpass filter 13

2.2 Fabrication methods 14

2.2.1 Thermal evaporation 15

2.2.2 Sputtering 17

2.2.3 Chemical vapour deposition 19

2.2.4 Atomic layer deposition 20

3 Optical monitoring **23**

3.1 Overview of optical monitoring 23

3.2 Different optical monitoring systems 25

3.2.1 Direct and indirect monitoring techniques 25

3.2.2 Broadband monitoring 26

3.2.3 Monochromatic monitoring 27

4 Experimental methods **29**

4.1 Computational methods 29

4.1.1 Used software 29

4.1.2 Forming a monitoring strategy 32
4.1.3 Refractive index characterization 33
4.2 Equipment and experimental methods 37
4.2.1 Coating machine 37
4.2.2 Optical monitoring system 40
4.2.3 Sample analysis 42

5 Design process and results 43
5.1 Bragg mirror 43
5.1.1 The first design 43
5.1.2 The second design 47
5.2 Short pass edge filter 51
5.2.1 The first design 52
5.2.2 The second design 59
5.3 Long pass edge filter 63
5.4 Narrow bandpass filter 70

6 Conclusion 79

Appendix I

1 Introduction

Optical coatings have a wide variety of applications and are utilized in most optical devices, like lenses and prisms. Optical coatings modify optical properties of the coated surface. Antireflection (AR) coatings [1] are one of the most prevalent optical coatings in the industry. AR coatings eliminate most of the reflection at the surface of an optical component, thus enhancing its transmissivity. This can be vital for minimizing transmission losses through multiple transmissive elements. AR coatings can be found for example in glasses, cameras and solar cells. On the other hand a coating may exhibit high reflectivity and be used as a mirror. Beam splitters [2] split an incident light beam into two beams, and the ratio of transmittance to reflectance can be chosen to be wavelength-dependent. Beam splitters have applications in interferometry, laser systems and cameras [3]. As optical coatings grow in complexity they can even be used as optical filters. A single coating may contain both highly transmissive and highly reflective regions effectively filtering out certain wavelengths. For example a short wavelength pass edge filter will transmit a wavelength band shorter than its cut-off wavelength and block longer wavelengths.

Optical coatings are multilayered thin film assemblies, where a single film may have a thickness from a couple nanometers to few micrometers. The films are deposited in a stack with precisely chosen layer thicknesses and alternating layer materials. At each layer boundary the change in refractive index of the medium causes the light to partly reflect and to partly transmit. Therefore inside the assembly there are numerous light beams advancing in both directions. The light beams can then interfere with each other, affecting the transmissivity and reflectivity of the coating. By carefully controlling the layer materials and the layer thicknesses certain types of self-interference patterns and optical behaviour can be created.

The most simple optical coating may only be a singular thin film on a substrate, but normally it is necessary to employ multiple layers. As the desired performance requirements of the coating increases, so do the required layer count, the overall structural complexity and the error sensitivity of the layers. For example a relatively simple AR-coating could contain less than ten layers, whereas the most complex

coatings may contain hundreds [4] or even thousands [5] of layers. High layer count structures are typically extremely sensitive to manufacturing flaws such as errors in layer thicknesses, refractive indices or layer inhomogeneity [6]. Further issues may arise from presence of very thin layers, which are especially sensitive to errors. It becomes clear that as the coatings become more complicated, the manufacturing techniques have to also be improved.

Optical coatings are manufactured using various types of nanoscale fabrication methods, such as vacuum evaporation, sputtering or chemical vapour deposition. In order to control the layer thicknesses reliably the deposited layer thickness should be monitored in real-time during the deposition process. This allows for accurate layer deposition termination at correct thickness values. One common and well-established monitoring method is to measure the physical layer thickness using quartz crystal monitoring. Another option is to monitor the deposited layer optically. As the layer thickness grows the optical properties of the coating change because of the self-interference of the light. Monitoring the changes in either transmittance or reflectance of the coating allows the optical layer thickness to be determined.

In this thesis I will first present theoretical background to the light self-interference phenomenon inside an optical thin film multilayer system. Then I will briefly introduce some of the most relevant nanofabrication methods used to manufacture optical coatings. In section 3 I will explain the principles of optical monitoring technology and introduce some of its variants.

For the experimental part of the thesis four different optical coatings were designed using computational methods. The coatings were a Bragg mirror, a long wavelength pass edge filter, a short wavelength pass edge filter and a narrow bandpass filter. For each of them an optical monitoring strategy was designed, after which they were fabricated using vacuum evaporation and monitored using direct intermittent monochromatic monitoring. The design processes are focused around forming a robust and repeatable monitoring strategy and will be discussed from that point of view. Lastly the results and how they possibly can be improved will be discussed.

The thesis was written for Millog Oy, who provided the equipment and support for the experimental part, as well as the software required for the computational coating design. Additional support was received from the evaporation machine manufacturer Bühler.

2 Theoretical background

2.1 Physics of optical thin-films

2.1.1 Fresnel equations

Let us consider a situation depicted in figure 1, where there is a surface boundary interface between two non-absorbing dielectric materials with refractive indices n_1 and n_2 so that $n_1 \neq n_2$. An incident light beam i arrives at the interface with angle θ_i from the surface normal. A part of the light becomes reflected (r beam) with an angle $\theta_r = \theta_i$ and another part becomes refracted through the interface (called transmitted t beam). Let us denote $\theta_r = \theta_i = \theta_1$ and $\theta_t = \theta_2$. The transmitted light advances through medium 2 in an angle that obeys Snell's law of refraction:

$$\frac{n_1}{n_2} = \frac{\sin\theta_2}{\sin\theta_1} \tag{1}$$

If the incident light is unpolarized, its electric field E can be broken down into $\vec{E}$-vectors perpendicular (s-polarization) and parallel (p-polarization) to the plane of incidence. The magnetic field $\vec{B}$ will always be perpendicular to the $\vec{E}$-field and its direction of propagation. The $\vec{E}$ and $\vec{B}$ vectors parallel to the plane of incidence can be further broken down into their horizontal (h) and vertical (v) components. Maxwell's equations can be used to derive the boundary conditions for how the light behaves at the dielectric interface. The vector sum of the horizontal components of $\vec{E}$ and $\vec{B}$ have to be equal between the mediums:

$$E_{1,h} = E_{2,h} \tag{2}$$

$$B_{1,h} = B_{2,h} \tag{3}$$

Let us first handle the case of s-polarized light. The horizontal components of $\vec{B}$ in medium 1 have to add up to $\vec{B}_{t,h}$ due to the second boundary condition 3.

$$\begin{aligned} \vec{B}_{i,h} + \vec{B}_{r,h} &= \vec{B}_{t,h} \\ \Leftrightarrow B_i \cos\theta_i - B_r \cos\theta_r &= B_t \cos\theta_t \end{aligned} \tag{4}$$

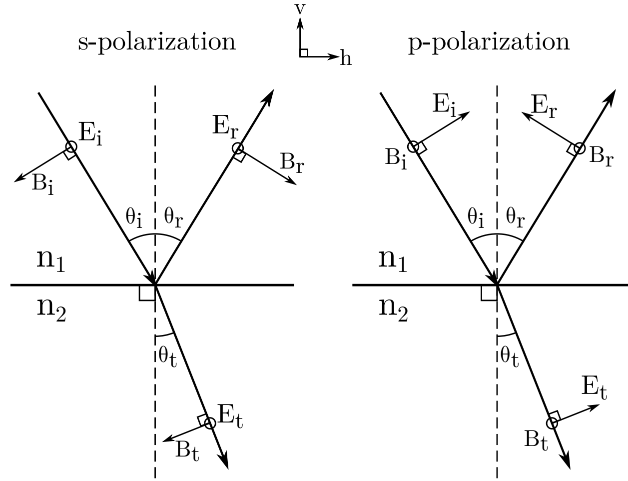

Figure 1. A diagram showing the orientation of electric and magnetic field vectors in s- and p-polarized light at an interface between two optical materials n_1 and n_2. i denotes the incident light, r the reflected light and t the transmitted or refracted light.

There is a relation between B and E:

$$B = \frac{E}{c_{medium}} = \frac{n}{c_0} E \tag{5}$$

This relation is substituted into equation 4. Corresponding indices for n and θ are used.

$$n_1 E_i \cos\theta_1 - n_1 E_r \cos\theta_1 = n_2 E_t \cos\theta_2 \tag{6}$$

Since the electric field is entirely horizontal, it must be equal between mediums. Therefore $E_t = E_i + E_r$. This is substituted into the previous equation, which can then be rearranged to find a ratio E_r/E_i:

$$\begin{aligned} n_1 E_i \cos\theta_1 - n_1 E_r \cos\theta_1 &= n_2 (E_i + E_r) \cos\theta_2 \\ \Leftrightarrow E_i (n_1 \cos\theta_1 - n_2 \cos\theta_2) &= E_r (n_1 \cos\theta_1 + n_2 \cos\theta_2) \\ \Leftrightarrow \boxed{\frac{E_r}{E_i} = \rho_s = \frac{n_1 \cos\theta_1 - n_2 \cos\theta_2}{n_1 \cos\theta_1 + n_2 \cos\theta_2}} \end{aligned} \tag{7}$$

This is the first Fresnel equation, which describes the ratio E_r/E_i for s-polarized light. ρ is called the Fresnel amplitude reflection coefficient.

Now let us substitute $E_r = E_t - E_i$ into the equation 6 and solve ratio E_t/E_i:

$$\begin{aligned} & n_1 E_i \cos\theta_1 - n_1(E_t - E_i)\cos\theta_1 = n_2 E_t \cos\theta_2 \\ \Leftrightarrow\ & E_i(2n_1\cos\theta_1) = E_t(n_1\cos\theta_1 + n_2\cos\theta_2) \\ \Leftrightarrow\ & \boxed{\frac{E_t}{E_i} = \tau_s = \frac{2n_1\cos\theta_1}{n_1\cos\theta_1 + n_2\cos\theta_2}} \end{aligned} \tag{8}$$

This second Fresnel equation describes the ratio E_t/E_i for s-polarized light. τ is called the Fresnel amplitude transmission coefficient.

Next we will consider the p-polarized light. Similarly to the case of s-polarization, the horizontal components of $\vec{E}$ in medium 1 have to be equal to $\vec{E}_{t,h}$ as stated by the boundary condition 2.

$$\begin{aligned} & \vec{E}_{i,h} + \vec{E}_{r,h} = \vec{E}_{t,h} \\ \Leftrightarrow\ & E_i\cos\theta_i - E_r\cos\theta_r = E_t\cos\theta_t \end{aligned} \tag{9}$$

Similarly the magnetic field must be equal between the mediums: $B_i + B_r = B_t$. Using the relation between B and E (equation 5) we get an equation:

$$\frac{n_1}{c_0}E_i + \frac{n_1}{c_0}E_r = \frac{n_2}{c_0}E_t\,.$$

After dividing this equation by c_0 and rearranging for E_t we find:

$$E_t = \frac{n_1}{n_2}(E_i + E_r)\,,$$

which is substituted into equation 9:

$$E_i\cos\theta_i - E_r\cos\theta_r = \frac{n_1}{n_2}(E_i + E_r)\cos\theta_t\,. \tag{10}$$

We can then solve for ratio E_r/E_i. Corresponding indices for θ are used.

$$\begin{aligned} & E_i(n_2\cos\theta_1 - n_1\cos\theta_2) = E_r(n_1\cos\theta_2 + n_2\cos\theta_1) \\ \Leftrightarrow\ & \boxed{\frac{E_r}{E_i} = \rho_p = \frac{n_2\cos\theta_1 - n_1\cos\theta_2}{n_1\cos\theta_2 + n_2\cos\theta_1}} \end{aligned} \tag{11}$$

This is the third Fresnel equation, and it describes the ratio E_r/E_i for p-polarized light.

Now let us substitute $E_r = \frac{n_2}{n_1}E_t - E_i$ into the equation 9 and find out ratio E_t/E_i:

$$\begin{aligned} E_i \cos\theta_1 - (\frac{n_2}{n_1}E_t - E_i)\cos\theta_1 &= E_t \cos\theta_2 \\ \Leftrightarrow E_i(2n_1\cos\theta_1) &= E_t(n_1\cos\theta_2 + n_2\cos\theta_1) \\ \Leftrightarrow \boxed{\frac{E_t}{E_i} = \tau_p = \frac{2n_1\cos\theta_1}{n_1\cos\theta_2 + n_2\cos\theta_1}} \end{aligned} \tag{12}$$

This is the fourth Fresnel equation, which describes the ratio E_t/E_i for p-polarized light.

In the case of incident light arriving to the surface at a normal angle $\theta_1 = 0°$ there is no distinction between s- and p-polarization. The Fresnel equations then take forms

$$\rho = \frac{n_1 - n_2}{n_1 + n_2} \tag{13}$$

$$\tau = \frac{2n_1}{n_1 + n_2} \tag{14}$$

So far we have assumed the dielectric mediums to be non-absorbing. An absorbing medium has a fully complex refractive index $N = n - \mathrm{i}k$ where n is the real refractive index, usually called just the refractive index, and k is the extinction coefficient. For further analysis it is convenient to combine the incidence angle θ with N by introducing an unit called the tilted admittance η, which for any given layer is defined as

$$\begin{cases} \eta_s = N\cos\theta, & \text{for s-polarization} \\ \eta_p = \dfrac{N}{\cos\theta}, & \text{for p-polarization} \end{cases}.$$

Now the boundary reflection and transmittance coefficients can be derived for absorbing medium similarly to the non-absorbing case with oblique incidence. [7, p. 29-32]

$$\rho = \frac{\eta_1 - \eta_2}{\eta_1 + \eta_2} \tag{15}$$

$$\tau = \frac{2\eta_1}{\eta_1 + \eta_2}. \tag{16}$$

2.1.2 A thin film stack

Suppose a stack of optical thin films with the total layer count being j. Let us assume that the thin film layers are homogeneous and their boundaries are parallel. In such an assembly there are multiple medium boundary interfaces, where an incoming light beam is able to reflect and transmit. Each boundary interface has on optical admittance $Y = B/E$, which is analogous to relation 5. In a thin film assembly the reflected light from the farther interfaces is able to interfere with the incoming light. In other words, inside a thin film assembly there are transmitted and reflected light beams that interfere with each other. This is the self-interference phenomenon that grants an optical thin film coating its optical properties. A film with physical thickness t effectively has a phase thickness $\delta = \alpha - \mathrm{i}\beta$ where

$$\alpha = 2\pi nt/\lambda \cos\theta \tag{17}$$

$$\beta = 2\pi kt/\lambda \cos\theta\,. \tag{18}$$

The phase thickness is the total phase change the light experiences as it is travelling through a medium $N = n - \mathrm{i}k$ with incidence angle θ. The imaginary part portrays a reduction in wave amplitude [7, p. 41]. The product Nt is called the optical thickness of the film, denoted d. Because the phase thickness and, subsequently, the interference of the light are dependent on $d = Nt$, the optical thickness is a highly relevant unit in thin film optics. We can further combine d with the incident angle θ to find the optical path length D of the light through a thin film:

$$D = d/\cos\theta = Nt/\cos\theta\,.$$

For interference to occur, the optical path difference between two beams of light must be shorter than the coherence length of the light. Films are considered thin when they are able to introduce this self-interference behaviour in light, although film "thinness" is naturally dependent on the wavelength. [7, p. 32] We can write the complex oblique phase thickness of a single thin film as:

$$\delta = 2\pi D/\lambda = \alpha - \mathrm{i}\beta\,. \tag{19}$$

At the boundary between two media the advancing light wave and its E and B components suffer an amplitude reduction caused by the interference with the light wave advancing in opposite direction, that has experienced a phase shift δ.

This causes a change in the optical admittance Y of the boundary. This holds true for every boundary of two media in the entire assembly. Applying the principle behind the Fresnel coefficients for every boundary interface the reflectance and transmittance for the entire assembly of thin films on a substrate can be found. Assuming the incident and exit media are non-absorbing, the thin film assembly will have total reflectance and transmittance:

$$R = \rho\rho^* = \left(\frac{\eta_0 A - C}{\eta_0 A + C}\right)\left(\frac{\eta_0 A - C}{\eta_0 A + C}\right)^* \tag{20}$$

$$T = \tau\tau^* = \frac{4\eta_0\eta_e}{(\eta_0 A + C)(\eta_0 A + C)^*}, \tag{21}$$

where η_0 and η_e are the tilted admittances of the incident and exit media respectively. A and C are defined by the characteristic matrix of the system:

$$\begin{bmatrix} A \\ C \end{bmatrix} = \left(\prod_{r=1}^{j} \begin{bmatrix} \cos\delta_r & (\mathrm{i}\sin\delta_r)/\eta_r \\ \mathrm{i}\eta_r \sin\delta_r & \cos\delta_r \end{bmatrix}\right) \begin{bmatrix} 1 \\ \eta_e \end{bmatrix}. \tag{22}$$

Detailed derivation of the results can be found in Macleod's book *Thin-film optical filters* chapter 2. [7]

Optical admittance for a thin film system including the substrate can be expressed by $Y = C/B$, which is analogous to relation5. The reflectivity of such a system is:

$$\rho = \frac{\eta_0 - Y}{\eta_0 + Y} \tag{23}$$

$$R = \left(\frac{\eta_0 - Y}{\eta_0 + Y}\right)\left(\frac{\eta_0 - Y}{\eta_0 + Y}\right)^*. \tag{24}$$

2.1.3 Quarter-wave stack

Suppose a stack of thin films, where there are two alternating dielectric layer materials. The material with higher real refractive index n will be denoted with H, and similarly the lower index n material will be denoted L. The layer media alternate, forming a HL-stack with $j-1$ perfect quarter-wave optical thickness (QWOT) layers. In other words, every layer has an optical thickness $d = \lambda_0/4$. The λ_0 can be called the central or the reference wavelength of the coating. Transmittance across a film with optical thickness d is:

$$\frac{\partial T}{\partial d_i} = C\frac{2\pi d_i}{\lambda}\sin\phi_i\,, \tag{25}$$

where

$$\phi_i = \frac{4\pi d_i}{\lambda}$$

is the phase change of the reflected light wave [8]. A normal incidence angle is assumed. Since for every layer $d_i = \lambda/4$ it follows that $\partial T/\partial d_i = 0$. Now suppose that layer j is deposited with $d_j \neq \lambda/4$, from which it follows that $\partial T/\partial d_j \neq 0$. Then layer $j+1$ can be deposited with thickness d_{j+1} so that the total phase change through $j+1$ layers is $\phi_1^{j+1} = (j+1)\pi$. This condition can be fulfilled when

$$\phi_1^{j+1} = \phi_1^j + \frac{4\pi d_{j+1}}{\lambda} = (j+1)\pi\,.$$

This shows that a thickness error in layer j can be compensated for by giving layer $j+1$ a thickness $d_{j+1} \neq \lambda/4$ as long as transmissivity over the structure fulfils

$$\frac{\partial T_1^{j+1}}{\partial d_{j+1}} = 0\,.$$

This is the basis of layer thickness error self-compensation phenomenon in the optical monitoring. Its practical value will be discussed further in section 3. However, as layer optical thickness d is dependent on the layer material's refractive index n and furthermore dependent on λ, the error self-compensation only functions at wavelengths equal to or near λ_0. For other wavelengths the optical thickness errors can not be compensated.

Consider a multilayer QWOT stack with alternating high- and low-index layer materials with respective refractive indices n_{H} and n_{L}. The stack has $2j+1$ layers, with high index material as the outermost layers. The substrate has refractive index n_s, with exit medium being air. For such a stack the reflectance will be:

$$R = \left(\frac{1-(n_{\mathrm{H}}/n_{\mathrm{L}})^{2j}(n_{\mathrm{H}}^2/n_s)}{1+(n_{\mathrm{H}}/n_{\mathrm{L}})^{2j}(n_{\mathrm{H}}/n_s)}\right)^2\,. \tag{26}$$

Increasing the layer count will increase the total reflectance of the system. [7, p. 165] This is graphically demonstrated in figure 2.

The width of the high-reflectance region of a symmetric QWOT stack can be shown to be dependent only on the layer refractive indices, but not on the layer count. The width of the reflective region is $2\Delta g$, where Δg is defined by

$$\Delta g = \frac{2}{\pi}\sin^{-1}\left(\frac{n_{\mathrm{H}}-n_{\mathrm{L}}}{n_{\mathrm{H}}+n_{\mathrm{L}}}\right)\,. \tag{27}$$

Therefore the width of the reflective region is dependent only on the refractive indices n_{H} and n_{L}. [7, p. 170] This is demonstrated graphically in figures 2 and 3.

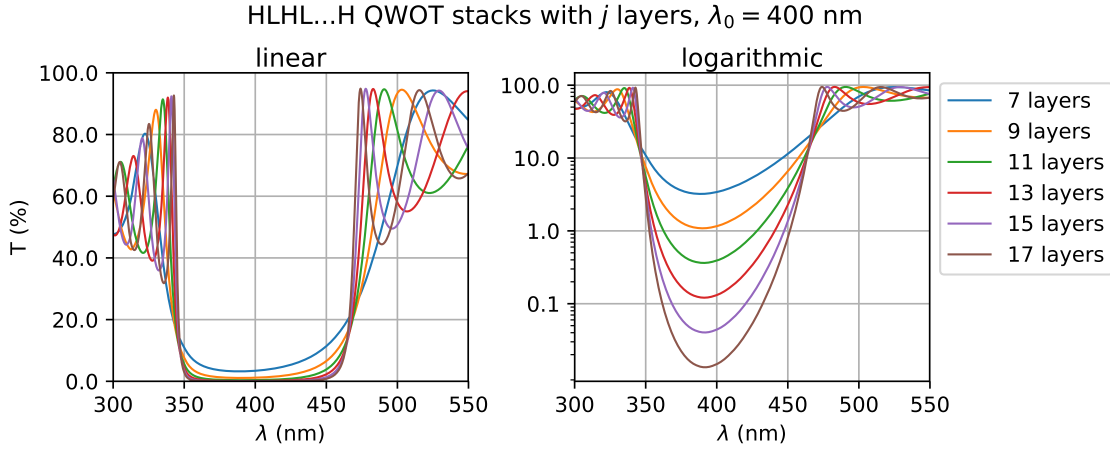

Figure 2. Computational transmittance profiles for various QWOT stacks with $\lambda_0 = 400$ nm. The T-axis is scaled linearly in the left graph, and logarithmically on the right. Adding more layers to the stack improves the reflectivity of the high-reflectance region, as can be seen in the logarithmic plot. However, adding layers with a constant thickness does not widen the blocking region, as can be seen in the linear plot.

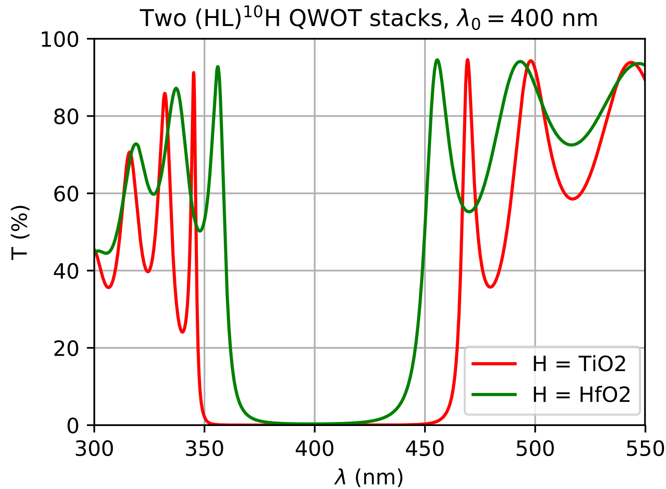

Figure 3. Computational transmittance profiles for two 21 layered stacks with structure $H(HL)^{10}$, where H and L are QWOT layers of high and low refractive index materials. The red stack has TiO_2 ($n = 2.59$) as the high index material, and the green stack has HfO_2 ($n = 2.16$). Both stacks use SiO_2 ($n = 1.47$) as the low index material. The stack with TiO_2 has a wider blocking region and better performance due to higher contrast between refractive indices of the layer material. Lower contrast would be useful if the blocking region should be narrow.

One more property of a QWOT stack is that with a normal incidence angle $\theta_0 = 0°$ its characteristic matrix reduces to

$$\pm \begin{bmatrix} 0 & \mathrm{i}/\eta_r \\ \mathrm{i}\eta_r & 0 \end{bmatrix}$$

when $\lambda = \lambda_0/q$ and q is an odd positive integer 1, 3, 5...

Adding another QWOT layer with admittance η to a QWOT stack assembly alters its admittance to η^2/Y. Therefore the total admittance of such an assembly, with j layers, can be calculated by

$$Y = \frac{\eta_1^2\eta_3^2\cdots\eta_j^2}{\eta_2^2\eta_4^2\cdots\eta_e} \tag{28}$$

when the layer count is odd, or

$$Y = \frac{\eta_1^2\eta_3^2\cdots\eta_{j-1}^2\eta_e}{\eta_2^2\eta_4^2\cdots\eta_j^2} \tag{29}$$

if the layer count is even. [7, p. 46]

2.1.4 Absorption bandpass filter

An absorbing metal layer will have a maximum transmissivity value T_{max}, called potential transmittance. The potential transmittance is defined by the refractive index $N = n - \mathrm{i}k$ of the metal at a certain wavelength as well as its thickness t. Let us assume a normal incidence angle $\theta_0 = 0°$ for light. For a metal layer the potential transmittance is given by equation:

$$T_{max} = \frac{T}{1-R} = \frac{\mathrm{Re}(Y)}{\mathrm{Re}(AC^*)} \tag{30}$$

where $Y = X + \mathrm{i}Z$ is the exit admittance of the layer. A and C are defined by the characteristic matrix of the metal layer:

$$\begin{bmatrix} A \\ C \end{bmatrix} = \begin{bmatrix} \cos\delta & (\mathrm{i}\sin\delta)/N \\ \mathrm{i}N\sin\delta & \cos\delta \end{bmatrix} \begin{bmatrix} 1 \\ X + \mathrm{i}Z \end{bmatrix}$$

The δ was defined in equation 19 as

$$\delta = 2\pi Nt/\lambda = 2\pi nt/\lambda - \mathrm{i}2\pi kt/\lambda = \alpha - \mathrm{i}\beta\,.$$

Potential transmittance T_{max} is therefore given by:

$$
\begin{aligned}
T_{max} = \Bigg(& \frac{(n^2 - k^2) - 2nk(Z/X)}{n^2 + k^2} (\sin^2\alpha \cosh^2\beta + \cos^2\alpha \sinh^2\beta) \\
& + (\cos^2\alpha \cosh^2\beta + \sin^2\alpha \sinh^2\beta) \\
& + \frac{1}{X} (n \sinh\beta \cosh\beta + k \cos\alpha \sin\alpha) \\
& + \frac{X^2 + Z^2}{X(n^2 + k^2)} (n \sinh\beta \cosh\beta - k \cos\alpha \sin\alpha) \Bigg)^{-1}
\end{aligned} \tag{31}
$$

The exit admittance $Y = X + \mathrm{i}Z$ can be optimized by finding optimal values for X and Z so that T_{max} in equation 31 will reach its extremum. The optimal values will be:

$$
X = \left(\frac{(n^2 + k^2)(n \sinh\beta \cosh\beta + k \sin\alpha \cos\alpha)}{n \sinh\beta \cosh\beta - k \sin\alpha \cos\alpha} - \frac{n^2 k^2 (\sin^2\alpha \cosh^2\beta + \cos^2\alpha \sinh^2\beta)^2}{(n \sinh\beta \cosh\beta - k \sin\alpha \cos\alpha)^2} \right)^{1/2} \tag{32}
$$

and

$$
Z = \frac{nk(\sin^2\alpha \cosh^2\beta + \cos^2\alpha \sinh^2\beta)}{n \sinh\beta \cosh\beta - k \sin\alpha \cos\alpha} \tag{33}
$$

Derivations for these equations can be found in Macleod's book *Thin-film optical filters.* [7, p. 295-298]

2.2 Fabrication methods

There is a wide variety of coating techniques available for thin film manufacturing. In this section a few of the most important ones will be briefly introduced.

Deposition methods are generally divided into two categories: physical and chemical vapour deposition methods (PVD and CVD respectively). PVD techniques include thermal evaporation techniques and sputtering, which will be introduced. Molecular beam epitaxy, laser ablation, ion plating and cluster deposition techniques can also be categorized as PVD techniques, but they are uncommon in optical manufacturing and therefore will not be discussed here. CVD techniques involve volatile molecular precursors, which cause the coating process to undergo chemical reactions. Atomic layer deposition is a variation of CVD technique capable of depositing a layer within accuracy of a single molecule length.

2.2.1 Thermal evaporation

In thermal evaporation a target material is heated until it boils and evaporates. The vaporized molecules then travel to the relatively cool substrate and condense on it forming a film. The substrates are often heated to $200 - 300$ °C to improve an even film formation. The vaporized molecules travel straight from the evaporation source until they collide with other atoms or molecules. This imposes some challenges on thermal evaporation deposition. First of all, the deposition has to be performed in a high vacuum in order to minimize the prevalence of intermolecular collisions as well as the chance of film contamination or oxidation. Second, the coating materials are deposited in line-of-sight impingement. This means that the coating uniformity can become compromised on uneven substrate surfaces. Especially large substrates can be problematic to coat uniformly, since different parts of the substrate will have non-equivalent distance to the evaporation source. Ridges or steps on the substrate can also block the line-of-sight from the evaporation source resulting in under- or uncoated regions called "shadows". [9]

Originally heating of the material in thermal evaporation was achieved by placing the coating material in a conductive container and then running a high current through the container. The current causes the container to heat due to electric resistance, and the heat transports to the evaporant material. This is called resistive heating, and it has been used up to this day. Downsides of resistive heating are that the rapid deposition can be difficult to control accurately, and the container may induce impurities by reacting with the evaporant material or by releasing particles when heated. However, resistive heating is a simple and cost-effective deposition method with high deposition rate. Metals like silver and aluminium are especially suitable for resistive heating, as they have relatively low melting point temperatures and their exact thickness is rarely important in coatings such as mirrors.

Another heating method that has on many instances surpassed resistive heating in industrial use is the electron beam evaporation. A high-energy electron beam (e-beam) is directed towards the coating material using magnetic fields. The electron bombardment causes the evaporant to melt locally. E-beam evaporation is not as vulnerable to outside contamination as the evaporation happens locally at the e-beam contact point, and the evaporant container can be watercooled in order to avoid heating it up. E-beam evaporation does carry a risk of X-ray damage on the substrates [9]. Generally e-beam evaporation allows for versatile, stable and easily

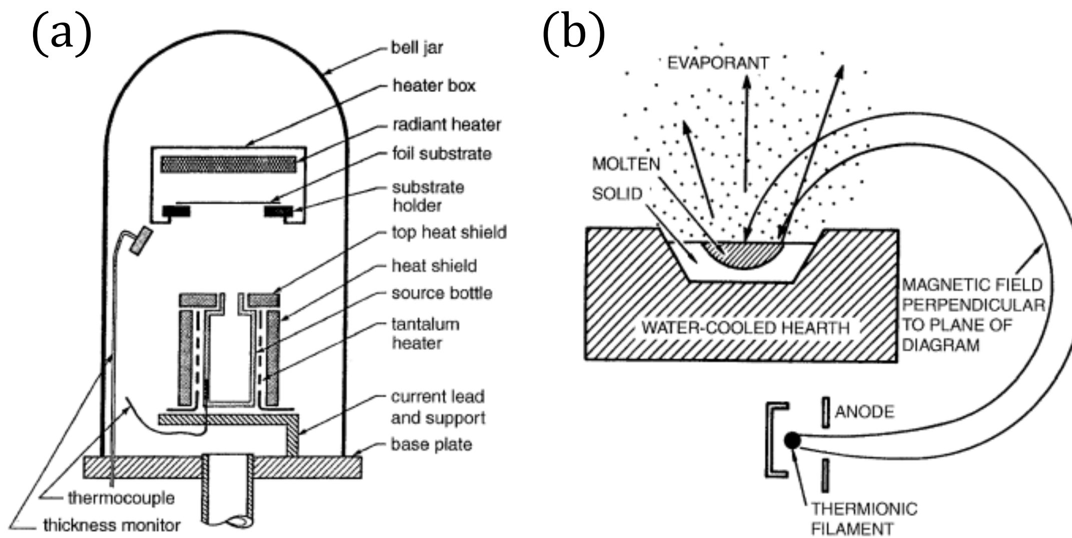

Figure 4. **(a)** An example of a thermal evaporation setup using resistive heating. **(b)** A diagram demonstrating the electron beam evaporation. A magnetic field deflects the electron beam into the evaporant crucible, melting the loaded material. [9]

controllable deposition method which, when coupled with a high vacuum, allows for good quality film fabrication. Another common evaporation method is to use RF induction coils for heating. In figure 4 a typical resistive evaporation system as well as a diagram for the e-beam evaporation are shown.

Vacuum evaporation can be enhanced by utilising plasma ion bombardment in a technique referred to as plasma-ion assisted deposition (PIAD). By transferring kinetic energy of charged ions onto the substrates the deposited molecules gain extra mobility and become able to move on the substrate surface to more energetically beneficial locations [10]. Ion bombardment grants the benefits of heating the substrates without actually heating them, which avoids problems with thermal expansion and induced stress in the coating. A thin film produced utilizing ion bombardment will have properties close to bulk material, like tighter packing density, higher refractive index and less absorptivity compared to conventionally evaporated films. PIAD also improves adhesion and durability of thin films. [11]

2.2.2 Sputtering

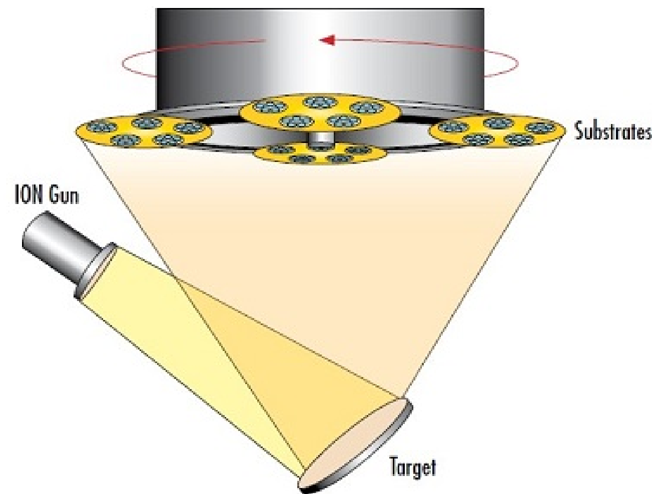

Figure 5. A schematic of ion beam sputtering deposition. [12]

Sputtering utilizes charged particles provided by a plasma source, which are then bombarded against a target material. The ions knock off the surface atoms of the target when colliding, and then the knocked off atoms travel to the substrate, where they nucleate and form a layer. Sputtering does not evaporate the coating material, but instead uses momentum transfer to achieve a similar result. As opposed to thermal evaporation techniques, sputtering does not require heating of the target material. Therefore the distance between the sputtering target and the substrate can be much shorter than during the thermal evaporation, as heat transfer by radiation is not an issue. Comparatively large targets can be used as well. [9]

A distance as short as possible between the target and the substrate in a sputtering system is necessary for a few reasons. First, the gas pressure in a sputtering system is orders of magnitude higher than in an evaporation system. A gas pressure of 10^{-3} mbar is common for a sputtering system, whereas an evaporation system usually requires a vacuum of 10^{-6} mbar. particles have a much shorter mean free path through the gaseous medium and lose energy through collisions rapidly. Second, a sputtering system has a relatively low flow of deposited particles, which results in low deposition rates. The low deposition rates can be compensated by increasing the target size. Sputtering has a few advantages over vacuum evaporation techniques. The short distance between the target and the substrate results in a good material

utilization factor. If a wide target is used, sputtering also has great conformation and is able to deposit behind corners without layer uniformity suffering. [13]

There exist a few variations in sputtering techniques. Probably the two currently most relevant for thin film deposition are ion beam sputtering and magnetron sputtering.

In ion beam sputtering (IBS) an ion gun is used to accelerate and fire a beam of ions towards the target. IBS can work in a vacuum similar to an evaporation system, thus avoiding many of the problems with regular sputtering systems and allowing for coating conditions to be better controllable. The low operating pressure also permits the sputtered particles to obtain longer mean free path and thus retain high kinetic energies. Thus IB sputtered films can be very dense, but may also be prone to high compressive stress. Unfortunately, ion beam sputtering as of now is limited to very low deposition rates ($0.5 - 5$ Å/s). Also certain materials such as fluorides are easily damaged by ion collissions and are therefore not suitable to be deposited using sputtering methods [14]. Ion beam sputtering as of now is mostly used in research and in production of specialty films.[13, 15]

In a magnetron sputtering system a strong electric field is introduced between the target material (cathode) and the substrates (anode). Plasma is generated near the target material, which will release ionized atoms to bombard the target material due to the electric field. Magnetic fields configured parallel to the target are used to trap the free electrons near the target where the plasma is located. This not only helps in maintaining the plasma source, but also prevents the electrons from bombarding the positively charged substrates. Magnetron sputtering reaches better plasma ionization rate than regular sputtering, which in turn leads to higher deposition rates and allows the plasma discharge to be maintained in lower operating voltage and pressure. [16]

Even though sputtering and thermal evaporation are both considered PVD techniques, each of them offer advantages and disadvantages over the other. Sputtering systems offer higher film uniformity, purity and film properties. Arguably higher quality coatings can be produced using sputtering systems, made evident by sputtering systems being used when producing high performance coatings with large layer counts [4, 5, 17, 18]. Also sputtering targets can be comparatively large and not as limited in their capacity to hold evaporant materials as the small crucibles of thermal evaporation systems. However, thermal evaporation systems can utilize a wider selection of materials. Compared to sputtering, thermal evaporation systems

also offer faster deposition rates, compatibility with plasma-assist sources, and are generally more straightforward as well as cheaper.

2.2.3 Chemical vapour deposition

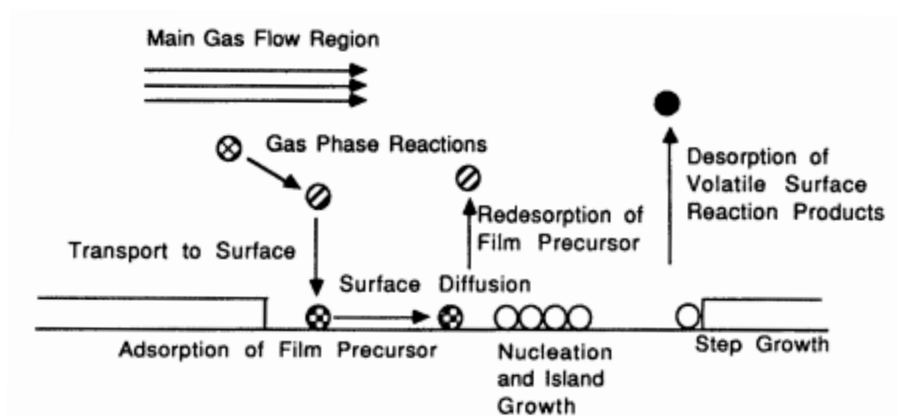

Figure 6. A schematic depicting the reaction process of chemical vapour deposition. [9]

In chemical vapour deposition (CVD) the thin film is fabricated through chemical reactions. Whereas in physical deposition methods the coating material travels to the substrate physically, in CVD the coating material is led to the coating chamber as a gas or vapour. The coating happens chemically and therefore requires presence of volatile precursor molecules as well as sufficient activation energy for chemical reaction to occur. The activation energy has to be supplied locally to the substrate in order to restrict the deposition on the substrates and avoid deposition elsewhere in the chamber. The activation energy can be supplied by thermal heating of the substrates, by generating DC, AC or RF voltage to the substrate, or by a laser. The chemical reaction produces gaseous by-products, which are pumped out of the chamber. A schematic of a CVD process can be seen in figure 6. The main advantage of CVD over PVD is its commendable layer conformality. CVD is not restricted by evaporant source's line-of-sight, but is able to evenly coat uneven surfaces and around corners. CVD processes are also fast compared to PVD, but the produced films may not be as environment resistant. [15]

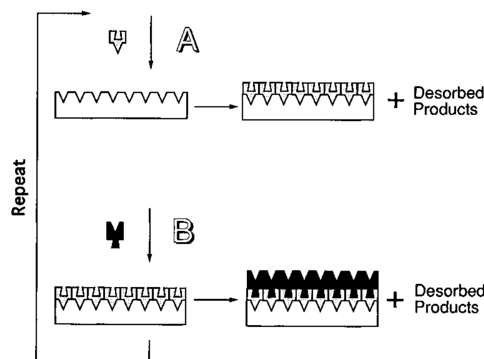

Figure 7. The principle of a binary ALD process. Precursor A attaches to the bare substrate during the first deposition cycle, and to precursor B on later cycles. Precursos B reacts with the precursor A and forms the finished layer. The deposition is self-limited by available reaction sites. Between the deposition cycles the desorbed products and excess precursors are flushed out of the chamber.[19]

2.2.4 Atomic layer deposition

Atomic layer deposition (ALD) is a relatively new deposition method. It was originally known as atomic layer epitaxy but developed into a more general non-epitaxial deposition method known as ALD. It can be considered to be a variation of CVD technology. ALD is based on a sequential monolayer fabrication that allows for layer thickness control within accuracy of a single molecule length. Substrates are loaded into a chamber, after which gaseous molecular precursors are let into the chamber. The precursor molecules attach to the substrate forming a monolayer on it. This layer is only a single molecule length thick, as the precursors can only attach to the free area of the substrate surface. After the substrate is fully covered an inert carrier gas (for example N_2 or Ar) is used to flush out the non-attached excess precursors and any reaction byproducts. Next, new molecular precursors are let into the chamber. These molecules chemically react with the previously deposited molecule layer. After the reactions have saturated the excess molecules are again flushed out of the chamber using a carrier gas. This process is then repeated by alternating between the precursors until the desired coating thickness has been reached. This process is depicted in figure 7. Because the molecular interactions are limited by available reaction sites, the ALD essentially is a self-limiting deposition process. The layer thicknesses can therefore be controlled within one molecule

length accuracy as a single process cycle always deposits a single monolayer. Layers produced by ALD have an outstanding layer uniformity and conformality. As far as film quality is concerned, ALD is often superior to the other deposition techniques. The disadvantages of ALD stem from its complexity. The choice of ALD coating materials is limited by the reaction pathways of the materials. Therefore some materials, or their combinations, are unusable in an ALD process. Some specific reactants may also be difficult or expensive to procure. Furthermore, due to its cyclic nature ALD processes are very slow, often having deposition rates of about $100 - 300$ nm/h. [20, 21]

3 Optical monitoring

3.1 Overview of optical monitoring

The possibilities of multilayer thin films are staggering in the field of optical coatings. However, more complicated coatings can be highly sensitive to layer thickness errors. In order to achieve desired end results, highly accurate and stable layer thickness monitoring techniques are required. While quartz crystal monitoring (QCM) is a well-established and sufficiently accurate monitoring method, it has certain shortcomings. Particularly high layer count structures can be problematic for QCM due to cumulative layer thickness errors. It is also noteworthy that QCM measures layer's physical thickness, which in itself has very little relevance on the optical properties of a coating.

Instead of the physical layer thickness, it is possible to measure the optical thickness instead. In optical coating design, fabrication and monitoring the optical thickness is more relevant than the physical thickness. Optical layer thickness tells what the optical path length of light is across a layer, which in turn is responsible for the optical properties of the coating.

In optical monitoring either a transmitted or reflected signal of a substrate is actively measured during the deposition process. The substrate becomes coated during the deposition and therefore exhibits optical properties of the coating as it is developing. From these changes in either transmittance or reflectance the optical thickness of the developing layer can be determined. The monitored substrate is called the monitoring glass. Either a single or multiple monitoring glasses may be utilized during a fabrication process, depending on how the process was designed. Depending on the equipment the monitoring glass's optical behaviour can either be measured on a single wavelength or across a spectrum.

Optical monitoring has existed for almost as long as the thin film coating technologies. In the beginning optical monitoring was limited to single wavelength monochromatic monitoring and coatings consisting entirely of layers with quarter wave optical thickness (QWOT). The monitored signal would reach its local minimum

and maximum points, so called turning points, exactly when the optical thickness of the deposited layer was equal to a quarter of the monitoring wavelength. Therefore the monitoring process was quite straightforward. This monitoring technique became known as turning value monitoring. [22]

Only a few types of optical coatings can be produced using exclusively quarter-wave layers. These include structures such as dielectric mirrors, also known as Bragg Mirrors, or Fabry-Perot bandpass filters. Coatings such as broad bandpass filters and edge filters instead have to contain non-QWOT layers in order to reach great performance. Therefore turning value monitoring can not be used when using a single monitoring wavelength. The layers will have to be terminated at certain transmittance levels, which can be anywhere between the transmittance signal's minimum or maximum values. This can be called either level-monitoring or trigger point monitoring. [23]

Optical monitoring also carries a certain level of layer thickness error compensation as was discussed in section 2.1.3. This is one major advantage of optical monitoring over physical monitoring. If, for example, QCM suffers from a systematic error factor then collective error will be accumulated for every layer in the coating. With simple or low layer count structures this may not be an issue, but complex high layer count coatings will have their spectral performance degraded. Of course thickness error sensitivity depends on the coating design, but even a systematic 0.5 % relative layer thickness error can ruin a complex coating. Optical monitoring, however, is able to compensate layer thickness errors. This error self-compensation effect has been observed both computationally and empirically. In 1972 Bousquet et al showed computationally that narrow bandpass filters could tolerate layer thickness errors up to 10 % while retaining satisfactory optical properties when using optical layer thickness monitoring [8]. The same year H.A. Macleod used theoretical and computational methods to also arrive to a conclusion that optical monitoring is capable of auto-correcting considerable layer thickness errors [24]. This initial research only considered simple QWOT assemblies. However, similar results have been achieved for non-QWOT stacks when the optical monitoring system is coupled with a computer, allowing for real-time layer termination adjustment and error compensation [25, 26].

The error self-compensation effect in optical monitoring is a consequence of the fact that layer thickness errors are not independent of each other. Any deviations

in a layer thickness change the optical behaviour of the entire structure and affect the upcoming layer behaviour as well. A layer with incorrect layer thickness will introduce a phase change in transmitted signal. When depositing the next layers, this phase change is countered by terminating the layer at a point where the system total phase change is again correct. In this way all the layer thickness errors are dependent on each other. While error cumulation is still possible, it is not systematic in one direction. [27]

3.2 Different optical monitoring systems

There are different techniques to optical monitoring, but first let us summarize what they have in common. Optical monitoring requires a monitoring test glass to be loaded in the deposition chamber so that the monitoring glass will become coated on one side during the deposition process. A light source is directed towards the monitoring glass, and a detector measures the intensity of the signal that was either transmitted through the glass or reflected from it. The detector is always outside of the deposition chamber, but the light source may or may not be inside the chamber depending on whether transmittance or reflectance of the monitoring glass is measured. As the monitoring glass becomes coated, its optical properties change as well. These changes in optical behaviour are monitored in real-time and when certain conditions are met (for example a certain amount of signal turning points are found) the layer deposition is terminated.

The most important distinction between optical monitoring techniques is whether a single wavelength or a broad band is used for monitoring. These techniques are called monochromatic monitoring and broadband monitoring, respectively. Both of the methods can be further divided into direct and indirect techniques. [22]

3.2.1 Direct and indirect monitoring techniques

In direct monitoring the transmittance or reflectance measurement is performed on one of the production substrates as it becomes coated. Indirect monitoring uses either one or several monitoring glasses physically separated from the production substrates. In other words, the indirect monitoring glasses are not located on the production substrate holders, but could be placed, for example, in a revolving magazine in the chamber ceiling.

Both direct and indirect techniques have their own advantages and disadvantages. Direct monitoring is more straightforward to use, as it monitors the actual coating deposited on production glasses. On the contrary, since indirect monitoring utilizes monitoring glasses that are physically in a different location than the production glasses, the monitoring glasses may become coated at a different rate than the production substrates. This can be corrected by determining calibration factors or by controlling deposition rate with a physical mask. Deposition distribution optimization is often easier when using direct monitoring methods. However, indirect monitoring can allow the monitoring glass to be changed in-between layer depositions, if the glasses are loaded in a revolving magazine. Some long processes may have to be monitored using multiple monitoring glasses, and a magazine allows the monitoring glasses to be changed without stopping and restarting the entire deposition process. When using direct monitoring the monitoring glass can not be changed without stopping the process, opening the deposition chamber and swapping the glass manually.

3.2.2 Broadband monitoring

In broadband monitoring (BBM) the transmittance or reflectance of the coating is monitored across a wide spectrum of wavelengths and then compared to a theoretical model. Multiple detectors can be employed to measure the optical spectrum. The spectrum is then compared to a theoretical model to estimate the layer optical thickness. Layer deposition termination is calculated from the time derivative of the layer's thickness growth.

The amount of data points gathered in a single BBM spectrum can be in hundreds or even thousands when using modern equipment. This allows an accurate estimation of the actual layer thickness. One of the most important features of BBM is its low sensitivity to random measurement errors in the signal. Layer thickness error self-compensation can be present in the BBM processes like in monochromatic monitoring [26]. However, as opposed to monochromatic monitoring, the error self-compensation in a BBM system is more dependent on the exact design of the coating. Therefore it is recommended that multiple design choices should be investigated in pre-production when using BBM. [22]

3.2.3 Monochromatic monitoring

In monochromatic monitoring (MM) a single wavelength of the transmitted or reflected light is observed. As the light source is typically a broadband source, the unnecessary wavelengths have to be filtered out. This can be achieved by guiding the collected light through a monochromator before it reaches a detector.

In figure 8 an example of a monochromatic transmittance signal is presented as a function of layer optical thickness. As the thickness of the deposited layer grows, the monochromatic signal acts like a sine function. Whenever the signal hits a local minimum or maximum (i.e. a turning point) the signal is experiencing either a maximum or minimum destructive interference at that point, respectively. After passing a signal turning point the next turning point will be reached after depositing a precise QWOT layer. Using turning points as a reference the monitoring system can estimate at which signal level the desired layer thickness will be reached. The layer deposition will then be terminated when that level is reached. For example if the first layer of the structure would be 2.5 quarter waves thick, the layer termination would take place after the second turning point when the the signal strength is equal to the average of the signal maximum and minimum.

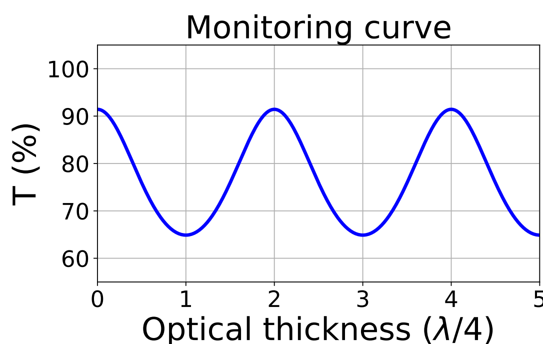

Figure 8. An example of a monochromatic transmittance signal as a function of layer optical thickness (units in quarter wavelengths). The layer material in this case is TiO_2.

4 Experimental methods

4.1 Computational methods

Most optical coatings are fairly complex by their structure, and their optical properties are often impractical to solve analytically. Fortunately efficient computational methods have been developed to be utilized in designing optical coatings. There are commercial softwares available specifically geared towards optical coating design. The softwares offer tools for determining optical behaviour of coatings — for example, their transmissive or reflective spectra — and for assisting in the design of coatings or even creating entire designs from scratch.

4.1.1 Used software

Two programs were used during the coating design process in this work. The first one was a thin film software OptiLayer [28], version 9.96q. OptiLayer was used for designing the structures of the optical coatings. OptiLayer allowed to computationally estimate spectral properties of the coatings and offered automated methods for refinement of the structures. OptiLayer also has a single wavelength monitoring tool, which was useful for deciding optimal monitoring wavelengths. Additionally two modules for OptiLayer, OptiChar and OptiRE, were used for certain tasks. OptiChar is a thin film characterization module. It was used to determine refractive indices of the used evaporant materials and substrates. OptiRE is a module for reverse engineering a finished coating from its spectral data. It allows for approximation of possible layer thickness errors, layer inhomogeneity and refractive indices correction.

Virtual deposition processes were performed with a simulation program OMSVis (version 2.8.010), developed by Leybold Optics Gmbh. With OMSVis it was possible to simulate monochromatic monitoring in a virtual deposition processes for the coatings designed in OptiLayer. Monitoring parameters could be adjusted and certain error factors (measurement signal noise, refractive index drift, layer termination delay etc.) could be introduced in the simulations. The virtual coatings accumulate

layer thickness errors, which could be seen after the simulation run as well as the resulting transmittance spectrum of the coating. After designing a coating with OptiLayer, simulations were run with OMSVis on that design to estimate if the deposition was practical and robust. The most important parameters to experiment with OMSVis are the monitoring wavelength, the monochromator slit size, Gain Signal Average (GSA) value and the layer termination algorithms.

Monochromator slit size controls the width of the monochromator exit slit. The slit width affects the bandwidth of the light signal arriving at the detector. The smaller the slit is, the narrower the broadband will be, resulting in better measurement accuracy. However, narrower slit also reduces the measured signal strength, thus increasing the relative amount of noise in the signal. A slit size of 1.0 mm corresponds to approximately 4.4 nm bandwidth for the collected light.

GSA is a multiplier used when automatically calculating a settling time. Settling time determines a window for a computational filter that takes a certain amount of recent monitoring data points and averages them in order to reduce signal noise. The smaller the GSA value is, the smaller the settling window will be, which may lead to inaccuracies if the signal is noisy. However the longer settling window may, in turn, lead to inaccurate signal turning point detection. GSA value should be an integer between 1 and 5, and can be decided by running test simulations with each value. Normally GSA value of either 3 or 5 is used.

Layer termination algorithms are required because the actual monitored transmittance and reflectance signals do not match the theoretical model exactly. The actual refractive indices of materials may slightly change because of layer inhomogeneity or a shift in refractive indices, which are exceedingly difficult to predict in the theoretical model. The optical monitoring system (OMS) uses transmittance and reflectance levels to determine when a layer has to be terminated. However, due to the mismatch between theoretical signal and real monitored signal, this termination level has to be adjusted during the process to ensure that layer deposition is terminated at the correct signal level [22, 29]. The signal level for layer termination is called a trigger point. This is done by measuring the actual reflectance or transmittance values and comparing them to the theoretical model. Three different points of the monitoring signal can be used to evaluate the relative mismatch between the actual monitoring signal and the theoretical signal. These points are shown in figure 9. The actual signal level of the trigger point can then be determined by estimating the

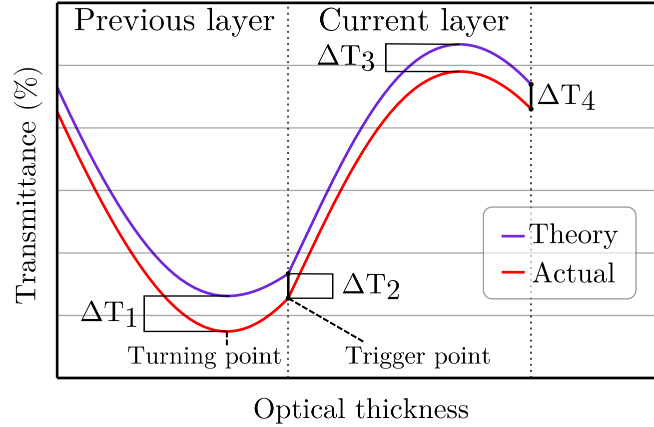

Figure 9. A diagram of theoretical and "actual" transmittance monitoring signals during a deposition process. OMS layer termination algorithms use the signal differences ($\Delta T_1 - \Delta T_3$) to determine an offset ΔT_4 for the layer trigger point. ΔT_1 is found at the second to last turning point and can be located in the previously deposited layer. ΔT_2 is found at the current layer start point. ΔT_3 is found at the current layer's last turning point, if there are any. ΔT_4 is the estimated transmittance difference at the current layer's trigger point.

mismatch of the signals at the upcoming layer termination point and offsetting the theoretical trigger point with the signal mismatch. The correction algorithms adjust the trigger points every time a layer deposition starts and at each local extrema of the monitoring signal.

There are three termination algorithms available: OFFSET, BACKWARDS and FORWARD. The OFFSET-algorithm sets the trigger point offset (ΔT_4) equal to the absolute difference between the theoretical and monitoring signal at the layer start point (ΔT_2), i.e. $\Delta T_4 = \Delta T_2$. This algorithm is useful for the first layers that do not contain turning points. BACKWARDS-algorithm uses the signal differences at the last two turning points (ΔT_1 and ΔT_3) to approximate the correct trigger point offset ΔT_4. The second to last turning point may be located in the previous layer. FORWARD-algorithm adjusts the trigger point offset ΔT_4 using the signal difference at the current layer's start point (ΔT_2) and a turning point in the same layer (ΔT_3). The more accurate the predicted value for ΔT_4 is the more accurate the layer thickness will be. The evaporation machine manufacturer recommended that generally BACKWARDS-algorithm should be used if the layers contain turning points.

4.1.2 Forming a monitoring strategy

The monitoring wavelength is by far the most important of the monitoring parameters. There are a few general principles which help in finding the optimal monitoring wavelength λ_m. If the structure is a QWOT stack where all layers have optical thickness equivalent to $p\lambda_0/4$ when p = 1,2,3..., then the monitoring wavelength should be chosen to be the same as the central wavelength: $\lambda_m = \lambda_0$. If the layers do not have exactly the same optical thickness, but are almost equally thick, then the monitoring wavelength can be chosen to be slightly shorter than the quadruple of the optical thickness of the thinnest layers. If the layer thicknesses, for example, fall in a region $0.9\lambda_0 - 1.1\lambda_0$ then a monitoring wavelength should be $\lambda_m < 0.9\lambda_0$. This ensures that every layer will have optical thickness $> \lambda_m/4$ and therefore will contain at least one turning point.

In some cases the central wavelength can not be used for optical monitoring. This is usually the case with coatings that have reflecting region at the central wavelength λ_0. These regions are formed when every layer has an optical thickness $\sim \lambda_0/4$. The transmittance or reflectance of this type of stack at the central wavelength will approach $T \approx 0$ % or $R \approx 100$ % as more layers are added. After about a dozen layers optical monitoring will be impossible. Instead the monitoring wavelength should be chosen near the lower wavelength edge of the reflective region. This ensures that all, or at least most, layers will have optical thickness $> \lambda_m/4$. In some cases the shorter wavelength edge may not be possible to use for monitoring. This can happen if the edge resides in the UV-region, in which case the monitoring can be hindered by absorption and UV-incompatibility of the light source or the detector. In these situations a longer monitoring wavelength will have to be used. The λ_m should still be chosen as close to the quadruple of the layer optical thicknesses as possible. If the layer thickness is very thin compared to $\lambda_m/4$, the layer will be difficult to monitor because the phase change across the layer would be comparatively small. Computational methods can be used to predict the shape of the monitoring signal for entire structures and for given wavelengths. This will help in comparing the viability of different monitoring wavelength. This will be elaborated further in the section 5.

When choosing a monitoring wavelength the goal is to have at least one turning point in every layer in the monitoring signal, although sometimes this is not possible. Sometimes the layers without turning points can still be monitored optically if the signal swing between the layer start and termination points is big enough.

Alternatively QCM can be used for these layers. Furthermore the turning points should be located close before the layer termination points to ensure better layer thickness accuracy. Turning points right after the layer start points are prone to introduce errors, but sometimes they have to be tolerated. Generally one should favour the later layers over the early layers, as the later layers can still compensate for layer thickness errors.

The design processes for each of the coatings themselves will be discussed in more detail in the section 5: Design process and results.

4.1.3 Refractive index characterization

It is essential for an optical coating designer to know the optical characteristics of the used materials. Having realistic refractive index models for materials not only helps in trigger point monitoring, as was previously discussed, but also immensely helps the coating design process. Even though common materials have their refractive indices well determined and publicly available [30], the actual refractive indices vary between deposition plants and should therefore be determined experimentally. The refractive index of a material is dependent on its crystalline structure, which can change depending on the used material quality, the deposition parameters and the ambient conditions. Changing deposition parameters such as e-beam current, temperature, plasma parameters and the level of vacuum can affect the packing density and purity of a thin film, which then alters the refractive index of that film. Also oxidation of a film can cause its refractive index to change. For these reasons when aiming to create an accurate theoretical model for an optical coating it is recommended to determine the refractive indices of the used coating materials under same fabrication conditions as the production coatings.

For refractive index characterization a single layer film should be fabricated. Materials with refractive index close to the substrate ($n \sim 1.5$ in case of crown glass) have a poor contrast against the substrates. Poor contrast makes the optical characterization difficult, as the deposited layer will be almost indistinguishable from the substrate. Therefore the substrate should to be chosen so that its refractive index is not too similar to the layer material's index.

The single layer film is then measured with a spectrophotometer. Both the reflectance and transmittance profiles can be used, but there are a couple things to keep in mind. When measuring reflectance it is recommended that the substrate has

a matte surface on the back side. The matte eliminates the unnecessary backside reflectance, although this also results in a loss of absorptivity data or the k-value. Transmittance profile can be measured when using a transparent substrate. Transmittance measurement is generally better for determining the k-value of the refractive index. However the substrate may disrupt the transmittance measurement due to absorption, which is especially relevant in the UV region.

Finally a theoretical layer model has to be fitted into the measurement data. Specialized software is available for this purpose. The layer model may be as simple as a homogeneous non-absorbing film on a smooth substrate, but it can be adjusted to contain bulk inhomogeneity, surface inhomogeneity, absorptivity and irregular dispersion behaviour. When a satisfying data fitting is reached the refractive index model has been determined. The layer thickness can also be determined from the model.

A homogeneous thin film has a constant refractive index N across the entire layer, whereas an inhomogeneous film does not have a constant index. In reality, layer inhomogeneity is present in most thin films to some degree. Layer inhomogeneity inevitably affects the optical properties of the films, as well as entire coatings. Layer inhomogeneity can be used as an advantage in certain coatings such as AR-coatings or rugate filters [31–33], but often homogeneous layers offer optimal design and performance solutions. Layer inhomogeneity may also interfere with the optical thickness monitoring. In the case of simple and non-sensitive coatings the layer inhomogeneities may be ignored. However, complex and sensitive coatings can have their optical performance degraded by layer inhomogeneity. Layer inhomogeneity can be caused by chemical instability of the deposited materials or abrupt changes in the deposition parameters, which disturb the layer growth rate and packing density. [7, 34–36]

In order to demonstrate optical layer characterization OptiChar was used to characterize a single layer of HfO_2. The data fitting and determined refractive index values can be seen in figure 10. The layer was deposited on a transparent silica substrate that has no absorption in $\lambda > 200$ nm region. The model assumed normal dispersion and slight UV-Vis absorption. Bulk inhomogeneity was marginally small for this model, but it contains a moderate surface inhomogeneity. The model fits the data well and the refractive index data seems realistic. The model estimated the layer thickness to be 279.9 nm.

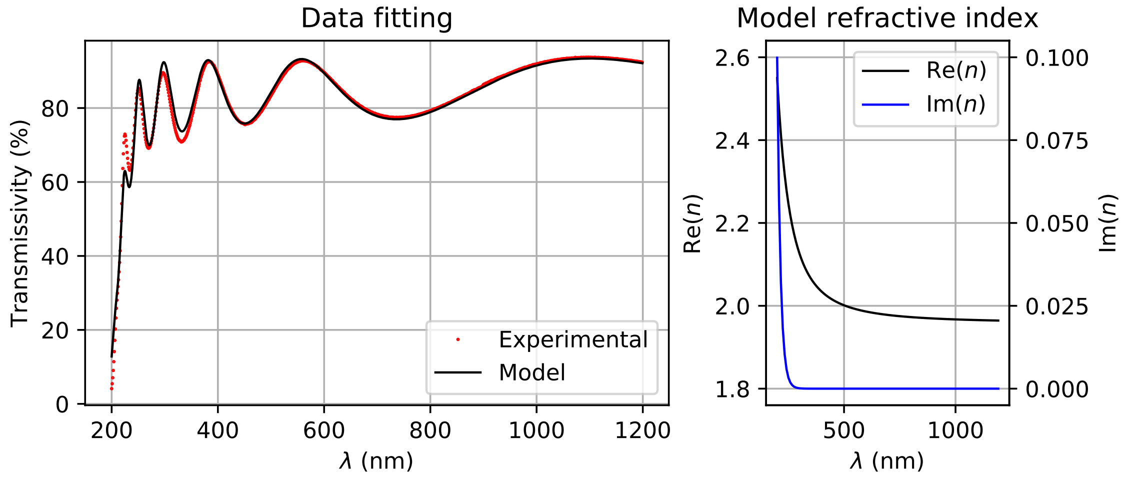

Figure 10. (left) A data fitting of the experimental transmittance data and the theoretical layer model for HfO_2 single-layer. The angle of incidence is 0°. (right) The refractive index profiles of the fitting model.

However, there is always a risk with computational methods, that it is possible to reach incorrect models that still fit the measurement data. An example of this is shown in figure 11. The figure shows a reflectance measurement for a thin (20 nm) Ag single layer on a BK7 substrate and a theoretical model that fits quite decently the measurement data. However the computed refractive indices reveal that the model is unrealistic. The real part of the refractive index, n, is unreasonably large for silver. Babar and Weaver determined that $n < 0.2$ when $\lambda < 2$ μm [37]. Also the model estimated the layer thickness to amount to 209 nm, which is an order of magnitude larger than it should be, and can not be a deposition error. Despite the model fitting the measurement data well, it can be concluded that the model is incorrect.

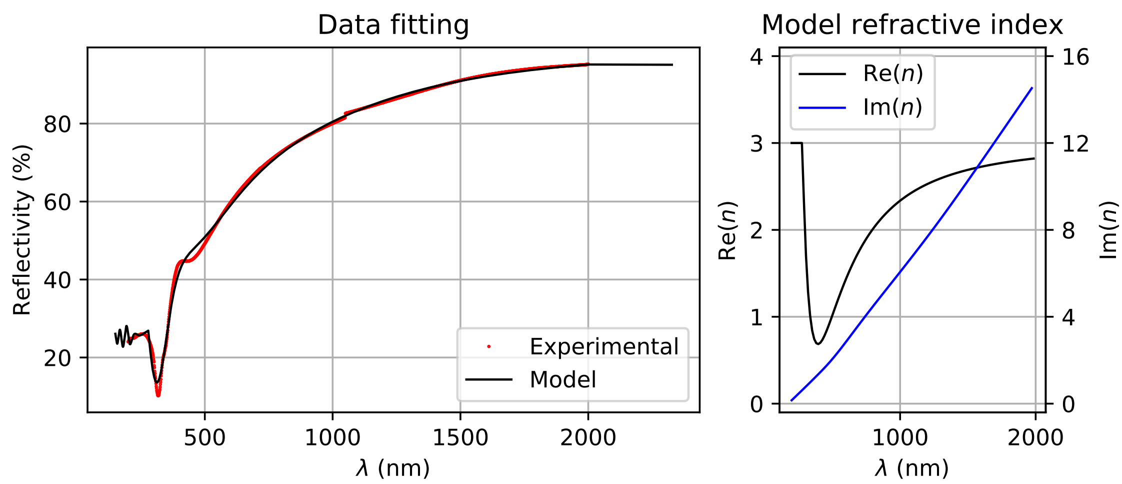

Figure 11. (left) A data fitting of the experimental reflectance data and the theoretical layer model for Ag single-layer. The angle of incidence is 6°. (right) The refractive index profiles for the fitted model.

4.2 Equipment and experimental methods

4.2.1 Coating machine

The coatings were fabricated with a SYRUS*pro* 1110 optical coating production system, by Leybold Optics. It is a plasma ion assisted e-beam evaporation system especially designed for industrial production of optical thin films. A photo of the Syrus' deposition chamber is shown in figure 12. The substrates are held by a spherical, rotating calotte near the ceiling of the deposition chamber. A diagram of the calotte is shown in figure 13. There are two electron beam guns (EBGs) and two rotating crucible holders, one for each electron gun. EBG generates an electron beam which is deflected by magnetic field to a crucible holder. The evaporant material in the crucible melts and evaporates under the e-beam. The crucible acts as a point source for the evaporated molecules. The evaporation can be controlled using shutters to block the vaporized molecules. Resistive evaporation is also possible from a single container called a boat, which is mainly used for evaporating metals like aluminium and silver.

SYRUS*pro* 1110 employs an advanced plasma source (APS) which is located in the middle of the deposition chamber floor. APS generates dense argon plasma that is led into the deposition chamber as an expanding beam. It offers many of the same benefits as the early ion bombardment mechanisms, but also has few advantages. APS guarantees nearly amorphous and especially durable films, and it can be applied to wide substrate areas. In addition to argon the APS also has an optional gas inlet for oxygen. [10, 38, 39] Additionally the plasma bombardment may be used for pre-deposition substrate surface etching. The energetic ions remove contaminants from the surface and can enhance adhesion even further. The central location of the APS ensures even distribution of plasma over the entire calotte. The long distance from the APS to the calotte minimizes the effects of thermal radiation on the substrates.

The deposition machine has both a QCM unit and an intermittent monochromatic transmittance monitoring system installed, and they can both be used during a deposition process. The optical monitoring system is a model OMS 5100 by Leybold Optics. For the intermittent measurement one of the calotte sector plates has to be replaced with an unique sector plate that contains a hole for reference light measurement and a slot for the monitoring glass (also called test glass or 'TG' from

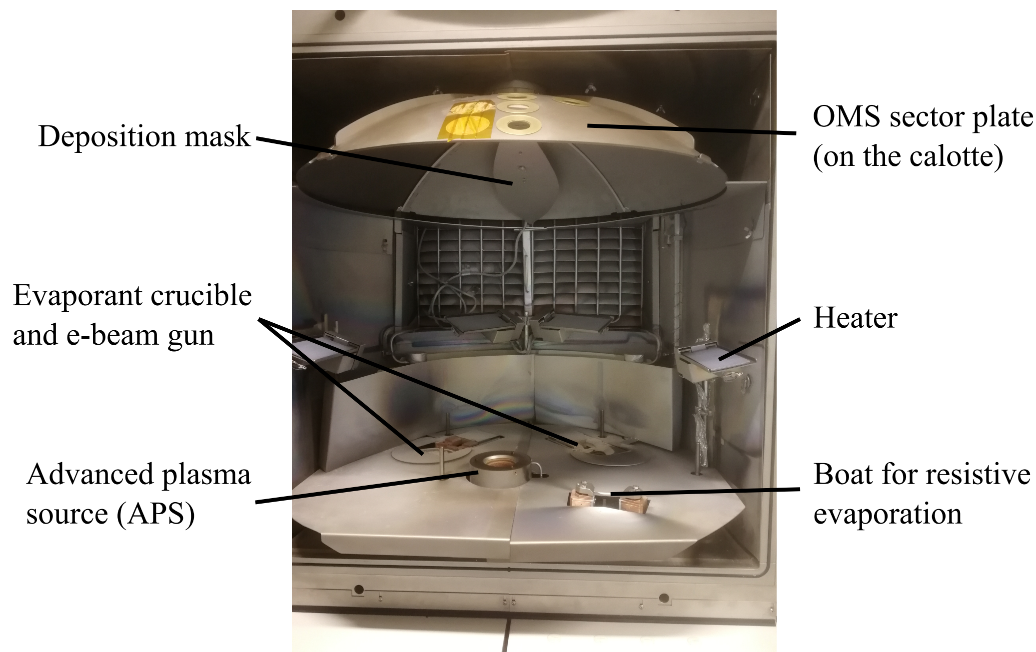

Figure 12. A photo of the coating machine's deposition chamber. Shutters for the crucibles, the APS and the boat have been removed.

here on). A halogen lamp acts as the broadband light source. It is protected from the evaporated material by a leaf-shaped deposition mask. The lamp casts a light beam on the chamber ceiling where the OMS's collimator is located. The calotte rotates between the lamp and the collimator. This set-up is described in figure 14 along the principle of intermittent measurement.

The OMS sector plate has five rows and two columns for substrate slots. The OMS test glass is located on the 3rd row of the plate. The substrates on the third row receive the same amount of deposited material in the same incidence angle as the test glass. The coatings on the other rows differ slightly from that of the test glass due to a slightly different angle of incidence and distance from the EBGs. For this reason the 3rd row usually yields the best results, as their actual coating is almost exactly identical to that of the test glass.

The deposition distribution vertically across the calotte can be optimized by using a deposition mask. The mask shadows a section of the calotte obstructing the deposition proportionally to its size. Because thermal evaporation has no corner conformation abilities, altering the shape of the mask alters the deposition distribution vertically across the rotating calotte. When optimizing the deposition distribution test glasses are loaded into the chamber on every available calotte row. After a

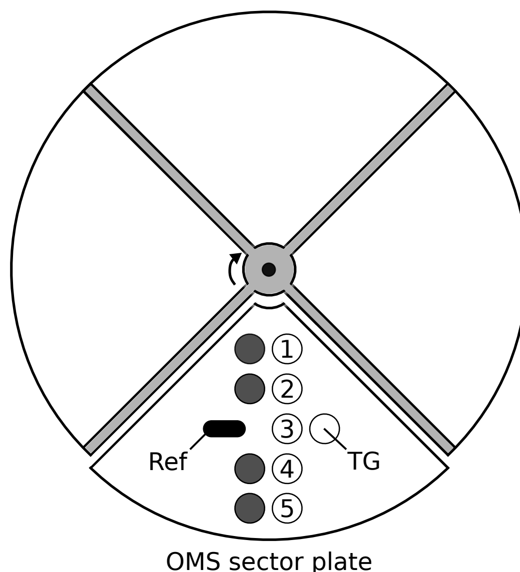

Figure 13. A diagram of the calotte found in the deposition chamber. The calotte is divided into four segments in which the sector plates are placed, supported by the cross-shaped metal frame. The calotte rotates around its central axis. The sector plates contain holes where the substrates are loaded. Sector plates can have differing substrate layouts, but only the sector plate used for intermittent transmittance monitoring is shown here. 'TG' is the slot for the monitoring glass, abbreviated from 'test glass'. 'Ref' is a hole through which the 100 % transmittance signal is measured. Numbered slots are where the substrates were loaded during experiments.

deposition process has been performed either the reflectance or transmittance profile is measured for all the test glasses. In an optimal scenario all the glasses have received an equivalent amount of coating material and therefore they should have identical spectra. If the deposition distribution over the calotte is not optimized the measured spectra will have shifted along the wavelength axis. A shift towards longer wavelengths indicates that the layers are too thick, and a shift towards shorter wavelengths indicates that the layers are too thin. In order to fix thin layers the mask should be narrowed to increase the deposition rate. Respectively by widening the mask thick layers can be corrected. The horizontal deposition distribution is only affected by the sector plate geometry, and therefore should not be of concern unless the plates have become deformed. When depositing sensitive coatings it should

be noted that the deposition distribution is also affected by the APS anode tube geometry.

For evaporant materials common optical dielectrics were used. For low refractive index material SiO_2 was used (Umicore, $1.5 - 3.5$ mm granulates of 99.99 % purity). For high refractive index materials Ti_3O_5 (Umicore, $0.7 - 5.0$ mm granulates of 99.5 % purity) and HfO_2 (COTEC, $1.0 - 2.8$ mm white granulates) were used. Ti_3O_5 has been studied and shown to create robust TiO_2 thin film layers with consistent refractive index when vacuum evaporated [40, 41]. HfO_2 does not have quite as high refractive index as TiO_2 but is better suited for UV-region filters than TiO_2 due to its low absorptivity. Silver (Balzers, $0.7 - 1.5$ mm granulates of 99.99 % purity) was also used in the absorption type filter. Substrate materials used for coatings presented in this thesis were either BK7 or B270, which are common optical glasses with refractive index $n = 1.52$. The B270 substrates (thickness 1 mm) were purchased from SCHOTT. The BK7 raw material was also purchased from SCHOTT, and polished at Millog (thickness 2.5 mm). They have similar optical properties at visible and infrared wavelength region.

4.2.2 Optical monitoring system

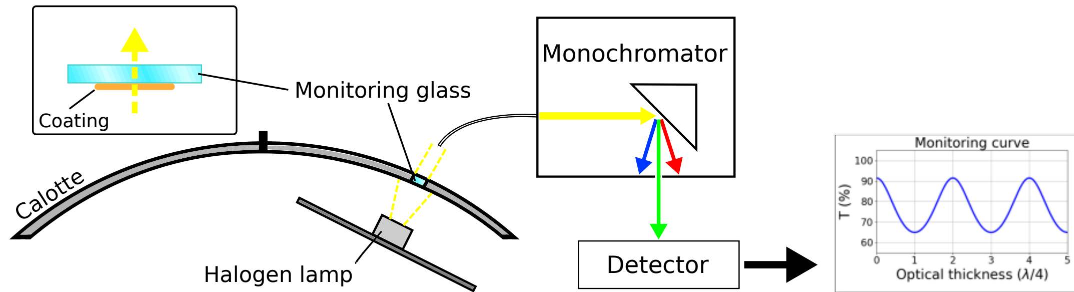

Figure 14. A diagram showing the principle of intermittent transmittance monitoring set-up.

The used optical monitoring system for direct intermittent transmittance monitoring is described in figure 14. A broadband light source, in our case a halogen lamp, is located inside the deposition chamber, facing the calotte. The light is collected by a collimator and led to a monochromator via optic cable. The monochromator uses blocking filters to suppress first and second order maximums from the signal. The

wavelengths are dispersed inside the monochromator with a grating. A narrow band of light with central wavelength equal to the desired monitoring wavelength exits the monochromator to a detector through an exit slit. The width of the monochromator's entrance and exit slits adjusts the measured bandwidth. The narrower the slits are, the narrower the band becomes, which increases the measurement accuracy. However, narrowing down the slits will also decrease the intensity of the detected signal, therefore increasing the noise-to-signal ratio. 1 mm slit width corresponds to a collected spectrum with bandwidth of approximately 4.4 nm. Three detector types with different operating wavelength regions are available. A photomultiplier (PMT) detector can be used for UV region measurements, Si-detector for visible wavelengths and InGaAs-detector for IR-region.

Direct transmittance measurement is performed once per full calotte rotation as the OMS sector plate passes the halogen lamp. Each transmittance measurement requires four individual intensity measurements, which are visualized in figure 15. First a dark reference signal $I_{dark\ ref}$ is measured against a solid part of the calotte, when $T = 0$ %. Second, a reference signal I_{ref} is measured through a hole, with $T = 100$ %. Third, a new dark signal $I_{dark\ int}$ is measured against the calotte before the test glass. Last, the signal I_{int} is measured through the test glass. The dark signals are measured in order to find a baseline for ambient signal. The transmittance intensity of the test glass is calculated by equation

$$T = \frac{I_{int} - I_{dark\ int}}{I_{ref} - I_{dark\ ref}} \tag{34}$$

The calotte rotates with an angular velocity of 33 rpm. Therefore the monitoring glass transmittance can only be measured roughly every two seconds. Accurate layer deposition termination can not be reached with such a long termination time window. Instead the layer termination time should be estimated. The OMS computer observes the transmittance profile and its time derivative constantly, and can estimate a proper time to terminate layer deposition even between transmittance measurements. Shutter delay time can also be compensated for if the delay time is known and consistent.

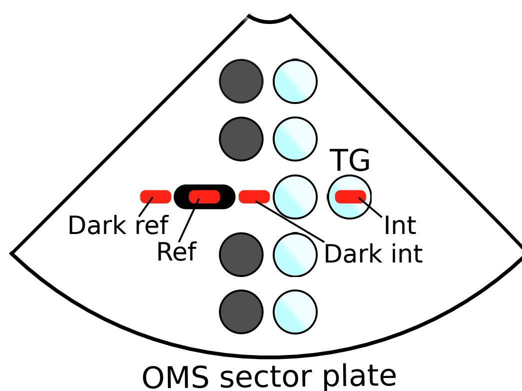

Figure 15. A diagram showing the four calotte locations on which light intensity is measured in order to determine the coating transmittance. 'Dark' background signals are measured against the calotte when $T = 0$ %, 'Ref' is measured with $T = 100$ % and 'Int' is measured through the coated monitoring glass.

4.2.3 Sample analysis

Agilent Cary 7000 spectrophotometer was used for measuring the transmittance spectra of the finished samples. There was also Cary Universal Measurement Accessory (UMA) available for the spectrophotometry. It allowed for reflectance measurements as well as transmittance measurements with oblique angles of incidence, which both proved useful for refractive index characterization of layer materials and substrates.

5 Design process and results

5.1 Bragg mirror

Bragg mirror, also known as a dielectric mirror or a Bragg reflector, is a multilayer dielectric stack of QWOT layers of alternating high and low refractive index materials. It has high reflectance near the central wavelength, the magnitude of which is proportional to the number of layers. Bragg mirrors perform the best when their odd-numbered layers, and consequently the outermost layers, are of material with high n-value [7].

5.1.1 The first design

The structural design for the Bragg mirror was provided by Technical Research Centre of Finland (VTT), and is used here with permission. The mirror was fabricated for ESA-ALTIUS project. The mirror was an 11 layer structure with alternating high refractive index (H) and low index (L) layers. Odd-numbered layers were high index (HfO_2) and even-numbered layers were low index material (SiO_2). The central wavelength for the mirror was $\lambda_0 = 346$ nm. As all the layers were QWOT layers, their optical thicknesses were 86.5 nm. The complete coating structure is shown in table A1 in the Appendix. The structure can be described as following:

$$\mathrm{BK7|H(LH)^5|Air}$$

where H and L are high index and low index QWOT layers respectively. HfO_2 is a suitable high index material for coatings with operating range near UV-region, since HfO_2 has low absorptivity near UV wavelengths. Optical glass BK7 was used as the substrate glass.

For a structure consisting entirely of QWOT layers the immediate idea would be to use a monitoring wavelength equal to λ_0. However, a Bragg mirror has a high reflectance region near λ_0, which may turn transmittance monitoring difficult. Furthermore, using monitoring wavelengths near UV region may be challenging because of the limited light source spectrum as well as the absorptivity of the

substrate. A halogen lamp produces light in the visible and infrared regions, but very little in the UV region. Too short monitoring wavelength may fall out of the operating range of the halogen lamp, which would naturally prevent the transmittance monitoring. For UV-region monitoring a deuterium lamp would be ideal as a light source. Another problem with the UV-region monitoring is that the used substrates absorb UV light. A soft lower limit for the monitoring wavelength was recommended to be about 350 nm by the machine manufacturer.

For these reasons the central wavelength (346 nm) was not used initially. Instead a longer monitoring wavelength was looked for using OptiLayer's *monitoring report* tool. Because the monitoring wavelength had to be $> \lambda_0$ every layer would have phase thickness $< \pi$. Therefore at least the first layer could not contain a signal turning point. $\lambda_m = 420$ nm was found to be a decent monitoring wavelength. The monitoring report can be seen in figure 16. This monitoring wavelength was chosen because all the layers besides the first one contained a turning point, and the later layers contained layer trigger points soon after turning points. The first layer would have to be monitored using OFFSET-algorithm due to the absence of turning points, and the second layer might be slightly safer to monitor with OFFSET-algorithm as well. For the rest of the layers BACKWARDS-algorithm could be used. Simulation results were satisfactory as well (shown in figure A1 in the Appendix), so 420 nm was chosen as the monitoring wavelength.

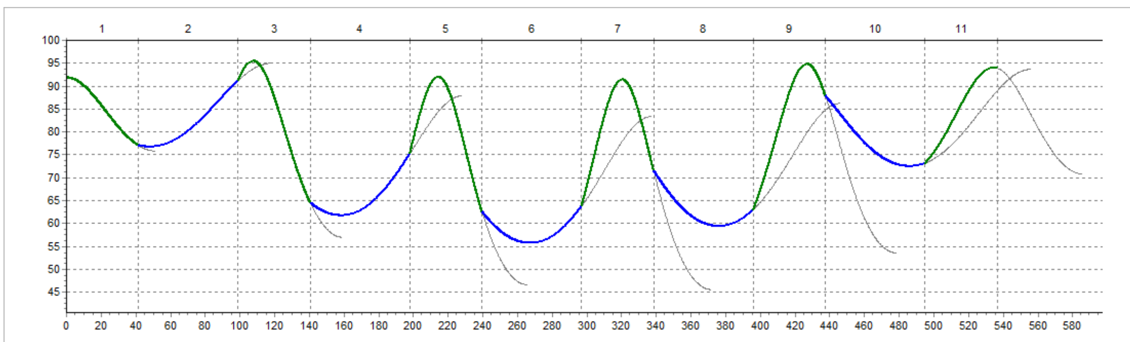

Figure 16. Monitoring report for Bragg mirror ($\lambda_0 = 346$ nm) when $\lambda_m = 420$ nm, exported from OptiLayer. Predicted transmittance signal of the system is presented as the deposition proceeds. The green curves represent the high refractive index layers, and blue curves represent the low refractive index layers. The grey curves act as a visual aid by showing the projected transmittance of a layer up to its next turning point, if that layer was not terminated.

The other deposition parameters did not seem to matter for the results of the simulation. Slit sizes 0.5 mm and 1.0 mm both yielded equally promising predictions, as well as both GSA values 3 and 5. Actual deposition rates were 0.4 nm/s for SiO_2 and 0.1 nm/s for HfO_2. During actual deposition a slit size of 0.5 mm and GSA of 5 were used.

After fabrication the transmittance spectra of the finished samples were measured. They can be seen in figure 17a.

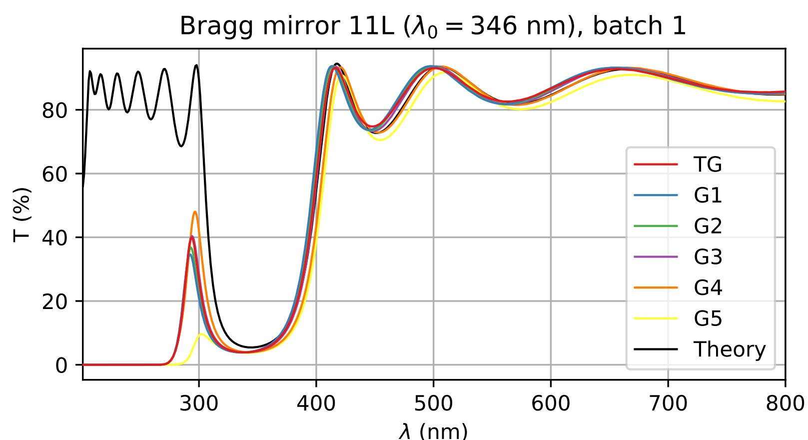

(a) Substrate absorptance not included in the theory.

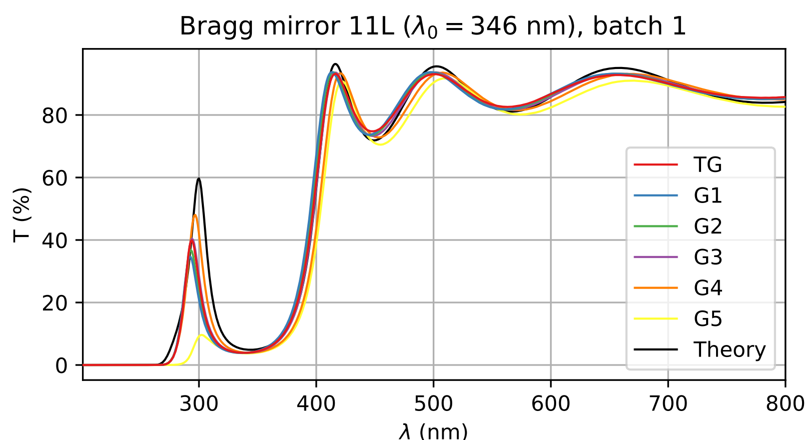

(b) Substrate absorptance included in the theory.

Figure 17. Transmittance profiles of the first batch of Bragg mirrors, with $\lambda_m = 420$ nm. 'TG' (red) is the monitoring test glass. The other glasses are numbered from the apex of the calotte ('G1') towards the edge ('G5'). The theoretical profile (black) is presented for comparison.

The first thing apparent from the transmittance measurement is that the trans-

mittances of the samples drop rapidly to zero for wavelengths under 300 nm. This is likely caused by the substrate, which has considerable absorptivity in the UV region. It was verified by measuring the transmittance profiles for uncoated test glasses, which are shown in the figure 18. The complex refractive indices were determined for the substrates from their transmittance data and included in the theoretical model of the Bragg mirror. In figure 17b the transmittance profiles of the samples are presented alongside the transmittance of the model that includes the newly determined.

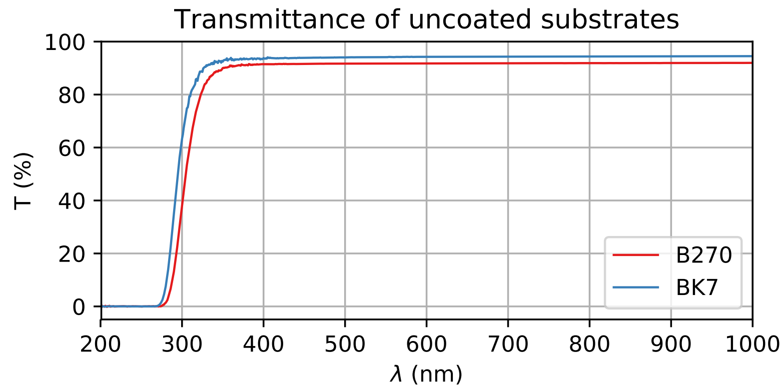

Figure 18. Measured transmittance of uncoated B270 and BK7 substrates. Absorptance is present in the UV-region.

There is an issue with the distribution of the samples, as the location of their first transmittance maximum after the reflecting region varies by almost 10 nm between the samples. This implies that the deposition distribution was not quite optimized. Regarding the performance of the coatings, the rejection region turned out wider and deeper than predicted. Theoretically $\lambda(T_{min}) = \lambda_0 = 346$ nm, but all the samples have a $\lambda(T_{min})$ in the region [337 nm, 341 nm]. If the tolerance for the $\lambda(T_{min})$ is ± 5 nm, only two of the outermost glasses 'G4' and 'G5' would pass. However, the samples do have a better rejection performance at $\lambda(T_{min})$ than the theoretical model predicted. Combined with increased rejection bandwidth, the performance of the coating is better than predicted if the shifted $\lambda(T_{min})$ is not an issue.

The monitoring strategy was suspected to be a reason for the shifted $\lambda(T_{min})$. While the simulations yielded excellent predictions, the strategy may not have translated perfectly into the actual experiment. The OFFSET-algorithm that was used for monitoring the first two layers may have to be changed. The OFFSET-algorithm uses the initial offset between the measured transmittance and the theoretical trans-

mittance at the beginning of the layer to adjust the trigger point level. This only works accurately if the theoretical layer refractive index matches the actual deposited refractive index. The wide rejection region seen in the finished samples indicates that the deposited layers had greater $n_{\mathrm{H}}/n_{\mathrm{L}}$ ratio than in theory (based on equation 27). Therefore it is possible that the n of HfO_2 was higher when deposited, which would cause the early OFFSET-terminated layers to have incorrect layer thicknesses. The later layers can compensate the early thickness errors, but it would still be worth to try another monitoring strategy.

5.1.2 The second design

The only parameters that affect the monitoring significantly are the monitoring wavelength, the monitoring algorithm and the monitoring method. Since the first layer of the Bragg mirror can not contain a turning point when $\lambda_m > 346$ nm, only the OFFSET-termination algorithm can be used for longer monitoring wavelengths. Monitoring the first two layers with QCM instead of OMS is a possibility, but it would be ideal if the entire coating was monitored optically. Instead the monitoring wavelength was changed to $\lambda_m = \lambda_0 = 346$ nm. As was earlier discussed, one should generally avoid monitoring wavelengths near the UV region due to absorption. Additionally the mirror has a high reflectance zone at λ_0, but there is a considerable justification to use $\lambda_m = \lambda_0$ anyway. Using this monitoring wavelength every layer will have optical thickness equal to $\lambda_0/4$, and therefore layers can be terminated at the signal turning points. Thus every layer will have a clearly defined termination condition that is not dependent on the deposited material's refractive index. Also the reflecting region will not be a problem in this case, as can be seen by looking at the monitoring report in figure 19. The reflectance of the system will gradually increase, but the layer count is sufficiently small to allow transmittance monitoring. The total reflectance for a structure like this increases as a function of the layer count (equation 26 and figure 2). Therefore the early layers will have only small or moderate reflection. Thus the second monitoring strategy will use $\lambda_m = \lambda_0 = 346$ nm.

The simulation results for the new monitoring strategy can be seen in figure A2 in the Appendix. The simulated depositions yielded excellent results. There were consistent layer thickness errors, but they were self-compensated for, and the end results did not suffer. This monitoring strategy should yield more consistent results over a number of deposition processes compared to the previous strategy.

The deposition parameters are the same as in the first batch (0.5 mm slit, GSA 5), besides the new monitoring wavelength and that BACKWARDS-termination algorithm was used for all layers. Of course, it was pre-emptively verified that 346 nm is a practical monitoring wavelength for our equipment. This was checked in SyrusPro's preparation mode by running a test transmittance measurement using an uncoated substrate. The signal strength was good and the standard deviation of the signal stayed in an acceptable level, under 0.01 %.

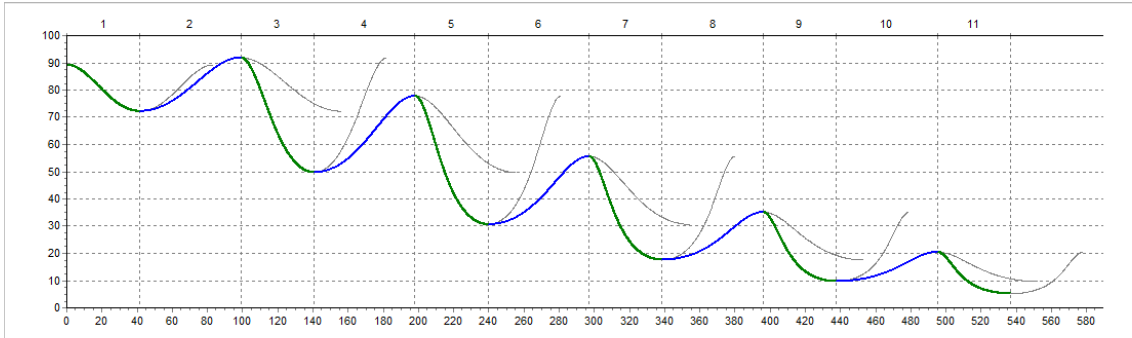

Figure 19. Monitoring report for Bragg mirror ($\lambda_0 = 346$ nm) when ($\lambda_m = \lambda_0$), exported from OptiLayer. The green curves represent the high refractive index layers, and the blue curves represent the low refractive index layers. The grey curves act as a visual aid by showing the projected transmittance of a layer up to its second turning point, if that layer was not terminated.

The deposition process was performed again with the new monitoring strategy. Due to a temporary shortage of substrates, only four sample substrates and the monitoring glass were loaded into the machine. The outermost glass, 'G5', was omitted because in the previous experience it had the most problems with the deposition distribution. After deposition, the transmittance profiles of the samples were measured, and they can be seen in figure 20

Comparing the new batch (figure 20) to the first batch (figure 17) it seems that the effects of changing the monitoring strategy were subtle. The new batch has its transmittance profile shifted towards the longer wavelength by about 6 - 8 nm. Every sample coating of the new batch has $\lambda(T_{min})$ within a tolerance value of ± 5 nm from the theoretical $\lambda(T_{min}) = 346$ nm, whereas in the first batch only two coatings passed. The rejection bandwidth is the same between the two sample batches, as is to be expected. The rejection bandwidth is dependent on the $n_{\mathrm{H}}/n_{\mathrm{L}}$-ratio, which has stayed unchanged between the fabrication processes, since deposition parameters

were not altered. As the rejection band shape and depth are the same between the batches the film quality is equally good between them. Changing the monitoring wavelength shifted the spectral profile slightly along λ-axis, but did not affect the film quality. The spectral performance was also similar between the batches.

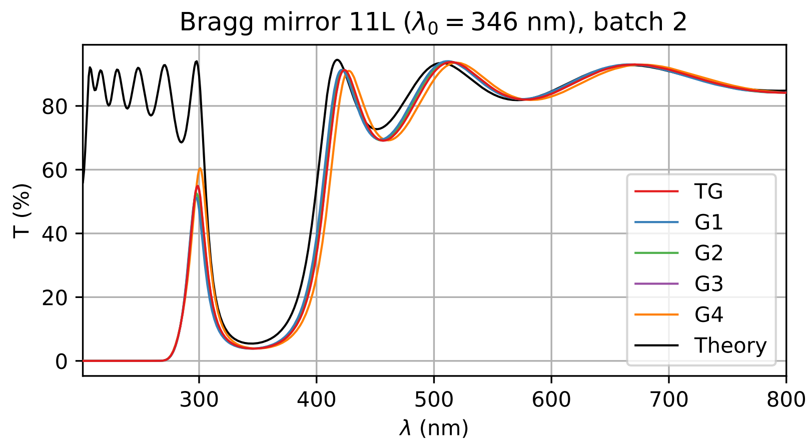

(a) Substrate absorptance not included in the theory.

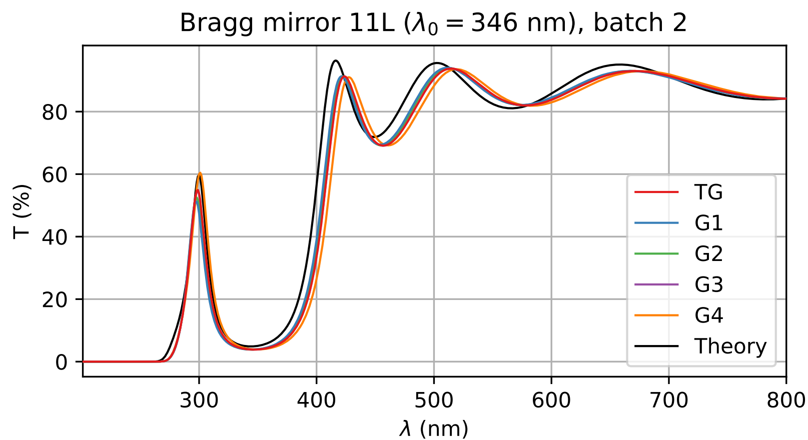

(b) Substrate absorptance included in the theory.

Figure 20. Transmittance profiles of the second batch of Bragg mirrors, with $\lambda_m = 346$ nm. 'TG' (red) is the monitoring test glass. The other glasses are numbered from the apex of the calotte ('G1') towards the edge ('G4'). The theoretical profile (black) is presented for comparison.

5.2 Short pass edge filter

A short wavelength pass edge filter (from here on called "short pass edge filter" or "SPF") has an operating region divided into a passing region (high transmissivity) and a blocking or rejection region (very low transmissivity). These regions are separated by an edge region, where the transmissivity rapidly declines from high T to low T. A cut-off wavelength (λ_c) is the point in the edge region where $T = 50\%$. The steepness of an edge filter can be described by a slope factor, which unfortunately has slightly differing definitions in the industry. For our purposes it is sufficient to define the slope factor as follows:

$$\text{slope factor} = \frac{|\lambda(T = 80\%) - \lambda(T = 10\%)|}{\lambda_{\text{Cut-off}}} \tag{35}$$

The SPF was designed with specifications listed in table 1 as the goal. $T \geq 91$ % was desirable over the passing region. In the blocking region the optical density of the filter should be ≥ 4.0, which means $T \leq 0.01$ %. The equipment manufacturer, Bühler, provided support in the structure design as well as proposed the monitoring strategy. SiO_2 and TiO_2 were chosen for layer materials as they have the highest n_H/n_L contrast of our available materials.

Table 1. Optical specifications for a short pass edge filter. The angle of incidence is 0 °.

SPF 625	
Cut-off wavelength (nm)	625
Cut-off tolerance (%)	±1
Slope factor (%)	< 1
Passing region (nm)	$350 - 612$
Transmittance (%)	≥ 91
Blocking region (nm)	$639 - 900$
Optical density	≥ 4.0

5.2.1 The first design

The blocking region can be built using a multilayer QWOT stack which has its central wavelength at the middle of the blocking region. However, a simple QWOT stack will not be able to meet the strict specifications set for the filter. First, the blocking region is too wide for a single QWOT stack to cover. Multiple QWOT stacks with different central wavelengths should be used to widen the blocking region. The central wavelengths for the stacks can be chosen in such a way that the reflecting regions of the stacks overlap slightly with each other. By linking multiple stacks in such a manner even very wide blocking regions can be acquired, though the overall structure will become very complicated as a result. The stacks can be deposited on top of each other or on different sides of the substrate. In this case the desired blocking region can be achieved by using two QWOT stacks, and they will be deposited on top of each other.

Second, the structure needs to be refined. A simple QWOT stack with uniform layer thicknesses contains ripples outside of its reflecting region. These ripples, or oscillations of transmissivity, have to be eliminated. By refining layer thicknesses these ripples can be suppressed and the edge region can be steepened. Computational software, such as OptiLayer, can and is recommended to be used for layer refinement. Figure 21a shows the transmissivity profiles of the two separate QWOT stacks after refinement. The transmissivity profile of the entire structure can also be seen in figure 21b. The structure can be described by notation

$$\mathrm{BK7|L(HL)^{38}|Air}$$

where L is SiO_2 and H is TiO_2. The optical thicknesses of the layers are not equal. The complete structure with exact layer thicknesses is shown in table A2 in the Appendix.

For the monitoring strategy Bühler proposed two options. The filter should be fabricated using either two or four monitoring glasses. As the structure of the coating is based on two QWOT stacks of different central wavelengths, it makes sense to monitor them using separate monitoring glasses. The monitoring reports can be seen in figures 22 and 25 respectively. The first SiO_2 layer will be monitored using QCM due to SiO_2's poor contrast with a glass substrate. The last three layers will also utilize QCM because two of them are too thin to monitor reliably optically (see layers 75-77 in figure 22 or 25). Both two and four glass monitoring strategies show

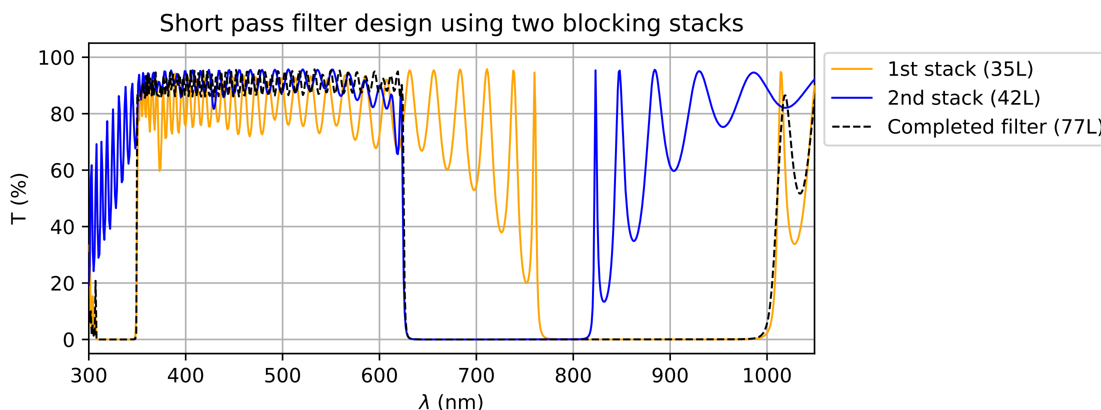

(a) Theoretical transmissivity profile demonstrating the SPF design utilizing two multilayer blocking stacks. Separately the stacks have limited blocking bandwidths. When the two stacks are deposited on top of each other the resulting 77 layer coating achieves both a wide blocking region and a highly transmissive passing region.

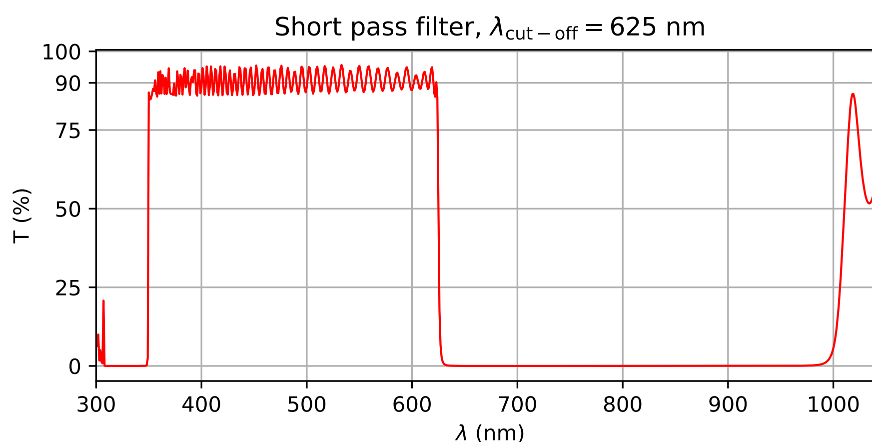

(b) Theoretical transmissivity profile of the completed filter.

Figure 21. Theoretical transmissivity profile of the SPF625 filter with 77 layer design. The structure can be described by BK7|L(HL)^{38}|Air, where L is SiO_2 and H is TiO_2. The optical thicknesses of the layers are not equal. **(a)** demonstrates the dual stack design principle used to achieve a wide blocking region. **(b)** shows the theoretical transmissivity of the completed filter.

promising results in OMSVis simulations (simulated transmittance profiles shown in figures A3 and A6 in the Appendix). Simulation results for individual monitoring glasses are listed in the Appendix as well. Simulated transmittance profiles for monitoring glasses used in 2-glass monitoring strategy are shown in A4 and the layer thickness errors in figure A5. Similarly the simulated transmittance profiles for

4-glass monitoring are shown in figure A7 and the layer thickness errors in figure A8. For parameters the simulations used slit size 0.5 mm and GSA value 3. The deposition rate was set to 0.4 nm/s for SiO_2 and 0.25 nm/s for TiO_2 to reflect their actual deposition rates. In 2-glass monitoring the first stack would use $\lambda_m = 765$ nm and the second stack would use $\lambda_m = 628$ nm. The 4-glass monitoring would use $\lambda_m = 765$ nm for monitoring glasses 1 - 2, and $\lambda_m = 628$ nm for glasses 3 - 4.

The disadvantage of using more than one monitoring glass in direct monitoring is that the fabrication process has to be stopped in order to change the monitoring glass. Stopping and restarting the fabrication process is not only time-consuming, but could also disturb the unfinished coatings. In order to change the monitoring glass the deposition chamber has to be vented and opened, which exposes the unfinished coatings to oxidation, moisture and temperature changes. However, in this case using multiple monitoring glasses is still preferable. Finding an optimal monitoring wavelength is easier when the two stacks can be monitored separately. In the case of short pass filters, it is desirable to choose the monitoring wavelength at the lower wavelength edge of the blocking region, since then most of the layers will have optical thickness $> \lambda_m/4$. If two monitoring glasses are used the two stacks can be both monitored using this strategy, without the first stack interfering with the monitoring of the second stack. Furthermore, replacing the monitoring glass in the middle of a long fabrication process may improve the signal quality and accuracy of the monitoring process. Also when the deposition is stopped, there is an opportunity to clean the deposition chamber and some components, such as the APS anode tube that accumulates dirt during operation. The evaporant materials can also be restocked. The quality of the coating could improve and contamination can possibly be avoided this way.

The four glass monitoring does not offer any significant theoretical advantage over two glass monitoring (comparing figures A3 and A6), but it might improve the fabrication process in practice. When the monitoring glass is changed and a new stack is started, any previous error layer thicknesses are effectively forgotten by the monitoring process. This stops excessive layer error cumulation, although the monitoring process also can no longer self-compensate the errors of the previous monitoring glasses. On top of that, the transmittance signal strength will increase when changing the monitoring glass to an uncoated one. As can be seen in figure 22, the monitored transmittance signal will oscillate at very low intensity levels during

the later layers of each monitoring glass. The ratio of background noise to signal intensity is the highest when the coating transparency is low. Now comparing the monitoring report to that of the 4TG monitoring (figure 25) it can be seen that the 4TG monitoring allows for more layers to be monitored at higher transmittance levels. Thus the signal-to-noise ratio should generally be better when using four monitoring glasses. The layer termination points are also easier for OMS to determine from higher signal oscillation amplitudes than from small amplitudes. Changing the monitoring glass more often, however, exposes the unfinished coatings to atmospheric conditions more often. The samples will also undergo more cycles of heating and cooling, which could introduce film stress due to thermal expansion.

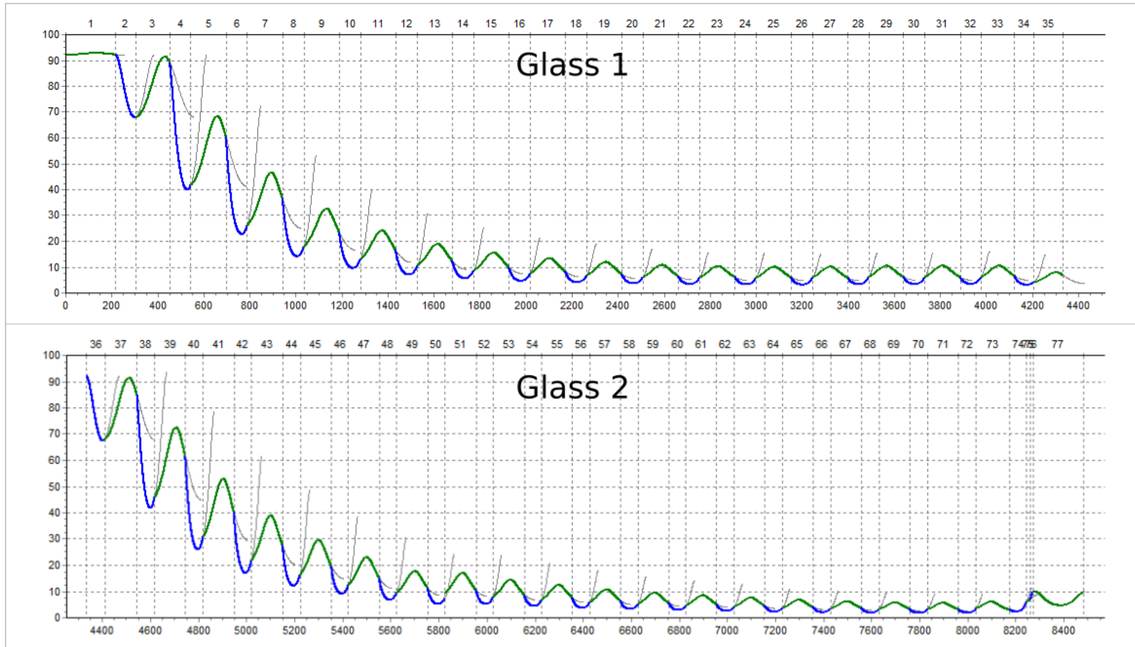

Figure 22. Two glass monitoring report for SPF625 77L design, exported from OptiLayer. The graphs present the monitored transmittance signal during the course of the deposition process. The first glass uses $\lambda_m = 765$ nm and the second glass uses $\lambda_m = 628$ nm. Green curves represent the low refractive index layers, and blue curves represent the high refractive index layers. The grey curves act as a visual aid showing the transmittance curve up to the next turning point of the layer, if the layer was not terminated.

Transmittance profiles were measured for the completed filters with spectrophotometer. The measured profiles can be seen in figure 23. Focused plots of the measured data around the passing region, blocking region and edge region are shown

in figure 24. One of the test coatings, 'G4' was not completed for reasons unrelated to the deposition process. Data analysis on the most important transmittance characteristics is presented in table 2. The desired specifications were listed in table 1. The exact wavelengths were determined by linear interpolation of the measurement data.

The cut-off point $\lambda(T = 50\%)$ of the filter edge was supposed to be located at $\lambda = 625$ nm with a tolerance of ± 1 % or ± 6.25 nm. The cut-off points placed within 0.6 % margin, thus achieving the tolerance requirement for the cut-off wavelength location. Of the test glasses 'G3' had the cut-off point closest to the goal, which could be expected since 'G3' is located at the same height on the calotte as the monitoring glass 'TG'. The glass at the top of the calotte, 'G1', and the outermost glass, 'G5', had the cut-off points furthest from the target. The coatings have experienced slightly different deposition distributions. This was addressed in the future depositions by altering the shape of the mask which shadows a section of the calotte.

The slope factor was determined from $\lambda(T = 80\ \%)$ and $\lambda(T = 10\ \%)$ points of the edge using equation 35. The goal was to reach slope factor < 1 %. Coatings 'G1' - 'G3' reached the specification. However 'G5' had slope factor 1.9 %. Figure 24 shows that the high transmission side of the 'G5' edge has degraded causing the first oscillation maximum of the passing region to fall under $T = 80$ %, giving the coating poor slope factor.

The passing regions of the coatings were not as good as desired. The aim was to have $T \geq 91$ % in the $350 - 612$ nm region. The transmittance stayed mostly $80\ \% - 90\ \%$ at $400 - 612$ nm, with the exception of a sharp and narrow transmittance drop near 460 nm in coatings 'G1' - 'G3'. Reverse engineering analysis with OptiRE was used to trace down the cause for the drop. The coating seems to be sensitive to altering layer thickness errors, which could cause the tear to appear in the passing region. Bulk inhomogeneities could also be a cause. Transmittance dropped rapidly under 400 nm in every sample. This may be caused by the increasing absorption in the substrate (BK7) and TiO_2 near the UV-region, which were not accounted for in the theoretical model. The $SiO_2 - TiO_2$ interface could also induce absorption. The transmittance drop at $\lambda < 400$ nm degraded the average transmittance within the given passing region.

The blocking region was designed to have optical density higher than 4, so

transmittance should be < 0.01 % in region 639 nm − 900 nm. The shorter wavelength side of the blocking region was not entirely within the specifications. The coatings reached OD 4 at 641 nm – 651 nm, with 'G1' having $\lambda(\mathrm{OD} = 4)$ the closest to the specified target. However, the average transmittances in the blocking regions were almost one order of magnitude better than desired. Producing coatings with OD > 5 should be possible if ripples can be entirely eliminated.

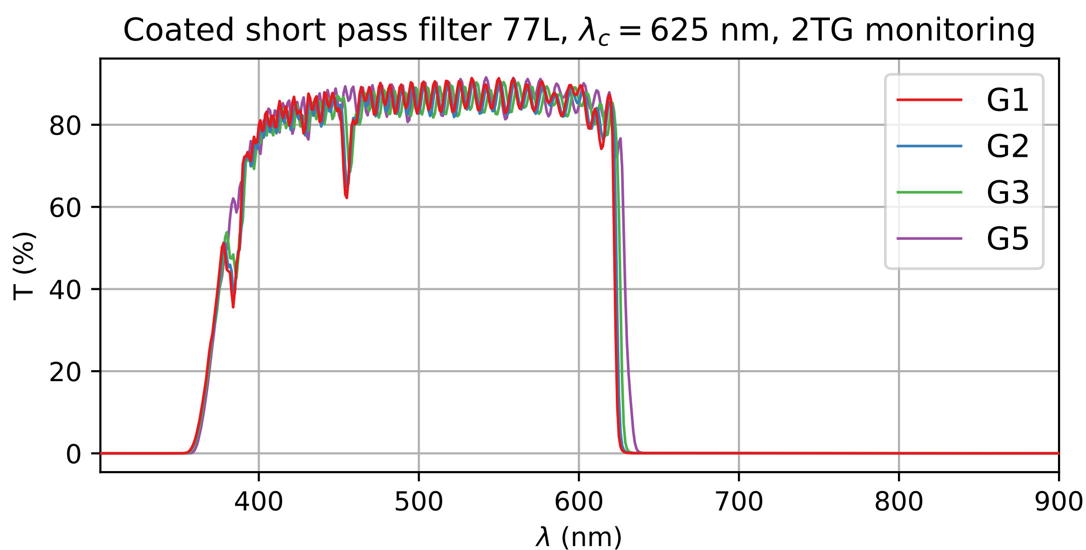

Figure 23. Transmittance profiles for the first batch of fabricated SPF625 filters using the 2-glass monitoring. The glass numbering begins from the apex of the calotte ('G1') towards the edge ('G5'), though glass G4 is absent.

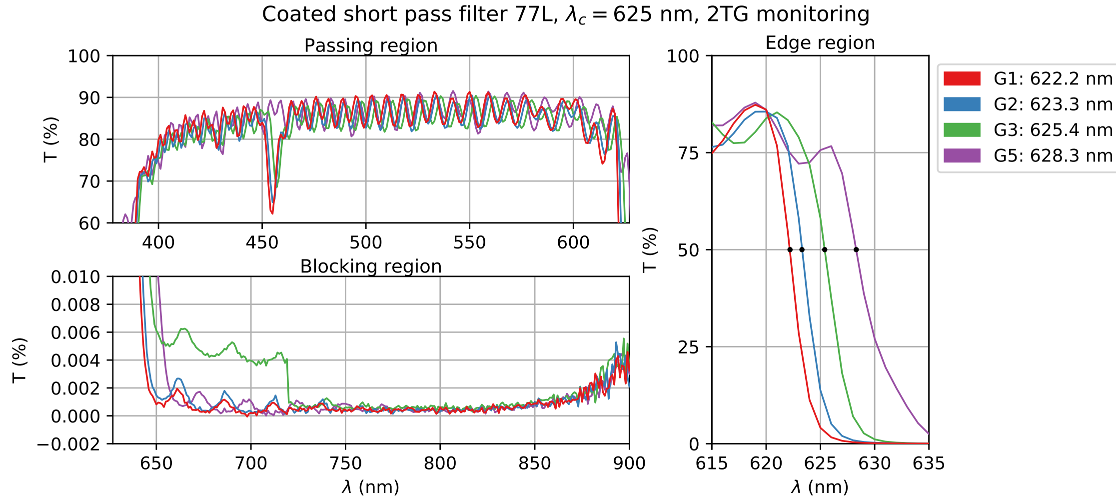

Figure 24. Transmittance profiles in the areas of interest for the deposited SPF625 filters using the 2-glass monitoring. The glass numbering begins from the apex of the calotte ('G1') towards the edge ('G5'), glass G4 is absent. The sudden increase in the transmittance of 'G3' in the blocking region is very likely a measurement error.

Table 2. Results for the fabricated short pass filter samples. The coating was produced in two fabrication processes using two monitoring glasses. The desired specifications can be seen in table 1. Glass numbering begins from the apex of the calotte ('G1') towards the outermost row ('G5'). The fourth test glass, 'G4', is not presented due to a fault unrelated to the depositon process. The blocking region spanned 350 nm - 612 nm, and the passing region spanned 639 nm - 900 nm.

	G1	**G2**	**G3**	**G5**
$\lambda(T = 50\ \%)$ (nm)	622.2	623.3	625.4	628.3
$\lambda(T = 10\ \%)$ (nm)	624.2	625.4	627.7	632.9
$\lambda(T = 80\ \%)$ (nm)	620.7	621.5	622.8	621.2
Slope factor (%)	0.6	0.6	0.8	1.9
T_{avg} (%), passing	75.5	74.8	74.7	76.2
T_{max} (%), blocking	0.0187	0.026	0.0327	0.138
T_{avg} (%), blocking	0.001	0.0013	0.0028	0.0026
$\lambda(T = 0.01\ \%)$ (nm)	641.2	642.8	646.6	650.9

5.2.2 The second design

The short pass filter was also fabricated using four monitoring glasses in order to compare whether two or four glass monitoring was better. The structure of the coating is exactly the same as in two glass monitoring. Only the fabrication and monitoring processes have been changed. The deposition process has been divided into four separate processes, in-between which the monitoring glass is changed to a new one.

After two glass monitoring the deposition chamber mask shape was adjusted slightly in order to improve deposition distribution. According to tests the three upper rows on calotte ('G1' - 'G3') should have better deposition distribution than before. The 'G4' and 'G5' glasses could not be significantly improved with these adjustments.

The measured transmittance spectra for the completed coatings can be seen in figure 26. In figure 27 the passing region, blocking region and edge region are shown more clearly. Data analysis on the most important transmittance characteristics is shown in table 3.

Table 3. Results for fabricated short pass filter samples. The coating was produced in four fabrication processes using four monitoring glasses. The desired specifications can be seen in table 1. Glass numbering begins from the apex of the calotte ('G1') towards the outermost row ('G5'). The blocking region spanned 350 nm - 612 nm, and the passing region spanned 639 nm - 900 nm.

	G1	**G2**	**G3**	**G4**	**G5**
$\lambda(T = 50$ %) (nm)	623.0	624.7	625.2	632.1	630.9
$\lambda(T = 10$ %) (nm)	627.0	627.6	627.8	634.5	632.8
$\lambda(T = 80$ %) (nm)	609.6	622.4	621.5	627.5	626.8
Slope factor (%)	2.8	0.8	1.0	1.1	1.0
T_{avg} (%), passing	74.4	78.1	75.3	76.2	77.1
T_{max} (%), blocking	0.0208	0.0164	0.0374	0.2744	0.1385
T_{avg} (%), blocking	0.0017	0.0008	0.0017	0.0044	0.0027
$\lambda(T = 0.01$ %) (nm)	648.7	642.5	646.4	651.8	648.7

The cut-off point location of the filter was specified to be at $\lambda_{\text{cut-off}} = 625$ nm with a tolerance of ±1 % or ±6.25 nm. Samples 'G1' - 'G3' and 'G5' had their cut-off

points located within the given tolerance, with 'G2' and 'G3' settling within ± 0.3 nm margin from the goal. The glass 'G4' deviated by 1.2 % from the specified cut-off point, thus not fulfilling the specification. Adjustment of the mask should have fixed the deposition distribution over the calotte, causing the transmittance profiles to shift closer to each other. However, when comparing the determined cut-off wavelengths $\lambda(T = 50\ \%)$, and their deviation from the expected $\lambda(T = 50\ \%) = 625$ nm, between the two filter batches, the differences were subtle. Cut-off wavelengths of the coatings 'G1' to 'G3' matched the theory slightly better after adjusting the mask, but the coating 'G5' shifted even further away from the target of 625 nm. Further adjustments to the mask are probably necessary in order to correct the deposition deviation.

The slope factors were determined from $\lambda(T = 10\ \%)$ and $\lambda(T = 80\ \%)$ points at the filter edge region using equation 35. The desired slope factor was < 1 %. The steepness performance of this filter batch was somewhat underwhelming, with only one test coating ('G2') achieving the desired slope factor. The slope factors for coatings 'G3' and 'G5' were 1.0 % and for 'G4' 1.1 %, which could be called passable, though not excellent. The coating 'G1' had a slope factor of 2.8 %, which was caused by poor transmittance profile shape on the shorter wavelength side of the edge region (see figure 27).

The passing region turned out similar to the filters fabricated using two monitoring glasses. The transmittance oscillated mostly between $80\ \% - 90\ \%$ when $\lambda > 400$ nm, but dropped rapidly when $\lambda < 400$ nm. There was again a sudden and narrow drop in transmittance at $\lambda \approx 460$ nm which, similarly to 2TG filters, was not present in the 'G5' sample. These drops degraded the average transmittance over the passing region. The average transmittance value between 2TG and 4TG filters was roughly equal.

The blocking region also turned out similar to the 2TG samples. The average transmittances over the blocking region were close to the average transmittances of the 2TG samples. Every sample reached the desired average optical density. As was the case with the 2TG coatings, the 4TG filters reached OD 4 on wavelengths longer than specified. Therefore the shorter wavelength side of the blocking region had OD > 4 in every filter sample.

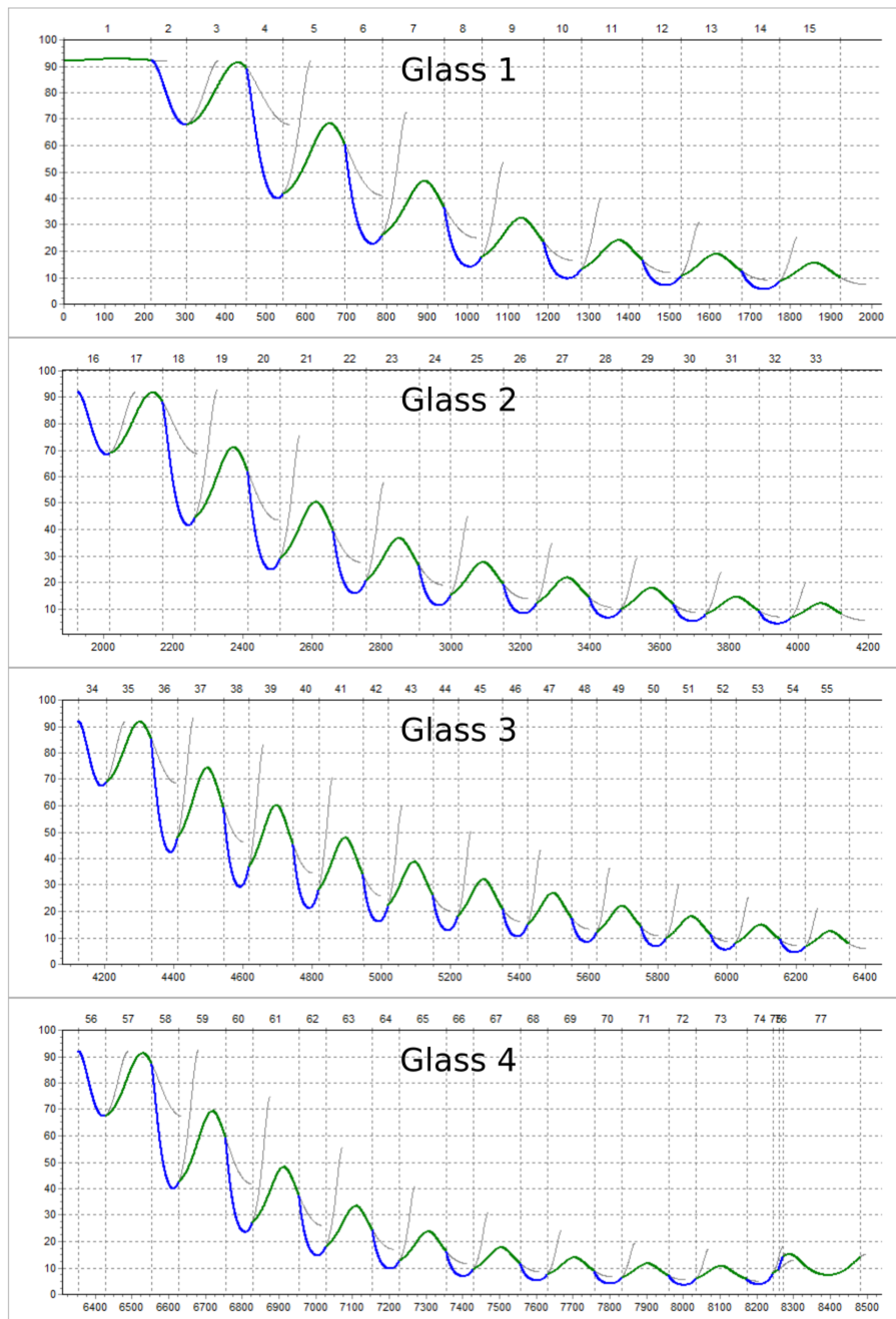

Figure 25. Four glass monitoring report for SPF625 77L design, exported from OptiLayer. The graphs present the monitored transmittance signal during the course of the deposition process. The 4-glass monitoring used $\lambda_m = 765$ nm for monitoring glasses 1 - 2, and $\lambda_m = 628$ nm for glasses 3 - 4. Green curves represent the low refractive index layers, and blue curves represent the high refractive index layers. The grey curves show a virtual transmittance curve up to the next turning point of the layer

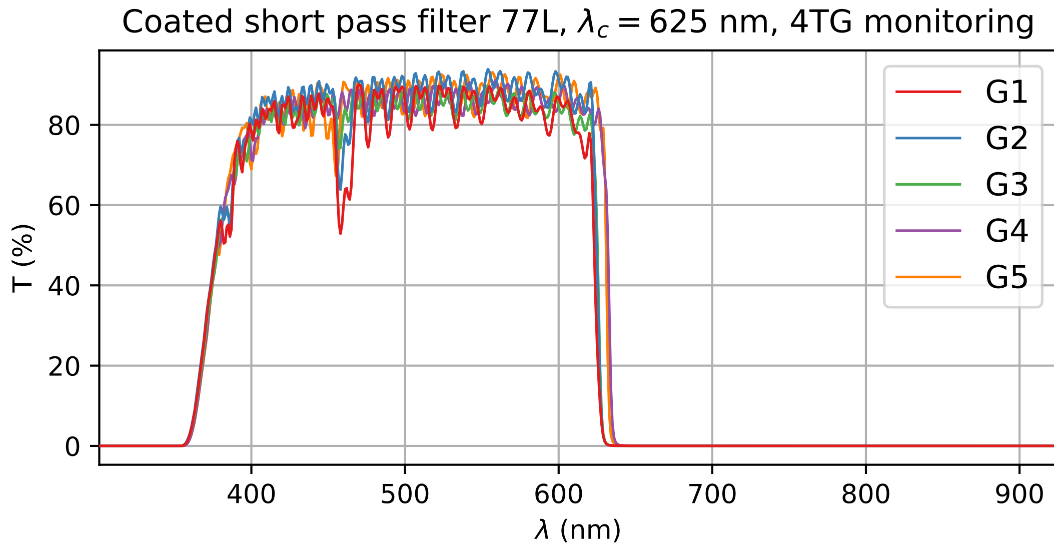

Figure 26. Transmittance profiles for the second batch of deposited SPF625 filters that used 4-glass monitoring. The glass numbering proceeds from the apex of the calotte ('G1') towards the edge ('G5').

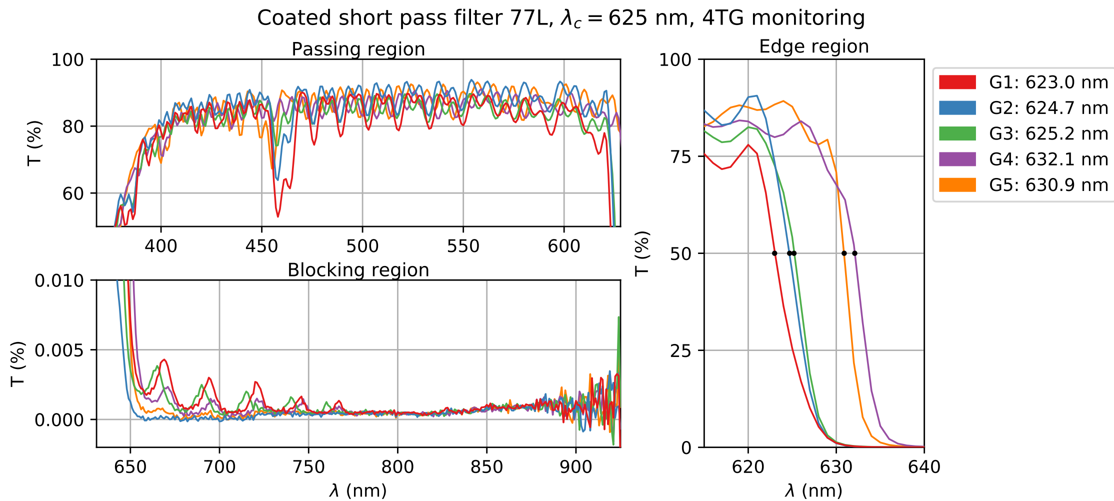

Figure 27. Transmittance profiles in the areas of interest for the deposited SPF625 filters using 4-glass monitoring. The glasses are numbered from the apex of the calotte ('G1') towards the edge ('G5').

5.3 Long pass edge filter

A long wavelength pass edge filter (from here on called "long pass edge filter" or "LPF") is an edge filter that transmits light of longer wavelength than its cut-on point and blocks a band of light with shorter wavelength. The passing and blocking regions are separated by an edge region, where the transmissivity rises sharply. The cut-on point is defined as $\lambda_c = \lambda(T = 50\ \%)$. The specifications for the filter are listed in table 4.

Table 4. Optical specifications for a long pass edge filter. The angle of incidence is 0 °.

LPF 425	
Cut-on wavelength (nm)	425
Cut-on tolerance (%)	± 1
Slope factor (%)	< 1
Passing region (nm)	433 – 1650
Transmittance (%)	≥ 91
Blocking region (nm)	200 – 415
Optical density	≥ 4.0

As usual, the design process began with a single QWOT stack. TiO_2 and SiO_2 were chosen as layer materials because of their excellent $n_\mathrm{H}/n_\mathrm{L}$ ratio and availability. Macleod suggests that a design of a long pass edge filter should be based on a $(0.5\mathrm{H}\ \mathrm{L}\ 0.5\mathrm{H})^j$ stack [7, p. 206]. In order to acquire a sufficient optical density and slope steepness it was decided that $j = 18$. When the QWOT stack central wavelength $\lambda_0 = 370$ nm the longer wavelength edge of the blocking region was located near the cut-on wavelength $\lambda_c = 425$ nm. Thus the starting design can be described by formula $(0.5\mathrm{H}\ \mathrm{L}\ 0.5\mathrm{H})^{18}$ with $\lambda_0 = 370$ nm. The theoretical transmittance profile for this stack can be seen in figure 28.

The blocking region should extend all the way down to 200 nm. At this point, according to the design software, the blocking region does not seem to extend far enough into UV region. The width of a QWOT stack's reflecting region is proportional to the central wavelength λ_0, which means that in the UV region the blocking bandwidths become relatively narrow. Thus possibly two additional stacks might be necessary, which would make the structure much more complicated. Also,

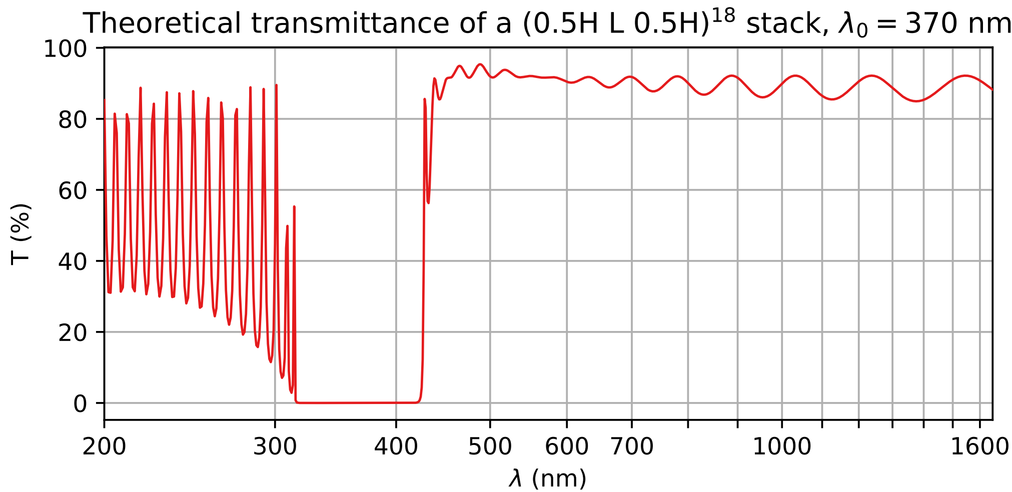

Figure 28. Theoretical transmittance profile for B270|(0.5H L 0.5H)^{18}|Air stack with $\lambda_0 = 370$ nm, computed by OptiLayer. H are TiO_2 layers and L are SiO_2 layers with optical thickness $\lambda_0/4$. The total layer count is 37.

as discussed in the experimental methods section 4 and Bragg mirror section 5.1, our optical monitoring equipment is not able to monitor in the UV region. However, there can be a considerably easier way to extend the blocking region far into UV. The B270 glass substrate used in the computational analysis did not have assigned k-value and therefore did not exhibit any absorptivity. Common glasses in reality have strong absorptivity in the UV region, as was already demonstrated in the analysis of Bragg mirrors. The B270 test glasses were examined with spectrophotometry. The results showed a rapid drop in transmittance when $\lambda < 350$ nm, and reaching $T < 0.1$ % when $\lambda < 275$ nm. Transmittance of an uncoated B270 substrate was plotted in figure 18. The substrate absorptivity should enhance the blocking region in the LPF, and even eliminate any need to extend the blocking region by adding layers.

Next the LPF design had to be refined. This was performed computationally using design tools available in OptiLayer. Refining in itself was a simple task, as the software is able to do it independently and quite accurately from a sufficient starting design. However, careless refinement can introduce layers with inconvenient thicknesses into the design. Very thin layers, especially in the middle layers, can make optical monitoring challenging, and those layers may become highly vulnerable to thickness errors [22, p. 82]. Sometimes this is not an issue, as every layer is not

equally sensitive to errors (error sensitivity can be approximated with tools offered by OptiLayer). However, it is desirable to make the design as robust as possible, and therefore thin middle layers should be avoided. It is better to minimize the thickness deviation between the layers if possible, which will also help in creating the monitoring strategy. Referring back to the theoretical transmissivity profile of the QWOT stack (figure 28), it can be seen the profile is already quite close to the desired outcome. *Constrained optimization* -tool was used to optimize the structure while restricting how much the layer thicknesses were allowed to be modified. For layers 1 – 33 about 5 % thickness deviation was allowed. Layers 34 – 36 were given a thickness limit between 0 nm and 300 nm. The resulting structure seemed satisfactory by its spectral performance. The final design came out to be a 36 layer structure described by

$$\text{B270}|(\text{H L})^{18}|\text{Air}$$

where H is TiO_2 and L is SiO_2. The layer thicknesses are not equal. The exact structure is listed in the Appendix table A4. Transmittance profile for the refined design can be seen in figure 29.

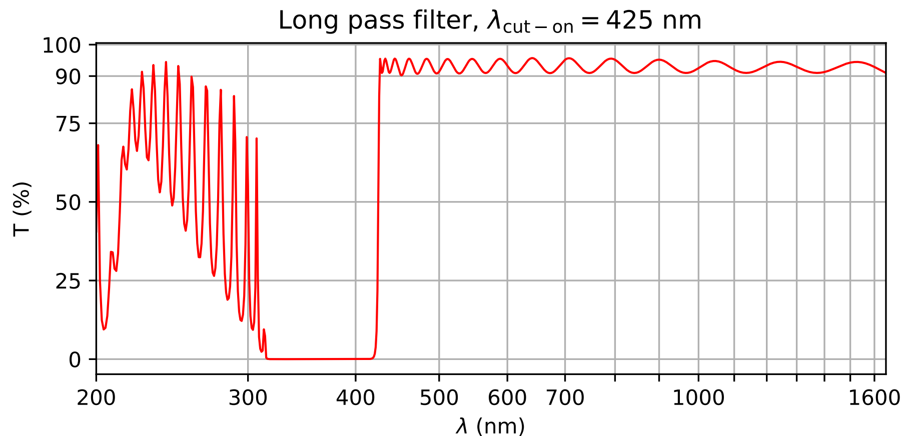

Figure 29. Theoretical transmissivity profile for the refined 36 layer LPF design. The structure can be described by formula B270$|(\text{HL})^{18}|$Air, but the layer thicknesses are not equal. For the exact design structure, refer to table A4 in the Appendix. Absorptivity of the substrate is not accounted for in the theory.

With long pass filters it is usually the best to choose a monitoring wavelength in the transmitting region just after the edge. For this filter $\lambda_m = 430$ nm was chosen

as the monitoring wavelength. The monitoring report for the LPF can be seen in figure 30. As stated earlier, choosing a monitoring strategy usually becomes easier when the layers are of similar optical thickness. With the exception of the first layer, every layer now has at least one turning point. Furthermore, aside from layers 1, 2 and 3, the turning points of the layers are not too close to the layer starting point. In the final layers the trigger points are just after the turning points, which is desirable.

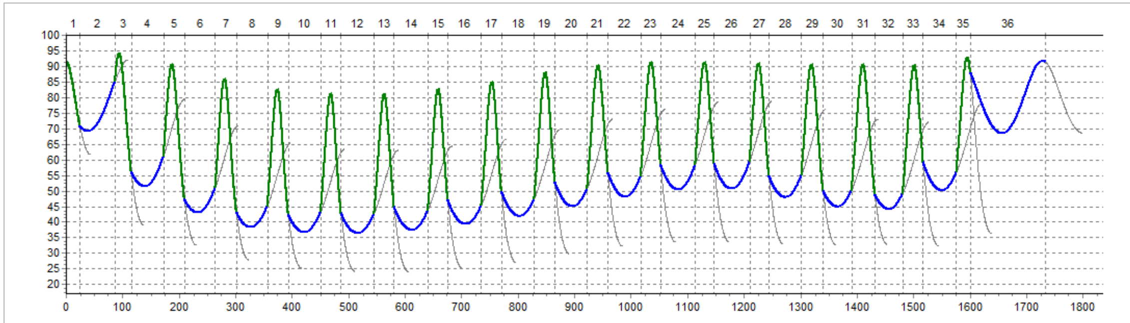

Figure 30. Monitoring report for LPF ($\lambda_c = 425$ nm) design when monitoring wavelength is $\lambda_m = 430$ nm, exported from OptiLayer. The graph presents the monitored transmittance signal during the course of the deposition process. Green curves represent the high refractive index layers, and blue curves represent the low refractive index layers. The grey curves show the transmittance curve up to the next turning point of the layer, if the layer was not terminated. They are there only for a visual aid.

Deposition simulations were run in order to predict whether this monitoring strategy and design were feasible. The monochromator slit size was again set to 0.5 mm. The deposition rates were 0.4 nm/s for SiO_2 and 0.25 nm/s for TiO_2. The first layer was monitored with QCM due to a lack of turning points, although optical monitoring could also be tried with OFFSET-algorithm. The GSA value was not clear whether 3 or 5 would be better, so a simulation was run for each value. The simulation results can be seen in figure A9 in the Appendix. The simulated coatings match the theory phenomenally. The estimated layer thickness values show that the GSA parameter values 3 and 5 caused a slight difference in layer thickness errors, but looking at the transmittance profiles the actual effect seems negligible. Experimental errors have much more relevance to the end result. GSA was decided to be 5. According to simulations this design and monitoring strategy should be robust enough to try out in practice.

The fabricated sample filters were measured with a spectrophotometer. The transmittance profiles can be seen in figure 31. In figure 32 the focused passing, blocking and edge region are displayed. Immediately it can be seen that there is no transmission in the UV region, even though the theoretical model predicted there would be (figure 29). In reality the substrate and the coating itself absorbed the UV region light strongly. Data analysis on transmittance characteristics was performed and the results are displayed in table 5. The exact wavelengths were determined by linear interpolation of the measurement data.

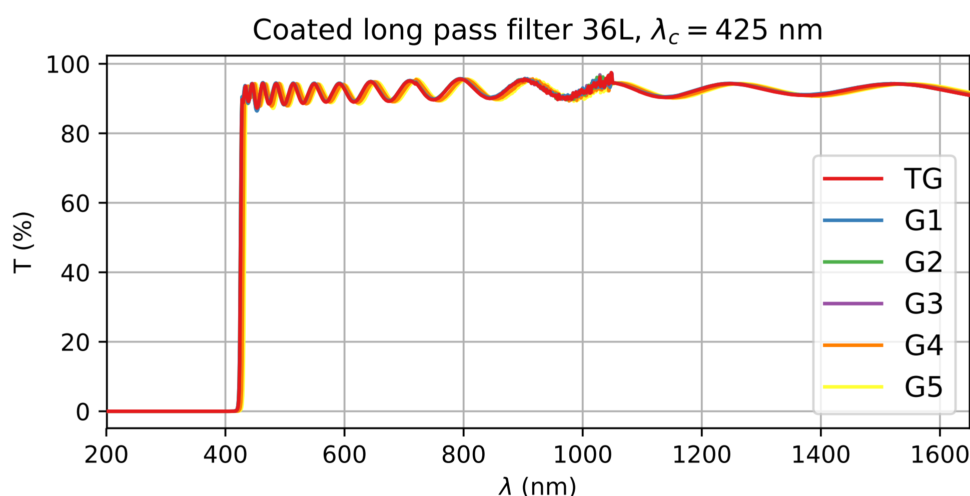

Figure 31. Transmittance profiles of the deposited LPF425 filters. 'TG' (red) is the monitoring test glass. The other glasses are numbered from the apex of the calotte ('G1') towards the edge ('G5').

The cut-on wavelength location should be located at 425 nm within ±1 % or ±4.25 nm tolerance. Coatings 'G1' - 'G3' had their cut-on points within 0.2 % tolerance margin from the desired cut-on wavelength, and the transmittance profiles of these coatings had no more than 0.5 nm shift. Coatings 'G4' and 'G5' however did not reach the cut-on wavelength tolerance limit. 'G4' deviated by 1.2 % and 'G5' by 1.7 % from the target. The slope factors were determined using equation 35. The slope factor for every coating was 0.8 % and reached the target slope factor of < 1 %.

Over the passing region (433 nm – 1650 nm) the goal was to reach $T \geq 91$ %. As can be seen in figure 32, the transmittance did not manage to stay ≥ 91 % at the oscillation minima. The transmittance also degraded very slightly close to the edge

region. Every filter had $T_{avg} \geq 92$ %, so the filters were generally satisfactory in this regard. The signal noise around $\lambda = 1000$ nm was caused by the spectrophotometer.

The optical density in the blocking region (200 nm – 415 nm) was supposed to be higher than 4, translating to $T \leq 0.01$ %. Coatings 'G1' - 'G3' did not reach OD 4 quite at $\lambda = 415$ nm. 'G4' and 'G5' had OD > 4 over the entire given blocking region. Every coating had average transmittance $T_{avg} < 0.001$ % over the entire blocking region. Thus the average optical density of each coating was higher than 5 over the blocking region. The UV absorptivity of the materials and the substrate was definitely an assisting factor at these wavelengths.

Because every coating had a similarly shaped transmittance profile, they had equally good film quality. The main difference between the profiles was the shift along λ-axis, which indicated a presence of systematic layer thickness errors caused by unequal deposition distribution. This can be improved by altering the shape of the mask which shadows a section of the calotte. As the coatings 'G4' and 'G5' had shifted towards longer wavelengths, they had increased layer thicknesses. Deposition on these glasses should be restricted by 1.2 % and 1.7 % respectively. Coatings 'G1' - 'G3' were satisfactory, having accurate cut-on locations and performing well over both passing and blocking regions on average.

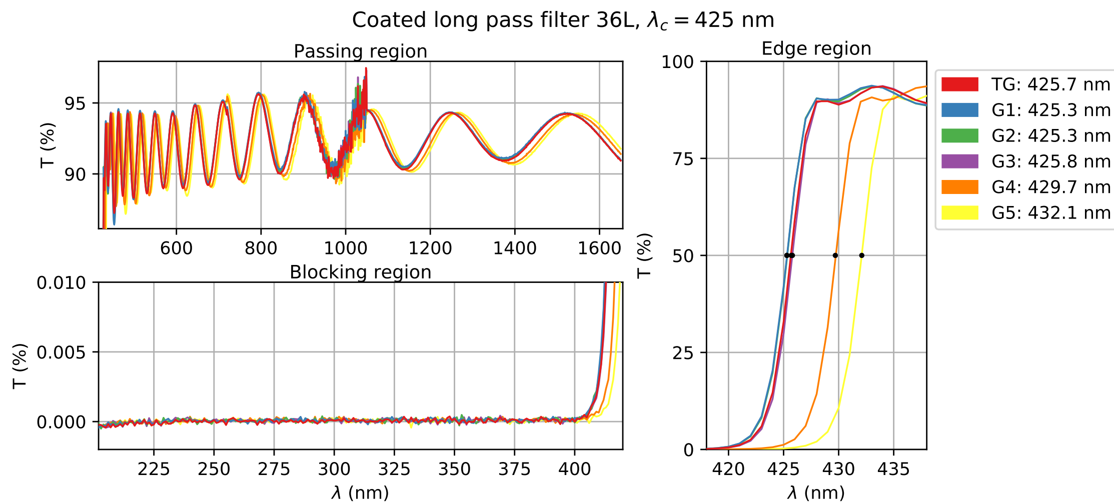

Figure 32. Transmittance profiles for the deposited LPF425 filters in the passing, blocking and edge regions. 'TG' (red) is the monitoring test glass. The other glasses are numbered from the apex of the calotte ('G1') towards the edge ('G5').

Table 5. Results for fabricated LPF425 samples. The desired specifications can be seen in table 4. 'TG' is the monitoring glass. Glass numbering begins from the apex of the calotte ('G1') towards the outermost row ('G5'). The blocking region spanned 200 nm - 415 nm, and the passing region spanned 433 nm - 1650 nm.

	TG	**G1**	**G2**	**G3**	**G4**	**G5**
$\lambda(T = 50\ \%)$ (nm)	425.7	425.3	425.3	425.8	429.7	432.1
$\lambda(T = 10\ \%)$ (nm)	423.5	423.1	423.2	423.6	427.5	429.9
$\lambda(T = 80\ \%)$ (nm)	427.0	426.7	426.7	427.1	431.1	433.5
Slope factor (%)	0.8	0.8	0.8	0.8	0.8	0.8
T_{min} (%), passing	87.2	86.4	86.5	87.1	87.7	72.6
T_{avg} (%), passing	92.4	92.5	92.4	92.4	92.3	92.2
T_{max} (%), blocking	0.0162	0.0208	0.0198	0.0152	0.003	0.0013
T_{avg} (%), blocking	0.0002	0.0003	0.0003	0.0003	0.0001	0.0001
$\lambda(T = 0.01\ \%)$ (nm)	413.0	412.4	412.5	413.1	416.6	418.8

5.4 Narrow bandpass filter

Narrow bandpass filter (NBP) is a filter that transmits over a relatively narrow bandwidth of wavelengths, and contains blocking regions on wavelengths shorter and longer than the passing region. There is no clear distinction between narrow and broad bandpass filters, but typically bandpass filters with a passing region width of a couple dozen nanometers or less are called NBPs. A bell-shape is also typical to a NBP transmissivity profile.

A narrow bandpass filter was designed to meet specifications listed in table 6. The central wavelength $\lambda_0 = 1300$ nm lies in the near-Infrared (NIR) region. The width of the passing band measured at half maximum transmittance level (FWHM) should be 25 nm. The blocking region is wide encompassing the entire operating region $200 - 3200$ nm, with the exception of the passing band. In the blocking region the average optical density should be higher than 3.0, corresponding to $T \leq 0.1$ %. A blocking region this wide can not be obtained with a Fabry-Perot filter, since they contain transmissive sidelobes. Instead an absorption type filter should be used. An absorption filter employs a metal layer through which transmissive band region can be induced using dielectric stacks.

Table 6. Optical specifications for a narrow bandpass filter. The angle of incidence is 0°. The optical density requirement is an average over the operating region, excluding the passing band.

NBP 1300-25	
Central wavelength	1300 nm
Central wavelength tolerance	± 10 nm
Transmittance	≥ 60 %
FWHM	25 nm
FWHM tolerance	± 5 nm
Optical density	≥ 3.0
Operating region	$200 - 3200$ nm

Silver (Ag) was chosen as the metal layer material. The layer thickness will have to be arbitrarily chosen at first and adjusted later to fit the bandpass into

the desired specifications. Thicker metal layer increase the optical density, which improves the blocking region but also decreases the peak transmittance and narrows down the passband. For the sake of brevity I will only show the calculations with the Ag physical layer thickness of 67 nm, which in reality was decided on after a few iterations. At $\lambda_0 = 1300$ nm the refractive index of Ag is $0.1056 + \mathrm{i}9.472$. TiO_2 and SiO_2 were used as the dielectric materials. Their respective refractive indices when $\lambda_0 = 1300$ nm are $n_{\mathrm{H}} = 2.24$ and $n_{\mathrm{L}} = 1.48$. The substrate was optical glass B270, which has a refractive index of $n_S = 1.52$. The incident medium will again be air with $n_A = 1.0$.

For calculations the incidence angle of light will be $\theta_0 = 0°$. From equations 17 and 18 we get the metal layer phase thicknesses

$$\alpha = 0.0341...$$
$$\beta = 3.0672...$$

Then we can find optimum exit admittance for the Ag layer with equations 32 and 33.

$$X = 0.8717...$$
$$Z = 9.6884...$$

thus $Y \approx 0.87 + \mathrm{i}9.69$. This metal layer exit admittance guarantees a maximum potential transmittance through the layer. From the equation 31 we can find the potential transmittance value for the Ag layer: $T_{max} \approx 79.57$ %.

The Ag layer will have a dielectric spacer layer on both sides. When the spacer layer is deposited onto the metal layer, the optical admittance of the system will begin to change as a function of the spacer thickness. Eventually the initially complex admittance value $(x - \mathrm{i}Z)$ will become a real value. According to MacLeod [7, p. 298] the real admittance value is given by:

$$\mu = \frac{2Xn_f^2}{(X^2 + Z^2 + n_f^2) + \sqrt{(X^2 + Z^2 + n_f^2)^2 - 4X^2n_f^2}} \tag{36}$$

The μ yields the combined admittance of the Ag and spacer layers when it is entirely real. The n_f is the spacer material's refractive index.

After the spacer layers there will be $(HL)^j$ QWOT stacks on both the incident and medium sides. The stacks can be designed to match the total admittance of the

system as closely as possible to the substrate admittance, or the medium admittance (both sides of the filter have to be handled separately). The better the admittances can be matched, the less transmissivity loss there will be in the filter. The matching layer count is found by calculating the stack admittance, including μ, one layer at a time, beginning with a low index layer, until a reasonable admittance match is found. According to equation 28 the sequence of admittances looks like the following:

$$\begin{aligned}
\mathrm{L}: & \frac{n_{\mathrm{L}}^2}{\mu} \\
\mathrm{LH}: & \frac{n_{\mathrm{H}}^2 \mu}{n_{\mathrm{L}}^2} \\
\mathrm{LHL}: & \frac{n_{\mathrm{L}}^4}{n_{\mathrm{H}}^2 \mu} \\
\mathrm{LHLH}: & \frac{n_{\mathrm{H}}^4 \mu}{n_{\mathrm{L}}^4}
\end{aligned}$$

...and so forth. Computational aid can then be used to compare the different solutions and choose the best one.

Ultimately TiO_2 was chosen as the spacer layer material. As an example of the admittance matching process the calculations using TiO_2 spacer will be shown.

The exit admittance of the silver layer was determined to be $Y \approx 0.87 + \mathrm{i}9.69$. Plugging $n_f = n_{\mathrm{H}} = 2.24$ into equation 36 we find the optical admittance of the Ag and spacer layers to be $\mu = 0.04391...$.

First we will handle the substrate side of the coating. We try to find the optical admittance for the dielectric stack that matches the substrate admittance $n_S = 1.52$ as closely as possible. When $n_{\mathrm{L}} = 1.48$ and $n_{\mathrm{H}} = 2.24$ the sequence looks like this:

$$\begin{aligned}
\mathrm{L}: & \frac{1.48^2}{0.044} = 49.88... \\
\mathrm{LH}: & \frac{2.24^2 * 0.044}{1.48^2} = 0.1005... \\
\mathrm{LHL}: & \frac{1.48^4}{2.24^2 * 0.044} = 21.77... \\
& ... \\
\mathrm{LHLHLHLHL}: & \frac{1.48^{10}}{2.24^8 * 0.044} = 1.8115...
\end{aligned}$$

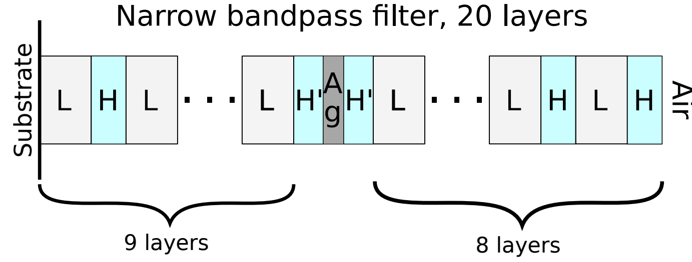

Figure 33. A diagram of the 20 layer narrow bandpass filter design. The substrate is B270 optical glass. H material is TiO_2, L material is SiO_2. H and L layers have optical thickness equal to $\lambda_0/4$, and H' layers have optical thickness of $0.85(\lambda_0/4)$. Ag layer has physical thickness of 67 nm.

At 9 layers we find an admittance sufficiently close to the substrate admittance. Therefore the substrate side of the coating will be:

$$\text{Ag}|\text{H}'\text{LHLHLHLHL}|\text{B270}$$

where H' is the non-QWOT spacer layer, whereas H and L are QWOT layers.

On the incidence medium side we have to match the stack admittance to the admittance of the medium, that is air with $n_A = 1.0$. Because the medium side gets deposited last in the coating process, it is more challenging to monitor than the substrate side. This will be further discussed later, but for now the important thing is that the less layers there are, the better. Thus there are two decent choices for layer count. With 6 quarterwave layers, beginning again with a low index layer, the optical admittance will be $(n_{\text{H}}^6\mu)/(n_{\text{L}}^6) \approx 0.53$, and with 8 layers it will be $(n_{\text{H}}^8\mu)/(n_{\text{L}}^8) \approx 1.21$. 8 layers will be chosen for the medium side stack. Thus the medium side of the coating will be:

$$\text{Ag}|\text{H}'\text{LHLHLHLH}|\text{Air}$$

The entire structure can be described by:

$$\text{B270}|\text{LHLHLHLHLH}'|\text{Ag}|\text{H}'\text{LHLHLHLH}|\text{Air}$$

Ag has physical thickness of 67 nm. L and H layers have optical thickness $\lambda_0/4 = 325$ nm. Finally the spacer layer (H') thickness was refined computationally using OptiLayer. An optimum spacer layer optical thickness was found to be 0.85 quarterwaves, or 276.2 nm. A diagram of the structure can be seen in figure 33. The complete design is also listed in the Appendix in table A5. The computed transmittance profile can be seen in figure 34.

The NBP filter consists mostly of QWOT layers, making it ideal to use λ_0 as the monitoring wavelength. However, deposition of the metal layer may be challenging to monitor optically, since it has a tremendous absorptivity and very small optical thickness. Physically 67 nm thick Ag layer has an optical thickness of barely 7 nm, or 0.022 quarterwaves when $\lambda_m = 1300$ nm. There is also a possibility that the literature value for Ag refractive index does not match the actual index, in which the case the optical monitoring can easily determine the layer termination incorrectly. Therefore QCM should be used to monitor the Ag layer.

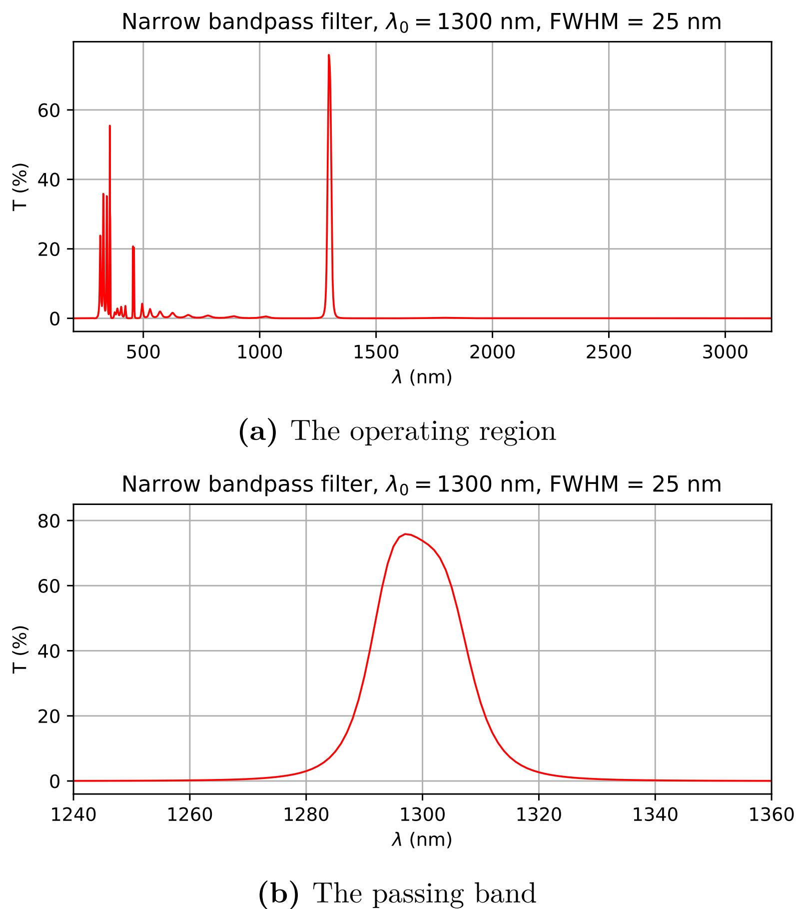

(a) The operating region

(b) The passing band

Figure 34. Theoretical transmittance profile for narrow bandpass filter with $\lambda_0 = 1300$ nm and FWHM of 25 nm. The structure of the filter is B270|LHLHLHLHLH′|Ag|H′LHLHLHLH|Air. The low index material is SiO_2 and high index material is TiO_2. L and H layers are QWOT layers, thus having optical thickness 325 nm. The H' spacer layers have optical thickness of 276.25 nm. Ag has physical thickness of 67 nm.

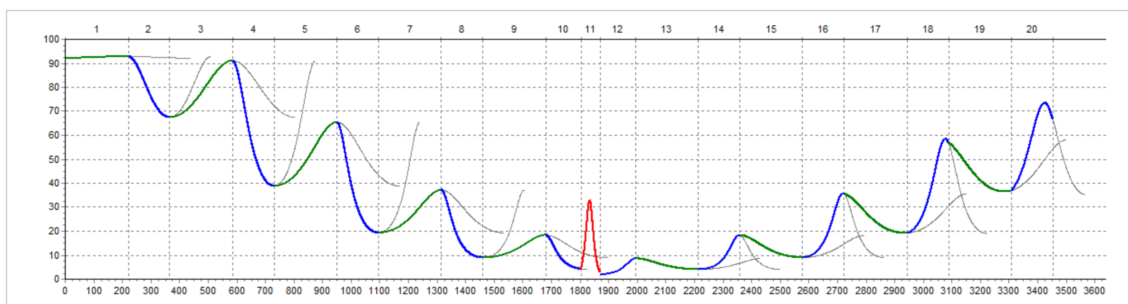

Figure 35. Monitoring report for NBP1300 design, exported from OptiLayer. The report estimates the monitored transmittance signal during the course of the deposition process. The first 10 layers (pre-Ag layers) have $\lambda_m = 1300$ nm, whereas the 9 post-Ag layers have $\lambda_m = 1294$ nm. Blue curves are high refractive index layers (TiO_2). Green curves are low refractive index layers (SiO_2). The red curve is the Ag layer. The grey curves are a visual aid showing the transmittance signal up to the next turning point if that layer was not terminated.

OptiLayer's *monitoring tool* was used to determine a suitable monitoring strategy. The QWOT layers before Ag-layer could be turning point monitored using $\lambda_0 =$ 1300 nm as the monitoring wavelength. The first layer, which is SiO_2, is an exception due to SiO_2's poor contrast against the substrate. The first layer should therefore be monitored using QCM. The spacer layers have optical thickness less than $\lambda_0/4$. Also, the spacer layers are extremely sensitive and absolutely should have the same layer thickness, otherwise the passband might degrade. Therefore it was decided they should be monitored with QCM as well. The last half of QWOT layers did not contain turning points with $\lambda_m = 1300$ nm according to OptiLayer, so their monitoring wavelength was changed to $\lambda_m = 1294$ nm. The monitoring report with these wavelengths can be seen in figure 35.

The simulation parameters in OMSVis seemed to matter only very marginally. Simulations were run using GSA value 3 and monochromator slit size 0.5 mm. The simulation results can be seen in figure A10 in the Appendix, where the transmittance profiles for the simulated coatings as well as their relative thickness errors are shown. Layers 1, 10, 11 and 12 were monitored using QCM, which was presumed to be perfectly accurate during the simulation. Therefore QCM layers have no layer thickness error present in the simulation. The simulations indicate that the errors originating from OMS are systematic and have very little effect on the deposition result. The experimental part was tried using this monitoring strategy.

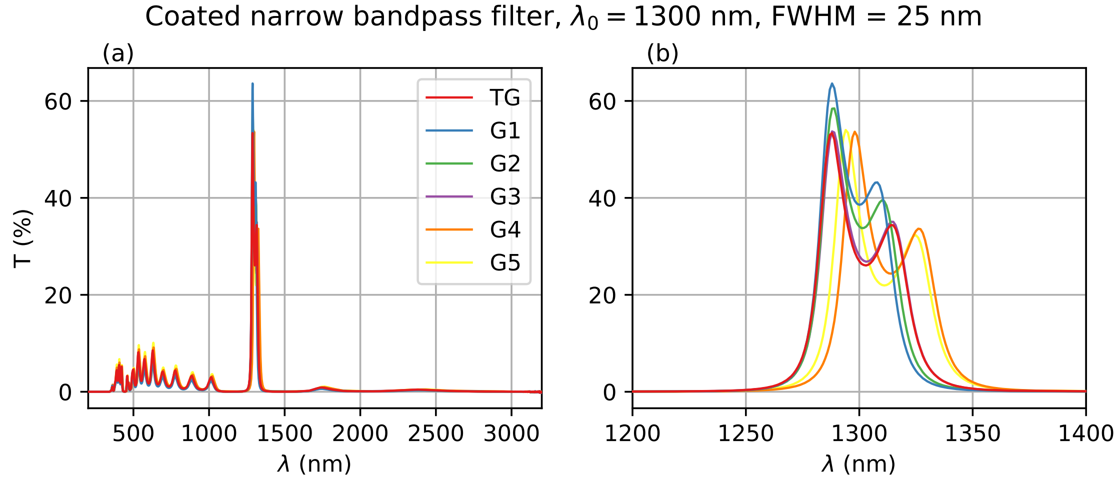

Figure 36. The measured transmittance profiles for the fabricated NBP1300 filters. **(a)** shows the transmittance over the entire operating region 200−3200 nm. **(b)** shows the bandpass region. 'TG' (red) is the monitoring glass. Numbering of the substrates starts from the apex of the calotte ('G1') towards the edge ('G5').

The measured transmittance profiles for the completed filters are shown in figure 36. Data analysis of the coatings is shown in table 7. The central wavelength was determined by integrating the bandpass transmittance and finding λ_c so that

$$\int^{\lambda_c} dT = \int_{\lambda_c} dT$$

Since data point interval was 1 nm the result wavelength has been rounded to accuracy of 1 nm. T_{peak} is the highest measured transmittance of the filter. Half maximum (HM) wavelengths are points on the wavelength axis where $T_{\mathrm{HM}} = T_{peak}/2$. In the case of multipeak band such as this, only the shortest and longest $\lambda(T_{\mathrm{HM}} = T_{peak}/2)$ points classify as HM points. The exact location of the HM points was approximated by linear interpolation. The FWHM value was calculated from the difference of HM wavelengths: $\Delta\lambda_{HM}$. Average transmission T_{avg} was calculated over the operating region, from 200 nm to 3200 nm, but excluding the passing region between the HM wavelengths from the calculation.

The transmittance profile over the band region contained two peaks, which acted as the first indication that the coating was not entirely successful. The central wavelength was specified to be located at $\lambda = 1300 \pm 10$ nm. The central wavelengths determined by surface area integration reached the specified error margin, so the transmittance peak locations were fine. The transmittance of the peak was desired

Table 7. Results for the fabricated NBP1300 filter samples. The desired specifications can be seen in table 6. The glass numbering begins from the apex of the calotte ('G1') towards the outermost row ('G5'). 'TG' is the monitoring glass. The blocking region spanned 200 nm - 3200 nm, but bandpass region between half maximum (HM) points was excluded from calculation of T_{avg}.

	TG	**G1**	**G2**	**G3**	**G4**	**G5**
$\lambda_{central}$ (nm)	1297	1295	1297	1298	1308	1305
T_{peak} (%)	53.4	63.6	58.5	53.7	53.7	54.0
λ_{HM} (nm)	1281.6	1282.1	1282.5	1282.2	1292.0	1288.2
	1319.3	1312.9	1315.5	1319.5	1331.0	1328.8
FWHM (nm)	37.7	30.8	33.1	37.2	39.0	40.5
T_{avg} (%), blocking	0.76	0.62	0.65	0.75	0.82	0.91

to be > 60 %. Only one of the coatings, 'G1' reached this level of transmission. FWHM was supposed to be 25 ± 5 nm. None of the coatings were satisfactory in this regard, as their FWHM values settled between $30 - 41$ nm. The average optical density of the filters was desired to be > 3.0, or $T_{avg} < 0.1$ %. The filters did reach OD 2 ($T_{avg} < 1$ %), but every one of them fell short of OD 3. The most notable transmission leaks can be seen in the visible light region.

Some conclusions can be drawn from the transmittance spectra and the data analysis. The central wavelength of the filters was satisfactory, so the spacer layers around the metal layer should be quite accurately deposited. If the spacer layers had systematic thickness errors, the entire passing band would shift along λ-axis. One possible reason for the division of the passband might be that the deposited metal layer was too thin. The higher than desired T_{avg} and FWHM values could also imply the metal layer probably was not thick enough. Another cause for the passband division could be that there was a design fault in one or both of the QWOT stacks. The QWOT stacks were designed to match the admittance of the spacer-metal-spacer layer system to the substrate and exit mediums. A fault in the stack design could implicate that the theoretical refractive index of the Ag did not match the actual index. Refractive index online database [30] lists a few dispersion measurements for silver. The results slightly differ from each other, so it would be possible that the index N of the deposited silver did not match the theory. The actual N of the Ag may have to be determined in the future, which could lead to redesigning the filter.

6 Conclusion

Four different types of optical filters were fabricated utilizing optical layer thickness monitoring. The used optical monitoring technique was intermittent transmittance monitoring measured directly from a coated substrate. The fabricated filters were a Bragg mirror, a short wavelength pass edge filter, a long wavelength pass edge filter and a narrow bandpass filter. Computational methods were used for the filter design processes and for planning monitoring strategies. The designs were created to be as suitable as possible for optical monitoring. The filters were fabricated using plasma-assisted electron beam evaporation in a high vacuum.

The Bragg mirror was fabricated twice using slightly different monitoring strategies. The first monitoring strategy used a monitoring wavelength longer than the central wavelength of the coating. The second strategy used the exact central wavelength for monitoring. The film quality was equally good in both processes, but the second batch had better reflection band location on λ-axis. The first batch had slightly shifted because of the monitoring wavelength choice, although the spectral performance was still great. This result will be useful when designing monitoring strategies for UV-filters.

The short pass filter was fabricated twice as well, first using two monitoring glasses and then using four monitoring glasses. The results were similar to each other. Both methods produced filters with great blocking regions easily reaching average optical density higher than 4. Optical density > 5 could realistically be reached. The passing regions were not satisfactory. Transmittances at the passing region oscillated between 80 % − 90 %, even though $T \geq 91$ % was desired. Also, both coatings exhibited drops in transmittance when $\lambda < 400$ nm and at $\lambda \approx 460$ nm. Computational analysis would indicate that the latter narrow drop was caused by either layer thickness variance or layer inhomogeneity. The short wavelength transmittance drop was likely caused by absorption. To counter the absorption, the substrate material and likely TiO_2 layer material should be changed to non-absorbing materials. For example Ta_2O_5 could be tried as the high index material. The cut-off point locations and edge steepnesses were satisfactory for most of the samples. Out

of total nine test filters only one failed to meet the cut-off error tolerance limit. The edge steepness or slope factor was at least passable for seven samples. 4TG filters generally had worse slope factors than the 2TG filters. 2TG monitoring seemed to yield slightly better results, possibly because the error self-compensation was more pronounced when using only two monitoring glasses.

A long pass filter with blocking region at UV wavelengths was designed and fabricated using a single monitoring glass. The blocking region was extended into the UV region using the absorptance of both the substrate glass (B270) and TiO_2. The filter turned out satisfying. The blocking region was excellent having optical density > 5. The passing region was not quite as transmissive as predicted by the theoretical model, but managed to reach $T_{avg} > 92$ %. The edge steepness was satisfying for all the samples. Three of the five samples, as well as the monitoring glass, had their edge location well within the given tolerance.

A narrow bandpass filter was designed to be an absorption type filter with an induced transmitting region. Silver was decided to be used as the absorbing layer material in order to achieve the 3 μm wide blocking region from UV to IR. Two QWOT stacks of TiO_2 and SiO_2 were used to induce the transmitting region. The silver layer was monitored using QCM, which may have led to an incorrect Ag layer thickness due to an incorrect quartz crystal monitoring correction factor. Also the actual silver refractive index may have not matched the literature value used during the design process. The fabricated filter batch suffered from a poorly shaped bandpass, which was not only too wide but had also divided in the middle. Both the Ag layer thickness and the Ag real dispersion have to be researched more to improve the filter.

Optical monitoring has been established as a compelling layer thickness monitoring method. It offers some considerable advantages over the regular quartz crystal monitoring. Most importantly the ability to monitor the optical thickness of the film as well as the error self-compensation phenomena allow the fabrication of complicated and sensitive optical filters. The challenges of optical monitoring can be complemented by using physical thickness monitoring in parallel.

References

[1] H. K. Raut et al. “Anti-reflective coatings: A critical, in-depth review”. In: *Energy Environ. Sci.* 4 (10 2011), pp. 3779–3804. DOI: 10.1039/C1EE01297E.

[2] M. Banning. “Practical Methods of Making and Using Multilayer Filters”. In: *J. Opt. Soc. Am.* 37.10 (1947), pp. 792–797. DOI: 10.1364/JOSA.37.000792.

[3] R. Paschotta. article on ’beam splitters’ in the *RP Photonics Encyclopedia,* https://www.rp-photonics.com/beam_splitters.html. Accessed on 2019-04-18.

[4] T. Begou, F. Lemarchand, and J. Lumeau. “Advanced optical interference filters based on metal and dielectric layers”. In: *Opt. Express* 24.18 (2016), pp. 20925–20937. DOI: 10.1364/OE.24.020925.

[5] K. Hendrix et al. “Demonstration of narrowband notch and multi-notch filters”. In: *Proc SPIE* 7067 (2008). DOI: 10.1117/12.795498.

[6] A. V. Tikhonravov and M. K. Trubetskov. “Computational manufacturing as a bridge between design and production”. In: *Appl. Opt.* 44.32 (2005), pp. 6877–6884. DOI: 10.1364/AO.44.006877.

[7] H. Macleod. *Thin-film optical filters*. 866 Third Avenue, New York 10022, USA: Macmillan Publishing Company, 1986. ISBN: 0-02-948110-4.

[8] P. Bousquet et al. “Optical filters: Monitoring process allowing the auto-correction of thickness errors”. In: *Thin Solid Films* 13.2 (1972), pp. 285 –290. ISSN: 0040-6090. DOI: https://doi.org/10.1016/0040-6090(72)90297-0.

[9] M. J. Madou. *Fundamentals of microfabrication: the science of miniaturization 2nd ed.* 2000 N.W. Corporate Blvd., Boca Raton, Florida 33431: CRC Press LLC, 2001. ISBN: 0-8493-0826-7.

[10] B. Schroeder et al. “Modelling and Simulation of the Advanced Plasma Source”. In: *Journal of Applied Physics* 110.4 (2011), p. 043305. DOI: 10.1063/1.3626806.

[11] P. J. Martin. “Ion-based methods for optical thin film deposition”. In: *Journal of Materials Science* 21.1 (1986), pp. 1–25. DOI: 10.1007/BF01144693.

[12] Edmund Optics, *An introduction to Optical Coatings.* https://www.edmundoptics.eu/resources/application-notes/optics/an-introduction-to-optical-coatings/. Accessed on 2019-05-29.

[13] J. D. Rancourt. *Optical Thin Films: Users' Handbook.* 866 Third Avenue, New York 10022, USA: Macmillan Publishing Company, 1987. ISBN: 0-02-947700-X.

[14] K. Iwahori et al. “Optical properties of fluoride thin films deposited by RF magnetron sputtering”. In: *Appl. Opt.* 45.19 (2006), pp. 4598–4602. DOI: 10.1364/AO.45.004598.

[15] D. W. Morelli. *Interference Filter Handbook.* 2789 Northpoint Parkway, Santa Rosa, USA: JDS Uniphase Corporation, 2006.

[16] P. Kelly and R. Arnell. “Magnetron sputtering: a review of recent developments and applications”. In: *Vacuum* 56.3 (2000), pp. 159 –172. ISSN: 0042-207X. DOI: https://doi.org/10.1016/S0042-207X(99)00189-X.

[17] M. Scherer, J. Pistner, and W. Lehnert. “UV- and VIS Filter Coatings by Plasma Assisted Reactive Magnetron Sputtering (PARMS)”. In: *Optical Interference Coatings.* Optical Society of America, 2010, MA7. DOI: 10.1364/OIC.2010.MA7.

[18] T. Begou et al. *Complex optical interference filter with stress compensation.* 2015. DOI: 10.1117/12.2191967.

[19] S. M. George, A. W. Ott, and J. W. Klaus. “Surface Chemistry for Atomic Layer Growth”. In: *The Journal of Physical Chemistry* 100.31 (1996), pp. 13121–13131. DOI: 10.1021/jp9536763.

[20] S. M. George. “Atomic Layer Deposition: An Overview”. In: *Chemical Reviews* 110.1 (2010), pp. 111–131. DOI: 10.1021/cr900056b.

[21] “A brief review of atomic layer deposition: from fundamentals to applications”. In: *Materials Today* 17.5 (2014), pp. 236 –246. ISSN: 1369-7021. DOI: https://doi.org/10.1016/j.mattod.2014.04.026.

[22] A. Piegari and F. Flory. *Optical thin films and coatings.* 80 High Street, Sawston, UK: Woodhead Publishing Limited, 2013. ISBN: 978-0-85709-594-7.

[23] H. A. Macleod. “Monitoring of optical coatings”. In: *Appl. Opt.* 20.1 (1981), pp. 82–89. DOI: 10.1364/AO.20.000082.

[24] H. Macleod. “Turning Value Monitoring of Narrow-band All-dielectric Thin-film Optical Filters”. In: *Optica Acta: International Journal of Optics* 19.1 (1972), pp. 1–28. DOI: 10.1080/713818494.

[25] B. Vidal and E. Pelletier. “Nonquarterwave multilayer filters: optical monitoring with a minicomputer allowing correction of thickness errors”. In: *Appl. Opt.* 18.22 (1979), pp. 3857–3862. DOI: 10.1364/AO.18.003857.

[26] B. T. Sullivan and J. A. Dobrowolski. “Deposition error compensation for optical multilayer coatings. I. Theoretical description”. In: *Appl. Opt.* 31.19 (1992), pp. 3821–3835. DOI: 10.1364/AO.31.003821.

[27] A. V. Tikhonravov and M. K. Trubetskov. “Automated design and sensitivity analysis of wavelengh-division multiplexing filters”. In: *Applied Optics* 41.16 (2002), pp. 3176–3182. DOI: 10.1364/AO.41.003176.

[28] *OptiLayer* homepage. https://www.optilayer.com. Accessed on 2019-04-23.

[29] A. V. Tikhonravov and M. K. Trubetskov. “Elimination of cumulative effect of thickness errors in monochromatic monitoring of optical coating production: theory”. In: *Appl. Opt.* 46.11 (2007), pp. 2084–2090. DOI: 10.1364/AO.46.002084.

[30] M. N. Polyanskiy. *Refractive index database*. https://refractiveindex.info. Accessed on 2018-10-31.

[31] J. R. Jacobsson. *Review of the optical properties of inhomogeneous thin films*. 1993. DOI: 10.1117/12.163540.

[32] P. G. Verly. *Design of inhomogenous and quasi-inhomogenous optical coatings at the NRC*. 1993. DOI: 10.1117/12.163557.

[33] B. G. Bovard. *Graded index rugate filters: power-sine rugate structures*. 1993. DOI: 10.1117/12.163541.

[34] H. K. Pulker. “Characterization of optical thin films”. In: *Appl. Opt.* 18.12 (1979), pp. 1969–1977. DOI: 10.1364/AO.18.001969.

[35] J. P. Borgogno, B. Lazarides, and E. Pelletier. “Automatic determination of the optical constants of inhomogeneous thin films”. In: *Appl. Opt.* 21.22 (1982), pp. 4020–4029. DOI: 10.1364/AO.21.004020.

[36] A. V. Tikhonravov et al. "Influence of small inhomogeneities on the spectral characteristics of single thin films". In: *Appl. Opt.* 36.28 (1997), pp. 7188–9198. DOI: 10.1364/AO.36.007188.

[37] Babar and Weaver. *Refractive index of Ag, datasheet.* https://refractiveindex.info/?shelf=main&book=Ag&page=Babar. Accessed on 2018-12-22.

[38] S. Pongratz and A. Zöller. "Plasma ion-assisted deposition: A promising technique for optical coatings". In: *Journal of Vacuum Science & Technology A* 10.4 (1992), pp. 1897–1904. DOI: 10.1116/1.578112.

[39] A. Zöller et al. *Plasma-ion-assisted deposition: a powerful technology for the production of optical coatings.* 1997. DOI: 10.1117/12.290193.

[40] H. K. Pulker, G. Paesold, and E. Ritter. "Refractive indices of TiO2 films produced by reactive evaporation of various titanium--oxygen phases". In: *Appl. Opt.* 15.12 (1976), pp. 2986–2991. DOI: 10.1364/AO.15.002986.

[41] Özlem Duyar, F. Placido, and H. Z. Durusoy. "Optimization of TiO 2 films prepared by reactive electron beam evaporation of Ti3O5". In: *Journal of Physics D: Applied Physics* 41.9 (2008), p. 095307.

Appendix

Coating designs

Table A1. Structure of the Bragg mirror with $\lambda_0 = 346$ nm. Layer material, physical thickness and optical thickness are displayed. QWOT is a ratio between the optical thickness of the layer and the quarter value of the central wavelength: $4d/\lambda_0$.

Layer	**Material**	**Phys.Th.**	**Opt.Th.**	**QWOT**
1	HfO_2	41.6 nm	86.5 nm	1.0
2	SiO_2	57.4 nm	86.5 nm	1.0
3	HfO_2	41.6 nm	86.5 nm	1.0
4	SiO_2	57.4 nm	86.5 nm	1.0
5	HfO_2	41.6 nm	86.5 nm	1.0
6	SiO_2	57.4 nm	86.5 nm	1.0
7	HfO_2	41.6 nm	86.5 nm	1.0
8	SiO_2	57.4 nm	86.5 nm	1.0
9	HfO_2	41.6 nm	86.5 nm	1.0
10	SiO_2	57.4 nm	86.5 nm	1.0
11	HfO_2	41.6 nm	86.5 nm	1.0
Substrate: BK7			Incidence medium: Air	

Table A2. Structure of the short wavelength pass edge filter with $\lambda_c = 625$ nm using 2 monitoring glasses. Layer material, physical thickness and optical thickness are displayed. QWOT is a ratio between the optical thickness of the layer and the quarter value of the monitoring wavelength, $4d/\lambda_m$. Glass number indicates which monitoring glass is used for the layer.

Layer	Material	Phys.Th.	Opt.Th.	QWOT	Glass
1	SiO_2	216.6 nm	320.5 nm	1.676	1
2	TiO_2	86.7 nm	196.2 nm	1.026	1
3	SiO_2	149.2 nm	220.7 nm	1.154	1
4	TiO_2	90.8 nm	205.4 nm	1.074	1
5	SiO_2	153.4 nm	227.0 nm	1.187	1
6	TiO_2	92.0 nm	208.1 nm	1.088	1
7	SiO_2	154.3 nm	228.4 nm	1.194	1
8	TiO_2	92.0 nm	208.3 nm	1.089	1
9	SiO_2	153.9 nm	227.8 nm	1.191	1
10	TiO_2	92.4 nm	209.0 nm	1.093	1
11	SiO_2	152.5 nm	225.7 nm	1.18	1
12	TiO_2	94.0 nm	212.7 nm	1.112	1
13	SiO_2	152.3 nm	225.3 nm	1.178	1
14	TiO_2	92.6 nm	209.4 nm	1.095	1
15	SiO_2	151.8 nm	224.5 nm	1.174	1
16	TiO_2	94.4 nm	213.6 nm	1.117	1
17	SiO_2	152.0 nm	224.9 nm	1.176	1
18	TiO_2	92.1 nm	208.5 nm	1.09	1
19	SiO_2	152.8 nm	226.1 nm	1.182	1
20	TiO_2	92.3 nm	208.8 nm	1.092	1
21	SiO_2	153.6 nm	227.2 nm	1.188	1
22	TiO_2	93.7 nm	212.1 nm	1.109	1
23	SiO_2	152.4 nm	225.5 nm	1.179	1
24	TiO_2	91.7 nm	207.5 nm	1.085	1
25	SiO_2	152.0 nm	224.9 nm	1.176	1
26	TiO_2	94.6 nm	214.0 nm	1.119	1
27	SiO_2	152.0 nm	224.9 nm	1.176	1
28	TiO_2	92.1 nm	208.5 nm	1.09	1
29	SiO_2	150.2 nm	222.2 nm	1.162	1
30	TiO_2	92.6 nm	209.6 nm	1.096	1
31	SiO_2	153.2 nm	226.6 nm	1.185	1
32	TiO_2	90.4 nm	204.6 nm	1.07	1
33	SiO_2	146.1 nm	216.1 nm	1.13	1
34	TiO_2	81.0 nm	183.2 nm	0.958	1
35	SiO_2	130.2 nm	192.6 nm	1.007	1
36	TiO_2	77.0 nm	176.5 nm	1.124	2
37	SiO_2	133.3 nm	197.7 nm	1.259	2
38	TiO_2	73.6 nm	168.8 nm	1.075	2
39	SiO_2	127.3 nm	188.7 nm	1.202	2
40	TiO_2	73.9 nm	169.4 nm	1.079	2
41	SiO_2	128.3 nm	190.1 nm	1.211	2
42	TiO_2	73.4 nm	168.3 nm	1.072	2
43	SiO_2	129.2 nm	191.5 nm	1.22	2
44	TiO_2	72.4 nm	165.9 nm	1.057	2
45	SiO_2	129.7 nm	192.2 nm	1.224	2
46	TiO_2	71.4 nm	163.8 nm	1.043	2
47	SiO_2	128.4 nm	190.3 nm	1.212	2
48	TiO_2	72.0 nm	165.0 nm	1.051	2
49	SiO_2	128.7 nm	190.8 nm	1.215	2
50	TiO_2	72.2 nm	165.6 nm	1.055	2
51	SiO_2	129.0 nm	191.2 nm	1.222	2
52	TiO_2	71.8 nm	164.6 nm	1.052	2
53	SiO_2	129.3 nm	191.7 nm	1.225	2
54	TiO_2	72.1 nm	165.4 nm	1.057	2
55	SiO_2	127.2 nm	188.6 nm	1.205	2
56	TiO_2	73.1 nm	167.8 nm	1.072	2
57	SiO_2	127.3 nm	188.7 nm	1.206	2
58	TiO_2	73.5 nm	168.7 nm	1.078	2
59	SiO_2	127.4 nm	188.9 nm	1.207	2
60	TiO_2	72.4 nm	166.0 nm	1.061	2
61	SiO_2	127.4 nm	188.9 nm	1.207	2
62	TiO_2	72.9 nm	167.3 nm	1.069	2
63	SiO_2	126.5 nm	187.5 nm	1.198	2
64	TiO_2	73.3 nm	168.2 nm	1.075	2
65	SiO_2	127.5 nm	189.1 nm	1.208	2
66	TiO_2	73.1 nm	167.8 nm	1.072	2
67	SiO_2	128.5 nm	190.5 nm	1.217	2
68	TiO_2	72.2 nm	165.6 nm	1.058	2
69	SiO_2	128.2 nm	190.0 nm	1.214	2
70	TiO_2	74.7 nm	171.4 nm	1.095	2
71	SiO_2	128.5 nm	190.5 nm	1.217	2
72	TiO_2	74.4 nm	170.7 nm	1.091	2
73	SiO_2	136.8 nm	202.8 nm	1.296	2
74	TiO_2	72.9 nm	167.3 nm	1.069	2
75	SiO_2	14.6 nm	21.6 nm	0.138	2
76	TiO_2	11.3 nm	25.8 nm	0.165	2
77	SiO_2	210.2 nm	311.6 nm	1.991	2

Substrate: BK7 Incidence medium: Air

Table A3. Structure of the short wavelength pass edge filter with $\lambda_c = 625$ nm using 4 monitoring glasses. Layer material, physical thickness and optical thickness are displayed. QWOT is a ratio between the optical thickness of the layer and the quarter value of the monitoring wavelength, $4d/\lambda_m$. Glass number indicates which monitoring glass is used for the layer.

Layer	Material	Phys.Th.	Opt.Th.	QWOT	Glass	Layer	Material	Phys.Th.	Opt.Th.	QWOT	Glass
1	SiO_2	216.6 nm	320.5 nm	1.676	1	40	TiO_2	73.9 nm	169.4 nm	1.079	3
2	TiO_2	86.7 nm	196.2 nm	1.026	1	41	SiO_2	128.3 nm	190.1 nm	1.211	3
3	SiO_2	149.2 nm	220.7 nm	1.154	1	42	TiO_2	73.4 nm	168.3 nm	1.072	3
4	TiO_2	90.8 nm	205.4 nm	1.074	1	43	SiO_2	129.2 nm	191.5 nm	1.22	3
5	SiO_2	153.4 nm	227.0 nm	1.187	1	44	TiO_2	72.4 nm	165.9 nm	1.057	3
6	TiO_2	92.0 nm	208.1 nm	1.088	1	45	SiO_2	129.7 nm	192.2 nm	1.224	3
7	SiO_2	154.3 nm	228.4 nm	1.194	1	46	TiO_2	71.4 nm	163.8 nm	1.043	3
8	TiO_2	92.0 nm	208.3 nm	1.089	1	47	SiO_2	128.4 nm	190.3 nm	1.212	3
9	SiO_2	153.9 nm	227.8 nm	1.191	1	48	TiO_2	72.0 nm	165.0 nm	1.051	3
10	TiO_2	92.4 nm	209.0 nm	1.093	1	49	SiO_2	128.7 nm	190.8 nm	1.215	3
11	SiO_2	152.5 nm	225.7 nm	1.18	1	50	TiO_2	72.2 nm	165.6 nm	1.055	3
12	TiO_2	94.0 nm	212.7 nm	1.112	1	51	SiO_2	129.0 nm	191.2 nm	1.218	3
13	SiO_2	152.3 nm	225.3 nm	1.178	1	52	TiO_2	71.8 nm	164.5 nm	1.048	3
14	TiO_2	92.6 nm	209.4 nm	1.095	1	53	SiO_2	129.3 nm	191.7 nm	1.221	3
15	SiO_2	151.8 nm	224.5 nm	1.174	1	54	TiO_2	72.1 nm	165.3 nm	1.053	3
16	TiO_2	94.4 nm	213.6 nm	1.117	2	55	SiO_2	127.2 nm	188.6 nm	1.201	3
17	SiO_2	152.0 nm	224.9 nm	1.176	2	56	TiO_2	73.1 nm	167.8 nm	1.072	4
18	TiO_2	92.1 nm	208.5 nm	1.09	2	57	SiO_2	127.3 nm	188.7 nm	1.206	4
19	SiO_2	152.8 nm	226.1 nm	1.182	2	58	TiO_2	73.5 nm	168.7 nm	1.078	4
20	TiO_2	92.3 nm	208.8 nm	1.092	2	59	SiO_2	127.4 nm	188.9 nm	1.207	4
21	SiO_2	153.6 nm	227.2 nm	1.188	2	60	TiO_2	72.4 nm	166.0 nm	1.061	4
22	TiO_2	93.7 nm	212.1 nm	1.109	2	61	SiO_2	127.4 nm	188.9 nm	1.207	4
23	SiO_2	152.4 nm	225.5 nm	1.179	2	62	TiO_2	72.9 nm	167.3 nm	1.069	4
24	TiO_2	91.7 nm	207.5 nm	1.085	2	63	SiO_2	126.5 nm	187.5 nm	1.198	4
25	SiO_2	152.0 nm	224.9 nm	1.176	2	64	TiO_2	73.3 nm	168.2 nm	1.075	4
26	TiO_2	94.6 nm	214.0 nm	1.119	2	65	SiO_2	127.5 nm	189.1 nm	1.208	4
27	SiO_2	152.0 nm	224.9 nm	1.176	2	66	TiO_2	73.1 nm	167.8 nm	1.072	4
28	TiO_2	92.1 nm	208.5 nm	1.09	2	67	SiO_2	128.5 nm	190.5 nm	1.217	4
29	SiO_2	150.2 nm	222.2 nm	1.162	2	68	TiO_2	72.2 nm	165.6 nm	1.058	4
30	TiO_2	92.6 nm	209.6 nm	1.096	2	69	SiO_2	128.2 nm	190.0 nm	1.214	4
31	SiO_2	153.2 nm	226.6 nm	1.185	2	70	TiO_2	74.7 nm	171.4 nm	1.095	4
32	TiO_2	90.4 nm	204.6 nm	1.07	2	71	SiO_2	128.5 nm	190.5 nm	1.217	4
33	SiO_2	146.1 nm	216.1 nm	1.13	2	72	TiO_2	74.4 nm	170.7 nm	1.091	4
34	TiO_2	81.0 nm	185.7 nm	1.183	3	73	SiO_2	136.8 nm	202.8 nm	1.296	4
35	SiO_2	130.2 nm	193.0 nm	1.229	3	74	TiO_2	72.9 nm	167.3 nm	1.069	4
36	TiO_2	77.0 nm	176.5 nm	1.124	3	75	SiO_2	14.6 nm	21.6 nm	0.138	4
37	SiO_2	133.3 nm	197.7 nm	1.259	3	76	TiO_2	11.3 nm	25.8 nm	0.165	4
38	TiO_2	73.6 nm	168.8 nm	1.075	3	77	SiO_2	210.2 nm	311.6 nm	1.991	4
39	SiO_2	127.3 nm	188.7 nm	1.202	3						

Substrate: BK7 Incidence medium: Air

Table A4. Structure of the long wavelength pass edge filter with $\lambda_c = 425$ nm. Layer material, physical thickness and optical thickness are displayed. QWOT is a ratio between the optical thickness of the layer and the quarter value of the monitoring wavelength, $4d/\lambda_m$.

Layer	Material	Phys.Th.	Opt.Th.	QWOT
1	TiO_2	24.5 nm	66.3 nm	0.716
2	SiO_2	61.9 nm	92.7 nm	1.003
3	TiO_2	28.6 nm	77.3 nm	0.836
4	SiO_2	57.5 nm	86.1 nm	0.931
5	TiO_2	36.8 nm	99.6 nm	1.077
6	SiO_2	54.5 nm	81.6 nm	0.882
7	TiO_2	37.5 nm	101.5 nm	1.098
8	SiO_2	54.9 nm	82.2 nm	0.889
9	TiO_2	37.0 nm	100.0 nm	1.081
10	SiO_2	57.2 nm	85.6 nm	0.926
11	TiO_2	36.2 nm	97.8 nm	1.058
12	SiO_2	58.6 nm	87.7 nm	0.949
13	TiO_2	35.3 nm	95.4 nm	1.032
14	SiO_2	59.7 nm	89.4 nm	0.967
15	TiO_2	35.3 nm	95.4 nm	1.032
16	SiO_2	59.3 nm	88.8 nm	0.96
17	TiO_2	35.7 nm	96.4 nm	1.043
18	SiO_2	58.0 nm	86.8 nm	0.939
19	TiO_2	36.7 nm	99.3 nm	1.074
20	SiO_2	56.9 nm	85.2 nm	0.921
21	TiO_2	36.9 nm	99.7 nm	1.078
22	SiO_2	58.1 nm	87.0 nm	0.941
23	TiO_2	35.1 nm	95.0 nm	1.027
24	SiO_2	61.3 nm	91.8 nm	0.993
25	TiO_2	33.4 nm	90.3 nm	0.977
26	SiO_2	63.0 nm	94.4 nm	1.02
27	TiO_2	34.0 nm	91.8 nm	0.993
28	SiO_2	57.8 nm	86.5 nm	0.935
29	TiO_2	38.1 nm	103.0 nm	1.114
30	SiO_2	50.5 nm	75.6 nm	0.818
31	TiO_2	41.4 nm	111.9 nm	1.209
32	SiO_2	49.1 nm	73.6 nm	0.795
33	TiO_2	36.2 nm	97.9 nm	1.059
34	SiO_2	58.9 nm	88.2 nm	0.953
35	TiO_2	24.6 nm	66.4 nm	0.718
36	SiO_2	132.9 nm	199.0 nm	2.152
Substrate: B270			Incidence medium: Air	

Table A5. Complete structure for narrow bandpass filter with $\lambda_0 = 1300$ nm and FWHM = 25 nm. Layer material, physical thickness and optical thickness are displayed. QWOT is a ratio between the optical thickness of the layer and the quarter value of the monitoring wavelength, $4d/\lambda_m$.

Layer	Material	Phys.Th.	Opt.Th.	QWOT
1	SiO_2	220.1 nm	325.0 nm	1.0
2	TiO_2	144.9 nm	325.0 nm	1.0
3	SiO_2	220.1 nm	325.0 nm	1.0
4	TiO_2	144.9 nm	325.0 nm	1.0
5	SiO_2	220.1 nm	325.0 nm	1.0
6	TiO_2	144.9 nm	325.0 nm	1.0
7	SiO_2	220.1 nm	325.0 nm	1.0
8	TiO_2	144.9 nm	325.0 nm	1.0
9	SiO_2	220.1 nm	325.0 nm	1.0
10	TiO_2	123.2 nm	276.2 nm	0.85
11	Ag	67.0 nm	7.0 nm	0.022
12	TiO_2	123.2 nm	276.2 nm	0.854
13	SiO_2	220.1 nm	325.0 nm	1.005
14	TiO_2	144.9 nm	325.0 nm	1.005
15	SiO_2	220.1 nm	325.0 nm	1.005
16	TiO_2	144.9 nm	325.0 nm	1.005
17	SiO_2	220.1 nm	325.0 nm	1.005
18	TiO_2	144.9 nm	325.0 nm	1.005
19	SiO_2	220.1 nm	325.0 nm	1.005
20	TiO_2	144.9 nm	325.0 nm	1.005
Substrate: B270			Incidence medium: Air	

Simulation results

Bragg mirror

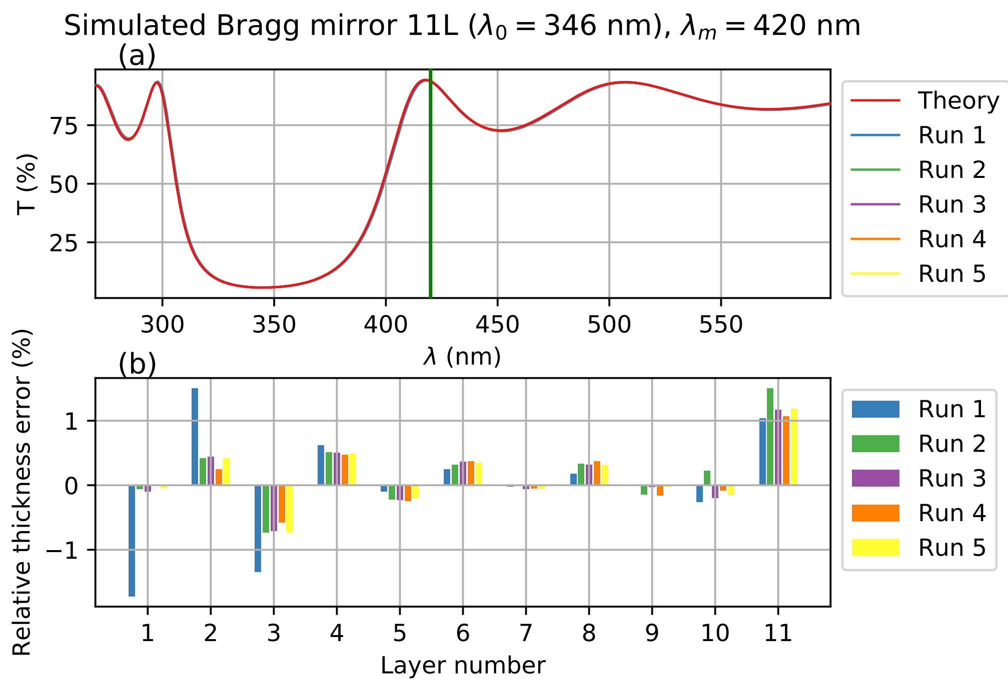

Figure A1. **(a)** Transmittance profiles of five simulated Bragg mirror coatings, as well as the theoretical profile. $\lambda_m = 420$ nm. **(b)** Relative layer thickness errors of the simulated Bragg mirrors.

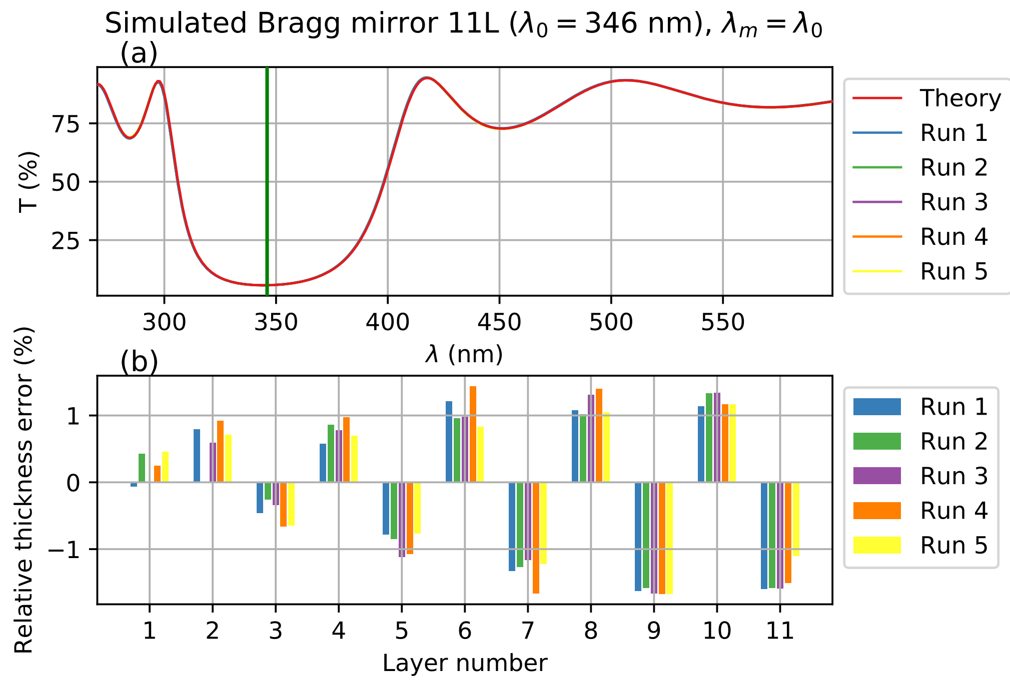

Figure A2. **(a)** Transmittance profiles of five simulated Bragg mirror coatings, as well as the theoretical profile. $\lambda_m = \lambda_0 = 346$ nm. **(b)** Relative layer thickness errors of the simulated Bragg mirrors.

Short pass edge filter

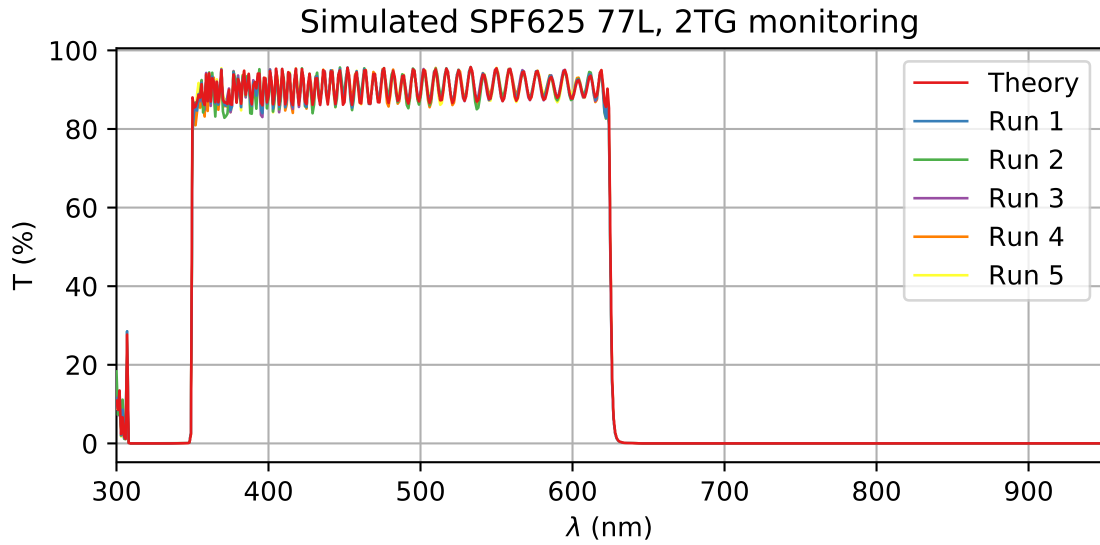

Figure A3. Transmittance profiles of five simulated SPF625 77L depositions using two monitoring glasses. Theoretical profile is shown for comparison.

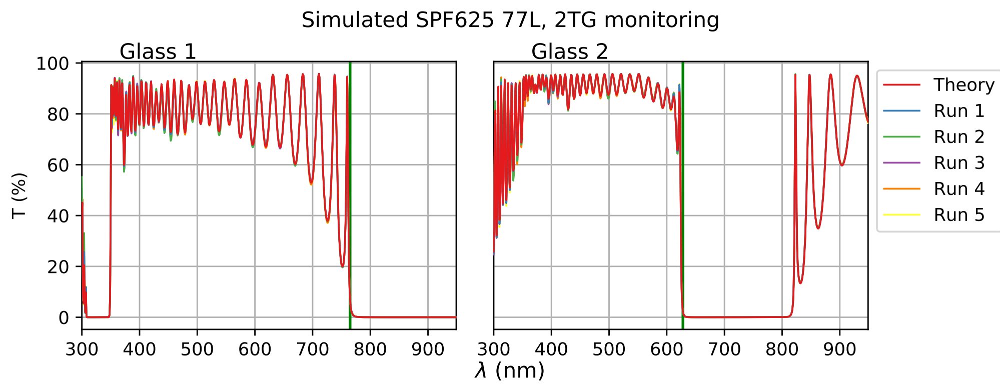

Figure A4. Simulated transmittance profiles of two monitoring glasses used in virtual SPF625 77L depositions. Theoretical profile is shown for comparison. The green lines show the used monitoring wavelength for that glass.

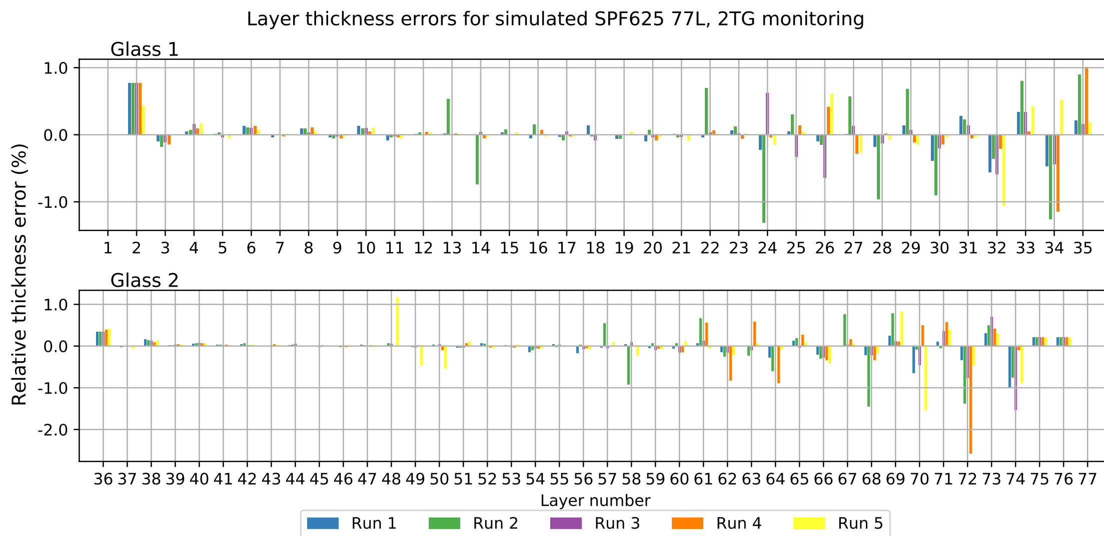

Figure A5. Relative layer thickness errors in the simulated SPF625 77L depositions when using two monitoring glasses.

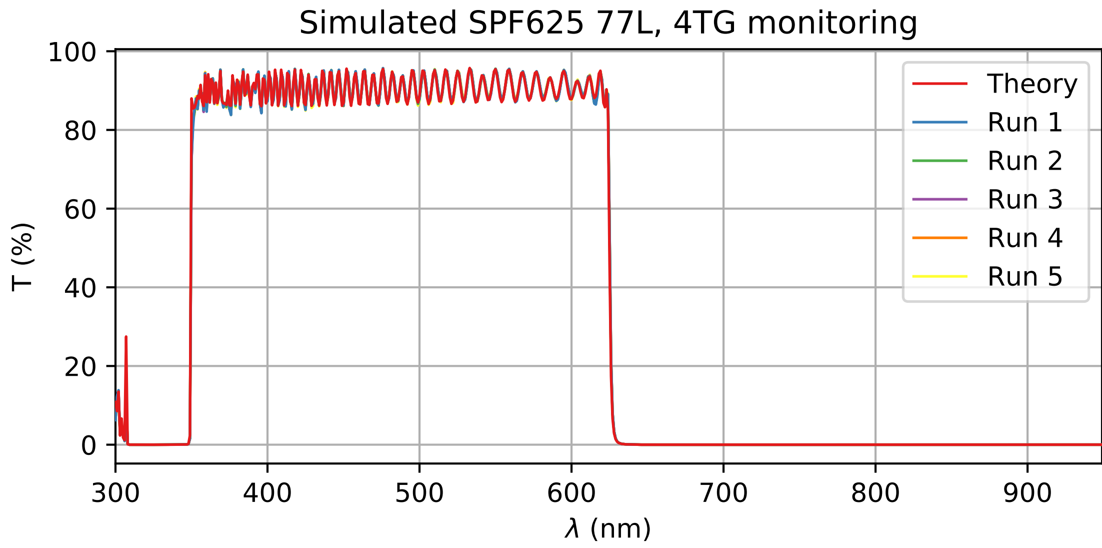

Figure A6. Transmittance profiles of five simulated SPF625 77L depositions using four monitoring glasses. Theoretical profile is shown for comparison.

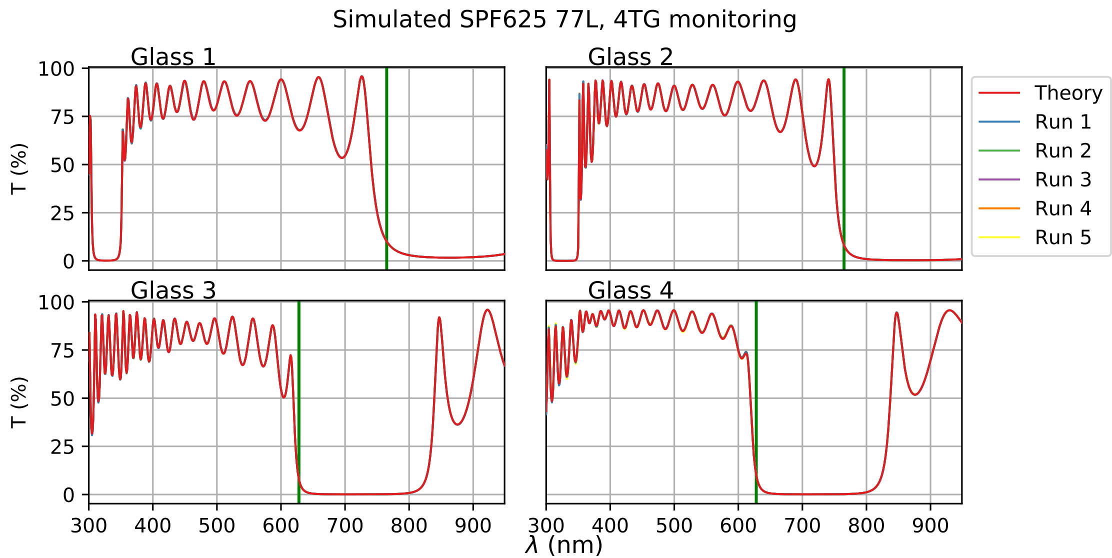

Figure A7. Simulated transmittance profiles of four monitoring glasses used in virtual SPF625 77L depositions. Theoretical profile is shown for comparison. The green lines show the used monitoring wavelength for that glass.

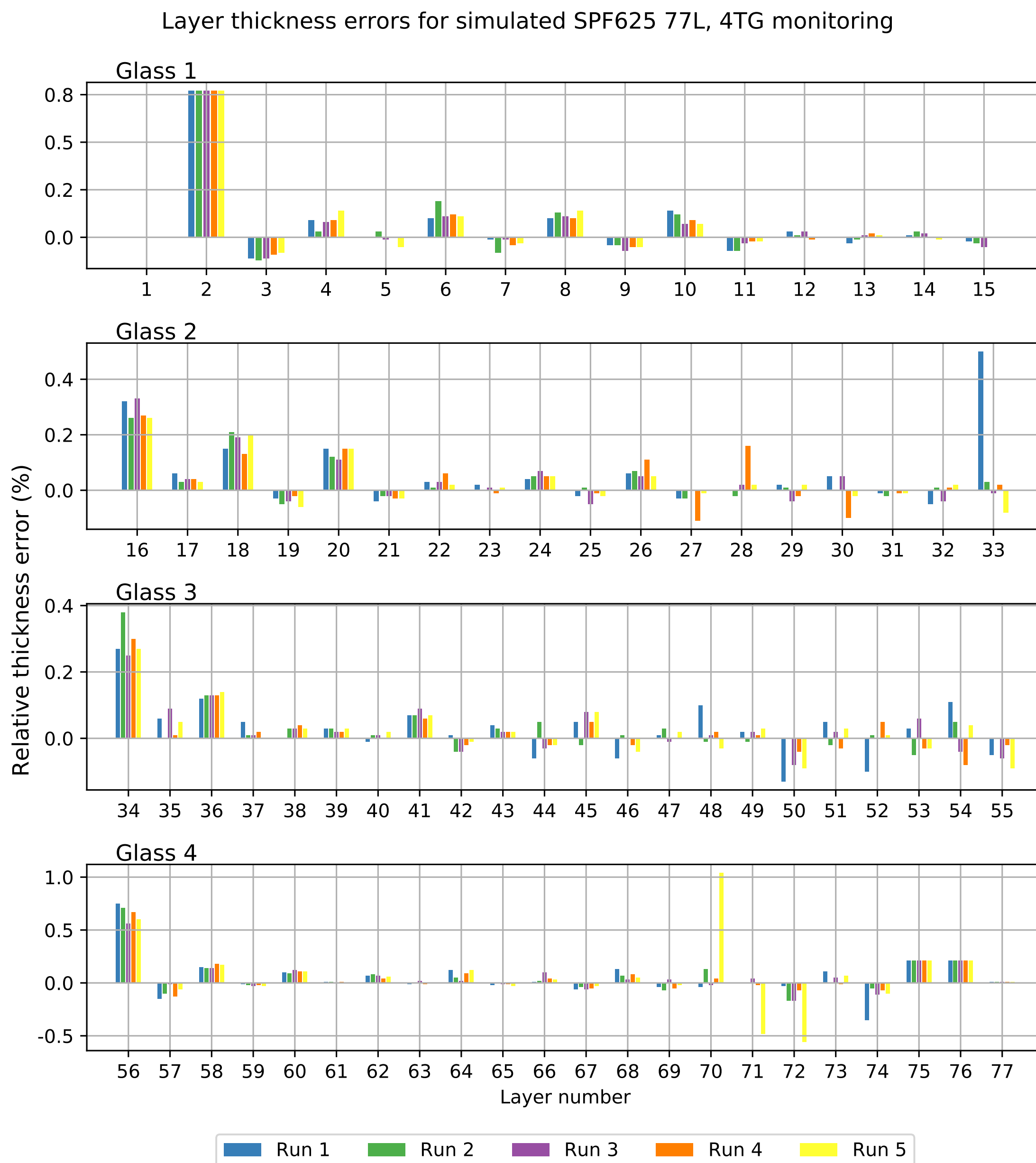

Figure A8. Relative layer thickness errors in the simulated SPF625 77L depositions when using four monitoring glasses.

Long pass edge filter

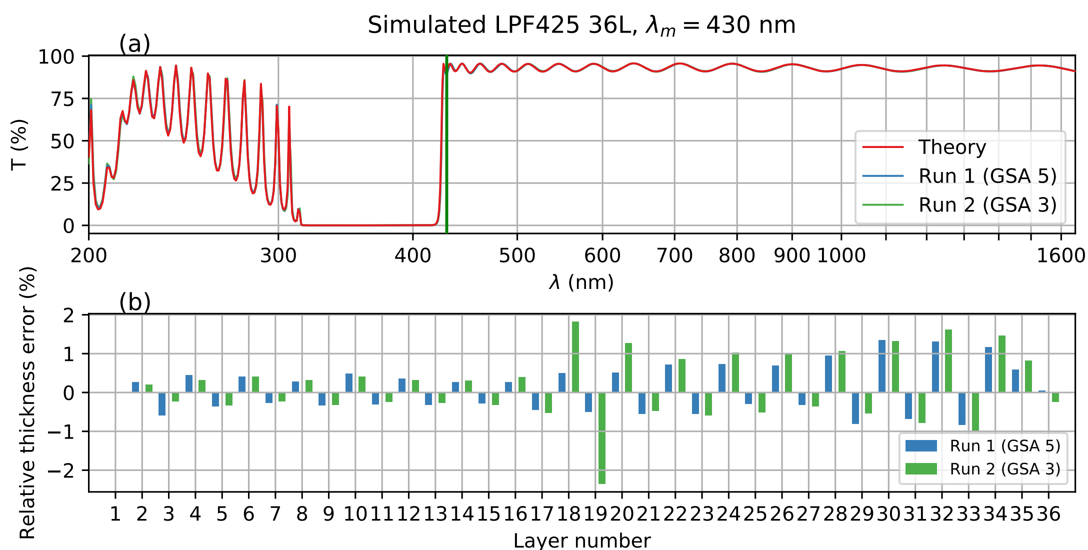

Figure A9. (a) Transmittance profiles of simulated LPF425 36L depositions, when $\lambda_m = 430$ nm (presented by the green line). Theoretical profile is also presented for comparison. **(b)** Relative layer thickness errors of the simulated filters.

Two values for Gain Signal Average were tried to see its influence on the results. The layer thickness errors implicate that GSA value 5 would be more optimal, but the transmittance profiles show that the actual effect is negligible.

Narrow bandpass filter

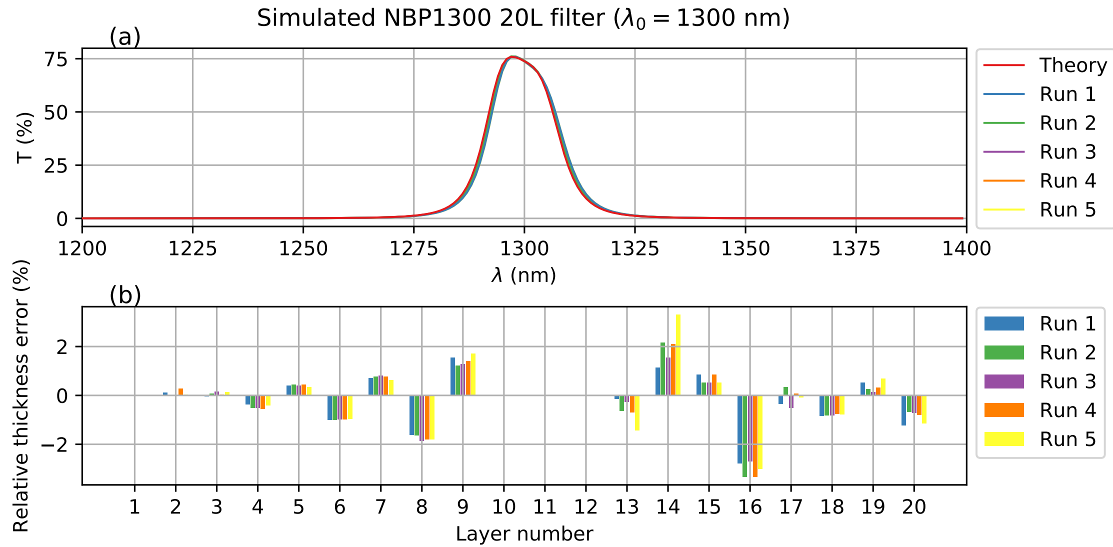

Figure A10. (a) Transmittance profiles for the theoretical NBP1300 filter as well as the simulated depositions and **(b)** relative layer thickness errors in the respective simulation runs. Results of five simulation runs are shown. Monitoring wavelength for the layers before Ag-layer was 1300 nm and and for the layers after Ag it was 1294 nm. QCM was used for the Ag layer and spacer layers, as well as the first layer. QCM was assumed to be perfectly accurate in the simulations.